

# **Characterization of Thin Film Photoanodes for Solar Water Splitting**

## **Proefschrift**

ter verkrijging van de graad van doctor  
aan de Technische Universiteit Delft;  
op gezag van de Rector Magnificus prof. ir. K.C.A.M. Luyben;  
voorzitter van het College voor Promoties,  
in het openbaar te verdedigen

op maandag 23 april 2012 om 10.00 uur  
door

**Cristina Simona ENACHE**

Licențiat în Fizică-Chimie  
Universitatea Transilvania Brașov

geboren te Brașov, Roemenië

Dit proefschrift is goedgekeurd door de promotor:

Prof. dr. J. Schoonman

Copromotor:

Dr. ir. R. van de Krol

Samenstelling promotiecommissie:

Rector Magnificus,	Voorzitter
Prof. dr. J. Schoonman,	Technische Universiteit Delft, promotor
Dr. ir. R. van de Krol,	Technische Universiteit Delft, copromotor
Prof. dr. G. Mul,	Universiteit Twente
Prof. dr. P.H.L. Notten,	Technische Universiteit Eindhoven
Prof. dr. A. Schmidt-Ott,	Technische Universiteit Delft
Prof. dr. A.H.M.E. Reinders,	Technische Universiteit Delft
Dr. ir. G. Boschloo,	Uppsala Universitet
Prof. dr. B. Dam,	Technische Universiteit Delft, reservelid

# *Contents*

<b>1. Introduction</b>	<b>1</b>
Abstract	
1.1 State of the Art	2
1.2 Hydrogen as an energy carrier	2
1.3 Semiconductors	6
1.3.1 General properties	6
1.3.2 The band diagram	6
1.3.3 Defects in semiconductors	7
1.4 Photoelectrolysis	10
1.4.1 Concept of photoelectrolysis	10
1.4.2 Requirements for semiconductor	11
1.5 Thin film photoanode materials	14
1.5.1 General introduction of titanium dioxide (TiO <sub>2</sub> )	14
1.5.2 General introduction of iron oxide (Fe <sub>2</sub> O <sub>3</sub> )	15
1.5.3 General introduction of indium vanadate (InVO <sub>4</sub> )	17
1.6 Deposition techniques	18
1.6.1 Spray Pyrolysis Deposition	18
1.6.1.1 Process parameters	19
1.6.1.2 Mechanism	19
1.6.2 Electrodeposition	19
1.7 Aims and outline of this thesis	20
References	21
<b>2. The photoresponse of Iron- and Carbon-doped TiO<sub>2</sub> (Anatase) photoelectrodes</b>	<b>23</b>
Abstract	
2.1 Introduction	24

2.2 Experimental details	24
2.2.1 Film preparation	24
2.2.2 Characterization techniques	24
2.3 Results and discussion	25
2.3.1 Morphology of the films	25
2.3.2 Structure characterization	26
2.3.3 Photoelectrochemical properties	27
2.3.54 Defect characterization	28
2.3.4.1 Mott-Schottky measurements	28
2.3.4.2 Photoluminescence characterization	32
2.4 Conclusions	34
References	35
<b>3. Addition of Carbon to Anatase TiO<sub>2</sub> by n-hexane treatment – surface or bulk doping?</b>	<b>37</b>
Abstract	
3.1 Introduction	38
3.2 Experimental details	39
3.2.1 Film preparation	39
3.2.2 Experimental set-up for the annealing treatment	39
3.2.3 Characterization techniques	40
3.3 Results and discussion	40
3.3.1 Film morphology	40
3.3.2 Structure characterization	42
3.3.3 Optical characterization	42
3.3.4 Photoelectrochemical properties	44
3.3.5 Phase transformation investigation	45
3.4 Conclusions	47
References	47
<b>4. Photoelectrochemical properties of thin-film InVO<sub>4</sub> photoanodes: the role of deep donor state</b>	<b>49</b>
Abstract	
4.1 Introduction	50
4.2 Experimental details	51
4.3 Results and discussion	52
4.3.1 Film morphology	52
4.3.2 Structure characterization	55
4.3.3 Optical and photoelectrochemical characterization	56
4.3.4 Impedance spectroscopy	60
4.3.5 Deep donor states	65
4.3.6 Photocurrent onset and flat bend potential	66
4.3.7 Defect chemistry considerations	67
4.4 Conclusions	69
References	70

---

<b>5. Characterization of structured <math>\alpha</math>-Fe<sub>2</sub>O<sub>3</sub> photoanodes prepared via electrodeposition and thermal oxidation of iron</b>	<b>73</b>
Abstract	
5.1 Introduction	74
5.2 Experimental details	75
5.2.1 Film preparation	75
5.2.2 Characterization techniques	75
5.3 Results and discussion	76
5.3.1 Electrolyte solution and sample preparation	76
5.3.2 Appearance and morphology	77
5.3.3 Structural characterization	80
5.3.4 Photoelectrochemical characterization	83
5.4 Summary and conclusions	88
5.5 Recommendations	89
References	90
<b>Summary</b>	<b>91</b>
<b>Samenvatting</b>	<b>95</b>
<b>Acknowledgments</b>	<b>101</b>
<b>Curriculum Vitae</b>	<b>103</b>
<b>List of publications</b>	<b>105</b>



# *Chapter 1*

**“I believe that water will one day be employed as fuel, that hydrogen and oxygen, which constitute it, used singly or together, will furnish an inexhaustible source of heat and light, of an intensity of which coal is not capable. I believe then that when the deposits of coal are exhausted, we shall heat and warm ourselves with water. Water will be the coal of the future.”**

**Jules Verne (1870) "L'île mystérieuse"**

## **Abstract**

*This chapter presents a general introduction of the photoelectrochemical production of hydrogen. An overview is given of the working principles, the necessary requirements for photoelectrodes, and the current state-of-the-art achievements in the field. It concludes with a brief outline of each chapter of this Ph.D. thesis.*

## 1.1 State of the art

Currently, mankind uses fossil fuels, such as coal, natural gas and oil for nearly all of its energy needs. These resources are, however not uniformly distributed over the world. Furthermore, their use contributes to the greenhouse effect due to their polluting combustion products, such as CO<sub>2</sub> [1]. Due to the rising standards of living and the fast growth of the world population, it is estimated that the global energy consumption will increase from 13.5 TW (in 2001) to 27-41 TW by 2050 [2]. Despite the fact that solar energy is the most abundant clean energy source available, the direct use of solar energy is limited and only 0.04% of all energy is generated by photovoltaic [3]. By covering 0.16% of the earth surface, which corresponds to the surface area of France and Germany combined, with 10% efficient solar cells, only 20 TW of power could be generated [2]. It is clear that finding, improving, and implementing various alternative sustainable energy sources, such as solar energy, wind energy, geothermal power, hydro-power, and biomass, is imperative to deal with the increased energy needs.

Hydrogen is widely regarded as a promising energy carrier for the future. It has a high gravimetric energy density and its only combustion product is pure water ( $\text{H}_2 + \text{O}_2 \rightarrow \text{H}_2\text{O} + 237 \text{ kJ/mol}$ ). Hydrogen can be produced by a number of processes, such as electrolysis (using electricity), steam reforming (converting natural gas into hydrogen), and biomass conversion (using micro-organisms to convert organic waste products into hydrogen) [4]. Nowadays, hydrogen is mainly produced from fossil fuels, a process which releases large amounts of CO<sub>2</sub> into the atmosphere. An alternative, more expensive method is the electrolysis of water. In this case, only hydrogen and oxygen are produced. Current commercially available electrolyzers operate with an electricity-to-hydrogen efficiency of ~85%. The main challenge here is to produce the required electricity from renewable sources, such as solar, wind, or hydropower.

## 1.2 Hydrogen as an energy carrier

Hydrogen is a promising energy carrier because of its high energy content and clean combustion. By burning hydrogen only water is produced, whereas the combustion of fossil fuels emits a large amount of CO<sub>2</sub> into the atmosphere, which contributes to the greenhouse effect. In addition, because hydrogen can be produced from a variety of resources that are widely distributed around the world, all societies can, in principle, have access to it and use it.

### *What is hydrogen?*

Hydrogen, the most abundant element in the universe, was first recognized as a distinctive element in 1766 by Henry Cavendish, an English chemist, who called it “inflammable air”. It had been observed that upon combustion of hydrogen in air, water was formed. This led to the name “hydrogen”, which means “water former”.

Hydrogen is a colorless, odorless gas with no taste, which burns with a pale blue flame that is virtually invisible in daylight. Its low density of 0.09 g/liter (at room temperature)

causes it to rapidly diffuse away when released in air. As a result, the explosion limits (18.3-59%) can only be reached in confined spaces.

#### *Compared to other fuels*

Hydrogen is a pollution-free energy carrier compared to other fuels, such as gasoline and natural gas. It is non-toxic and non-poisonous, in contrast to e.g. gasoline, oil and many other conventional fuels. Some of its characteristics are presented in Table 1.1.

**Table 1.1:** Properties and fire hazard of hydrogen compared to other fuels [5-7].

Property	Gasoline	Methane	Hydrogen
Density (kg/m <sup>3</sup> )	4.40	0.65	0.09
Boiling point (°C)	38-205	-161	-253
Flammability limits (in air)	1-7.6%	5.3-15%	4-75%
Explosion limits (in air)	1.1-3.3%	5.7-14%	18.3-59%
Ignition temperature (°C)	228-471	540	585
Flame temperature in air (°C)	2197	1875	2045
Specific heat at constant pressure (J/gK)	1.20	2.22	14.89

Hydrogen has to reach a concentration of 4% in the surrounding atmosphere before it poses a danger, whereas gasoline's concentration only has to reach 1% before the danger of ignition is apparent. It has to be mentioned though that since hydrogen is a gas, higher concentrations are reached faster in case of leakages since gasoline (a liquid) needs to evaporate first.

Hydrogen can be used in fuel cells to generate electricity. Fuel cells are electrochemical devices that convert hydrogen and oxygen into electricity. Unlike batteries, they do not need to recharge, and can be a continuous source of electric power as long as they are supplied with hydrogen and oxygen. Fuel cells are essentially the opposites of electrolyzers.

#### *How can hydrogen be produced?*

Hydrogen can be produced using various methods, as illustrated in Figure 1.1. Some of these processes, such as the use of nuclear energy or mechanical energy, are less likely to be used because the direct conversion of nuclear energy into electricity is more efficient. On the other hand, the nuclear production of hydrogen may still be viable because it is much easier to store large amounts of hydrogen than storing large amounts of electricity.

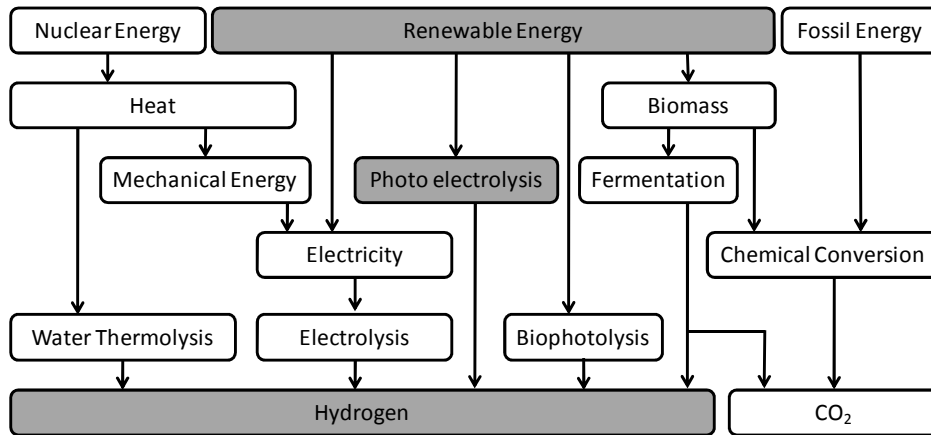


**Figure 1.1:** Different possible paths to produce hydrogen. Source: Adapted from John A. Turner, *Science* 285, 687, 1999.

Nowadays, hydrogen is mainly produced by methane steam reforming (converting natural gas into hydrogen and CO, followed by the water gas shift reaction), or by partial oxidation of heavy oils [8]. In both cases carbon dioxide is also produced. An alternative route to generate hydrogen is via electrolysis of water. The main advantage is the high purity of the hydrogen with no traces of CO that can degrade (or “poison”) the fuel cell. In order to make the production sustainable, the electricity should come from renewable sources, such as solar energy via solar cells. At this moment only a small fraction is produced from renewable sources because of the low efficiencies and the implicitly high prices of processes that are still in the development stage. The practical overall efficiency of an electrolyzer coupled to a solar cell (having an efficiency of 12%) has a value of 8%. In this respect the direct photoelectrolysis with a semiconductor electrode may be more promising, i.e., the so-called photoelectrochemical cell. In Table 1.2 a summary of performance, stage of development, costs, and CO<sub>2</sub> emissions for different processes to produce hydrogen is given.

The research described in this thesis investigates the possibility to produce hydrogen by direct photoelectrolysis of water using solar energy. The aim is to find suitable semiconducting photoanodes that can convert light into electron-hole pairs, which are then used to split water into hydrogen and oxygen. First, a brief review of the properties of semiconductors, the working principles of photoelectrochemical devices, and the current achievements in this field will be given. After this, the materials studied in this thesis will be discussed in more detail.

**Table 1.2:** Costs and performance characteristics of various hydrogen production processes [7]. The given costs are reported in relation with the costs of steam methane reforming (SMR).

Hydrogen production process	Energy Required [kWh/Nm <sup>3</sup> of H <sub>2</sub> ]		Status of technology	Efficiency [%]	Costs Relative to SMR	% of total production	Need for CO <sub>2</sub> sequestra tion
	Ideal	Practical					
Methane steam reforming	0.78	2-2.5	Mature	70-80	1	48	Y
Methane/NG pyrolysis			R&D to mature	72-54	0.9		N
H <sub>2</sub> S methane reforming	1.5	-	R&D	50	<1	-	N
Landfill gas dry reformation			R&D	47-48	~1	-	Y
Partial oxidation of heavy oil	0.94	4.9	Mature	70	1.8	30	Y
Naphta reforming			Mature				
Steam reforming of waste oils			R&D	75	<1	-	Y
Coal gasification –TEXACO	1.01	8.6	Mature	60	1.4-2.6		Y
Partial oxidation of coal			Mature	55		18	Y
Steam iron-process			R&D	46	1.9		Y
Chloralkali electrolysis			Mature		by-	4	N
					product		
Grid electrolysis of water	3.54	4.9	R&D	27	3-10		Y
Solar & PV-electrolysis of water			R&D to mature	10	>3		N
High-temperature electrolysis of water			R&D	48	2.2		N
Thermochemical water splitting cycles			Early R&D	35-45	6		N
Biomass gasification			R&D	45-50	2.0-2.4		
Photobiological			Early R&D	<1		-	N
Photolysis of water			Early R&D	<10			N
Photoelectrochemical decomposition of water			Early R&D				N
Photocatalytic decomposition of water			Early R&D				N

## 1.3 Semiconductors

### 1.3.1 General properties

Nowadays, semiconductors play an important role in modern society (e.g. integrated circuits, solar cells). Research on the photoelectric effect in semiconductors first started in 1839, when Becquerel observed an electric current between two silver electrodes immersed in an electrolyte solution under illumination [9]. The following sections will give an overview of the basic properties of semiconductors, and how they can be used in a photoelectrochemical device to split water.

### 1.3.2 The band diagram

Semiconductors are characterized by a bandgap (in the order of 1-3.5 eV) between the valence and the conduction band, which can be crossed by electrons through thermal or optical excitation. The valence band (VB) is the highest energy band filled with electrons, while the conduction band (CB) is the lowest unoccupied band. In all materials, electrical conductivity requires the presence of mobile charge carriers. These charge carriers can be either electrons in the (normally empty) conduction band and/or holes in the (normally filled) valence band. These can be created by either thermal or optical excitation. Only partially filled bands contribute to electrical conductivity. In an insulator the bandgap is too large for electrons to be excited by practical means, while in a metal the conduction and valence bands overlap (Figure 1.2). The Fermi level, which can be viewed as the solid-state physics equivalent of the electrochemical potential of the electrons, lies halfway between the CB and VB within the bandgap of the semiconductor.

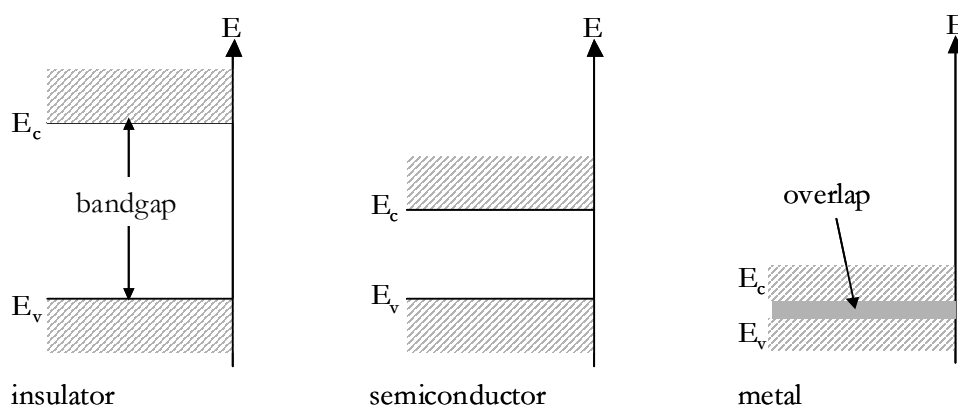


**Figure 1.2:** Band diagrams for insulator, semiconductor, and metal.

When the n-type semiconductor and the electrolyte solution are brought into contact, charges will be transferred between the semiconductor surface and the electrolyte until the electrochemical potentials have equilibrated. (Figure 1.3 a,b). For an n-type semiconductor electrode the Fermi level,  $E_F$ , is typically higher than the redox potential of the dominant redox species in the electrolyte. Therefore, electrons are transferred from the semiconductor to the electrolyte species, and an upward bending of the bands occurs, as is shown in

Figure 1.3 b. The band bending can be controlled externally by applying a potential between the semiconductor photoanode and the reference electrode. The applied potential for which no excess charge exists in the semiconductor is referred to as the ‘flatband potential’ ( $V_{fb}$ ).

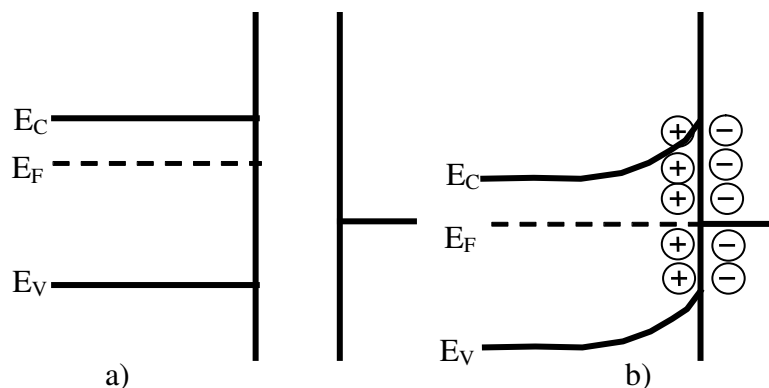


**Figure 1.3:** Schematic representation of the band bending that occurs when an n-type semiconductor is brought into contact with an electrolyte: a) n-type semiconductor before contact in dark; b) after contact with the electrolyte band bending occurs and a depletion layer is formed in the dark.

The (local) concentration of electrons can be calculated from the energy difference between the Fermi level and the conduction band minimum using the following expression:

$$n = N_C \exp\left(\frac{-E_C - E_F}{kT}\right) \quad (1)$$

Here,  $k$  is Boltzmann’s constant,  $T$  is the temperature in Kelvin,  $E_C$  is the conduction band minimum,  $N_C$  is the effective density of states in the conduction band, and  $E_F$  is the Fermi level.

More detailed information on semiconductor properties and the effect of the band bending in solution can be found in books dedicated to these subjects. Especially recommended are the books of Bard and Faulkner, and of Morrison [10,11].

### 1.3.3 Defects in semiconductors

While the electronic structure of a pure, perfect crystal determines the basic optical and electrical properties of a material, many of these properties are also strongly affected by the presence of defects. The two most common types of point defects in ionic materials are Frenkel and Schottky defects. These are so-called “intrinsic defects” since they can be thermally generated in a perfect crystal. A Frenkel defect is formed when a cation is displaced from its regular lattice site into an interstitial site, leaving a vacancy behind. If an anion occupies an interstitial site and leaves an anion vacancy behind, it is called anti-Frenkel disorder. A Schottky defect pair is formed by the simultaneous creation of both cation and anion vacancies, as illustrated in Figure 1.4.

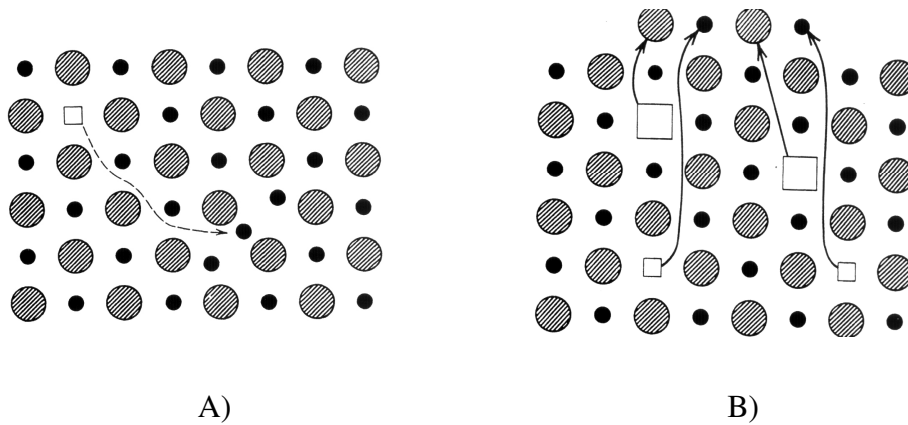
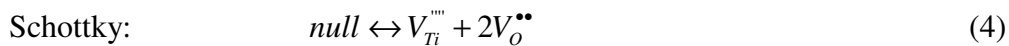
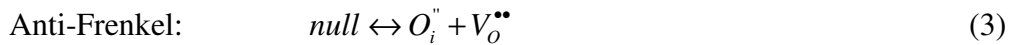
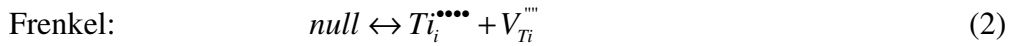


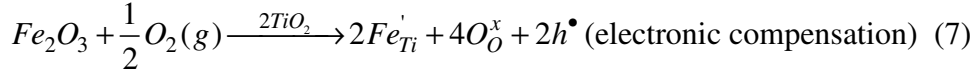
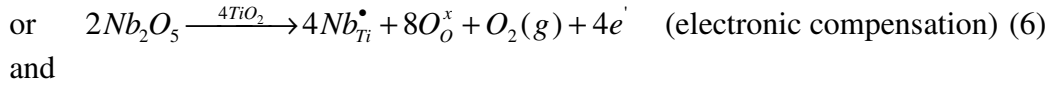
Figure 1.4: Frenkel (A) and Schottky (B) defects [12].

The vacancies must be formed in a stoichiometric ratio in order to preserve electrical neutrality in the crystal [12]. In the case of  $\text{TiO}_2$  the formation of Frenkel and Schottky defects can be written as follows:



Here, the standard Kröger-Vink notation is used to describe the various defects [12].

The electronic properties of a semiconductor, such as  $\text{TiO}_2$ , can be controlled by the deliberate introduction of foreign atoms in the regular crystal lattice. This process, called ‘doping’, is often used to improve the conductivity of a semiconductor. The foreign ions can be incorporated substitutionally (on lattice sites normally occupied by regular cations or anions), or interstitially (on normally empty lattice sites in the crystal structure). Each type of defect in the regular crystal structure can have an effective charge that has to be either ionically or electronically compensated. For example, Nb has five valence electrons. When Nb sits on a Ti (four electrons) site, four valence electrons are used to form bonds with the surrounding oxygen ions, and one electron remains ( $\text{Nb}_{\text{Ti}}^{\bullet}$ ), so the total charge is zero. Nb gives this electron to the lattice (i.e., the conduction band) and is, therefore, called a “donor”. Aluminum (Al) has only three electrons to share with the neighboring O-atoms, so it needs an extra electron and it is called an “acceptor”. The negatively charged aluminum ( $\text{Al}_{\text{Ti}}^{\prime}$ ) is charge-compensated by an electron-hole, indicated as  $h^{\bullet}$ . If a semiconductor has more donors than acceptors, then the majority of the electronic charge carriers are electrons, and the material is called “n-type”. If there are more acceptors, then the majority charge carriers are holes and the material is called “p-type”. Based on Kröger-Vink notation the incorporation of  $\text{Nb}_2\text{O}_5$  or  $\text{Fe}_2\text{O}_3$  as a dopant in  $\text{TiO}_2$  is given by:



In  $TiO_2$ , pentavalent dopants such as  $Nb_{Ti}^{\bullet}$  or  $Ta_{Ti}^{\bullet}$ , as well as positively charged intrinsic defects such as  $V_O^{\bullet\bullet}$  and  $Ti_i^{\prime\prime\prime\prime}$  are donors, while trivalent solutes such as  $Al_{Ti}'$  and  $Fe_{Ti}'$ , or negatively charged intrinsic defects such as  $V_{Ti}^{\prime\prime}$  and  $O_i''$  are acceptors [13]. In a donor-doped material, electrons can be trapped on the positively charged defects, such as  $Nb_{Ti}^{\bullet}$ . Then these electrons are no longer free, and are trapped in an energy level below the conduction band, as is schematically drawn in Figure 1.5. If the donor level is located within  $\sim 3kT$  ( $\sim 75$  meV at room temperature) of the conduction band, it is called a shallow donor and it will be (almost) fully ionized at room temperature. In the case of deep donors, with levels  $>100$  meV below the conduction band, much higher temperatures are required for ionisation. The case of acceptor-doped semiconductors is analogous, here the acceptor energy levels are located just above the valence band. Shallow donors and acceptors can be used to increase the conductivity in n-type and p-type semiconductors, respectively, at room temperature.

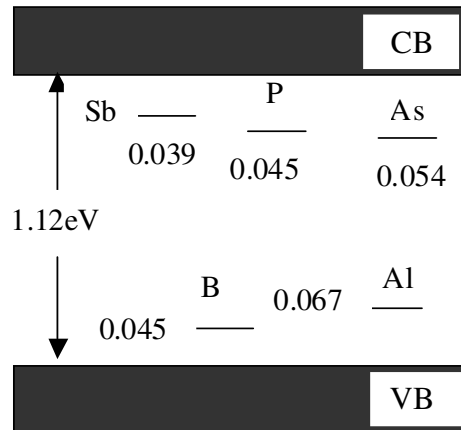
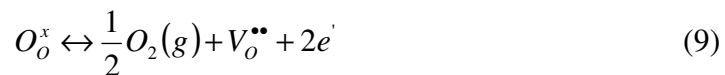


**Figure 1.5:** Donor and acceptor levels for selected dopants in silicon. The donor dopants are Sb, P, and As and the acceptor type defects are B and Al in this diagram [12].

Impurity addition, however, is not the only doping mechanism. The stoichiometry of an oxide semiconductor can also be changed by reduction [14]. The reduction of an oxide, for example  $TiO_2$ , can be written as the removal of oxygen (i.e., an oxide-ion) to the gas phase, leaving behind oxygen vacancies ( $V_O^{\bullet\bullet}$ ):



In this case oxygen vacancies (formally “oxide-ion vacancies”) function as donors because they yield more electrons in the system (n-type). Reduction can occur by heating the material in an oxygen-poor reducing environment, for example, vacuum, hydrogen, argon, or CO.

## 1.4 Photoelectrolysis

### 1.4.1 Concept of photoelectrolysis

Photoelectrolysis is a very elegant method towards the truly sustainable production of hydrogen. The working principle will be illustrated by using the energy diagram shown in Figure 1.6. The hydrogen production system consists of a semiconductor working electrode and a platinum counter electrode, both immersed in an aqueous electrolyte.

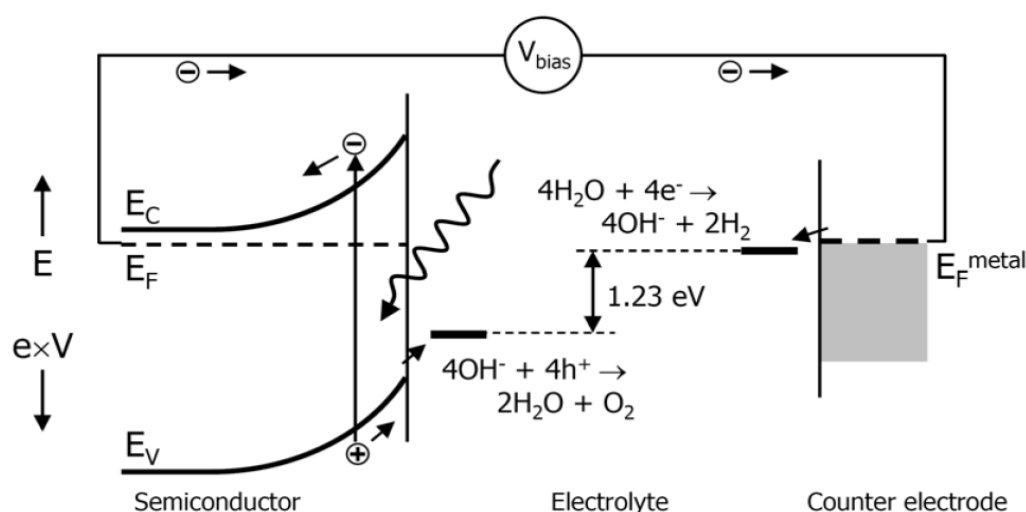
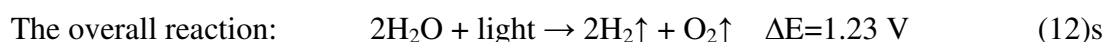
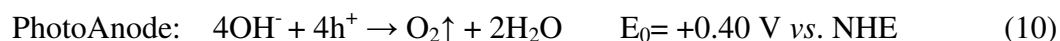


**Figure 1.6:** Schematic working principle of a photoelectrochemical cell based on an n-type semiconductor.

Upon illumination with sufficient energy electrons in the valence band (VB) are excited into the conduction band (CB), creating an electron-hole pair in the semiconductor. The electric field present in the semiconductor, usually induced by electrons trapped at OH species adsorbed at the surface, separates the photo-generated charge carriers. The electrons are transported from the conduction band via an external wire to the platinum cathode where the hydrogen evolution reaction occurs. The holes are transported to the photoanode surface where they oxidize water to produce oxygen. In this way, hydrogen and oxygen are produced at the different electrodes and can be conveniently collected in separate storage volumes. In an alkaline medium the electrochemical reactions that occur at the cathode and photoanode are:



Here, the potentials are given for the *reduction* half-reaction under standard conditions (298K, 1 bar, all concentrations 1 mol/L).

### 1.4.2 Requirements for semiconductor

In order to successfully split water with solar irradiation, suitable semiconductor electrodes are needed. Following the discovery of the photocatalytic splitting of water on rutile TiO<sub>2</sub> electrodes by Honda and Fujishima in 1972, a lot of effort was devoted to the development of low-cost transition metal oxides [15]. They have to fulfill several requirements such as:

- The bandgap has to be larger than 1.23 eV. In practice, ~1.9 eV is required to split water, since an additional 0.4 eV is needed to cover thermodynamic losses and ~0.3-0.4 eV for overpotentials [16,17]. At the same time, the band gap should be small enough to absorb an appreciable part of the solar spectrum
- The conduction band edge has to be higher in energy than the water reduction potential so that the reduction of water will be energetically possible
- The valence band edge has to be lower in energy than the water oxidation potential so that the oxidation of water will be energetically possible
- A good stability in aqueous environments and resistant to photocorrosion
- Efficient charge separation and transport. Fast charge transfer is desired to avoid recombination.
- Non-toxic, environmentally friendly
- Low cost

In Figure 1.7 some semiconductor materials used in solar-cell applications are presented. As can be seen, few semiconducting materials fulfill the energetic requirements for water splitting. Most non-oxide semiconductors, such as CdS, GaP, GaAs, etc, either dissolve or form a thin oxide film, which prevents electron transfer across the interface. ZnO decomposes in aqueous solution upon illumination. Titanium dioxide (TiO<sub>2</sub>) and tin dioxide (SnO<sub>2</sub>) fulfill almost all requirements. Unfortunately, TiO<sub>2</sub> absorbs only in the ultraviolet part of the solar spectrum due to its large bandgap of 3.2 eV. Hence, it only absorbs ~4% of the incident sunlight and the overall conversion efficiency is low. Detailed studies on this oxide are presented in Chapters 2 and 3 of this thesis. For most of the materials the band edges are not suitably positioned with regard to the water oxidation and/or reduction potentials. For example, if the conduction band of the material is positioned at a more positive potential than the hydrogen evolution potential, an externally applied bias is necessary. Fe<sub>2</sub>O<sub>3</sub> is such an oxide. More details on iron oxide are presented in Chapter 5. A general trend is that wide-bandgap materials, such as most oxide semiconductors, are stable under illumination, while small bandgap semiconductors (that can absorb more visible light) are not.

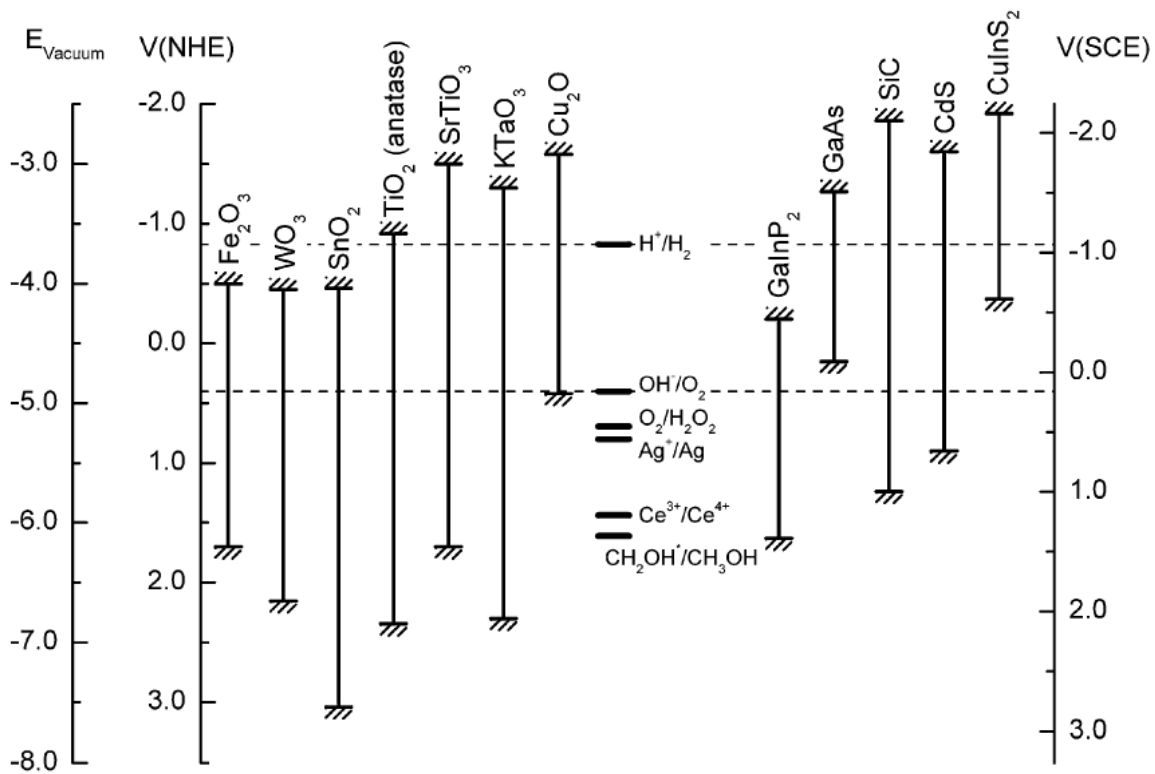


**Figure 1.7:** Band positions and values of the bandgap of several semiconductors in contact with an aqueous electrolyte at pH 14. The energy scale is indicated having the vacuum level or NHE (normal hydrogen electrode) as a reference [18-21]. It should be noted that the reduction and oxidation potentials of water as well as the band edges of most materials (in particular the metal oxides) vary with -59 mV per pH unit.

The idea of splitting water by using a semiconductor photoelectrode was reported for the first time in 1972 by Fujishima and Honda [22]. They showed that water could be split into hydrogen and oxygen by irradiating rutile TiO<sub>2</sub> with ultraviolet light. Following this discovery a lot of effort was devoted to find efficient semiconductor photoelectrodes. Different approaches have been investigated in this area:

#### A) *Electrolyser coupled to a photovoltaic (PV) cell.*

This type of technology uses solar cells to provide the necessary voltage to split water. The main advantage over the hydrogen produced via the steam reforming of methane is the high purity hydrogen obtained with no traces of CO which will poison the platinum catalyst of the Polymer-Electrolyte Membrane Fuel Cell (PEMFC). Using a solar cell with 12 % efficiency in combination with a 85% efficient electrolyser, the overall conversion efficiency is limited to 8% [23,24]. The advantage of this approach is that both electrolyser and photovoltaic cell can be developed separately and the demands for the one device do not restrict the other. However, the main disadvantage is that two separated devices are less convenient in terms of

energy losses, packaging and overall costs. Extensive work is going on to improve further the efficiency of the solar cells and lower the costs.

## **B) Direct photoelectrolysis**

### *i) Micro-heterogeneous systems of photocatalyst particles.*

In this case the semiconductor is suspended in an aqueous solution in the form of a fine powder. With this approach both the reduction and oxidation of water take place at the surface of the same particle. Using this method eliminates the need for a conductive substrate so that conventional high-temperature solid-state synthesis processes can be used to prepare various compounds in a relatively simple manner. Co-catalysts, necessary to enhance the kinetics and avoid recombination can be easily included in the desired amount by mixing and firing. Moreover, this approach provides a convenient screening method for selecting/preparing suitable photoanode materials. Various powder systems, such as  $\text{BiVO}_4$  [15],  $\text{WO}_3$  [25,26],  $\text{InVO}_4$  [27],  $\text{BaCrO}_4$  [28],  $\text{Bi}_2\text{YNbO}_7$  [29], and various barium tantalates [30], have been reported to generate hydrogen and/or oxygen, albeit with low efficiencies [21]. One of the disadvantages of using powder photocatalysts is the difficulty to accurately determine the efficiency of such a system. More importantly, hydrogen and oxygen are produced in the same reactor volume and need to be separated. Furthermore, the catalysts need to be regenerated once in a while, which requires separation of the catalyst particles from water.

### *ii) Photoelectrochemical cells (PEC)*

Compared to coupled PV / electrolysis, a more attractive approach is to directly use the photo-generated charge carriers for the reduction and oxidation of water, i.e., without sending them through an external circuit to a separate electrode. This can be achieved by using a semiconducting photoanode and/or photocathode that are in direct contact with water. By using two separate electrodes, the  $\text{H}_2/\text{O}_2$  and catalyst/water separation problems discussed in the previous paragraph can be easily avoided. It is expected that such an integrated device will lead to less energy losses. Moreover, it is more attractive in terms of packaging and overall system costs. The challenge is to find suitable semiconductor electrodes that absorb sufficient visible light, have suitable band edge positions for water splitting and are stable against (photo-)corrosion. Despite extensive efforts starting in the 1970s, no photoanode materials have been found to fulfill all requirements. Extensive work has been done on  $\text{TiO}_2$ ,  $\text{Fe}_2\text{O}_3$ ,  $\text{WO}_3$  as photoanode materials. Augustynski et al. reported an efficiency of 4.5 % for  $\text{WO}_3$  photoelectrodes using a dye-sensitized solar cell (DSSC) to provide the necessary bias voltage, the so-called tandem cells [31,32]. This value is close to the theoretical efficiency reported for this material [16]. Recent work on  $\text{Fe}_2\text{O}_3$  (hematite) photoelectrodes indicates overall solar-to-hydrogen efficiencies of 2.1 % [33]. The estimated theoretical efficiency for this material is 12.9 % [16], which indicates ample opportunities for improvements.  $\text{Fe}_2\text{O}_3$  is one of the most promising candidates for efficient photocleavage of water using a PEC due to its bandgap of 2.2 eV, which is close to the supposedly ideal value of 2.03 eV [16].

Since metal oxide semiconductors absorb only a small portion of the solar spectrum, several efforts have been made to design monolithic tandem cells with several functional layers combined into a single plate device. Impressive efficiencies in the range of 12-20 % have been achieved for monolithic tandem cells based on III/IV semiconductors, i.e., GaAs,  $\text{Al}_x\text{Ga}_{1-x}\text{As}$ , and  $\text{GaInP}_2$  [23,34-36]. When the plate is inserted in a solution and illuminated hydrogen and oxygen evolve at opposite sides. The main problem is the photocorrosion of these materials and the fact that devices based on high-purity semiconducting materials are still too expensive for terrestrial applications. More affordable semiconductors produced using simple deposition methods which are easy to scale up are required in this sense. However, the main disadvantage of low-cost deposition techniques is the lower final purity of the materials and, as a consequence, more recombination.

An efficient, economical, and sustainable method to produce hydrogen still needs to be developed. It is still a great technological challenge to change from an oil-based economy towards a sustainable energy economy.

## **1.5 Thin film photoanode materials**

In the study described in this thesis the primary focus is on transition metal oxide semiconductors, in particular titanium dioxide ( $\text{TiO}_2$ ), indium vanadate ( $\text{InVO}_4$ ), and iron oxide ( $\text{Fe}_2\text{O}_3$ ) as thin film photoelectrodes for the splitting of water in oxygen and hydrogen.

### **1.5.1 General introduction of $\text{TiO}_2$**

Titanium dioxide  $\text{TiO}_2$  is a transition metal oxide that occurs in three different natural forms (rutile, anatase, and brookite), as well as in five polymorphs that can be synthetically prepared. The anatase form is usually obtained at temperatures below  $500^\circ\text{C}$ , while rutile is thermodynamically stable at all temperatures and can be prepared between  $700$ - $1000^\circ\text{C}$ .

$\text{TiO}_2$  is a well known white pigment and is not only widely used in paints but also in toothpaste, chewing gum, or as a UV-VIS absorber in sun cream and various cosmetic products.

In addition, anatase  $\text{TiO}_2$  has been investigated as a functional ceramic for a wide variety of applications, such as solar cells, anode materials in batteries, ceramics, photocatalysis, protective coatings, anti-reflection coatings, and optoelectronics. It is one of the few materials that have suitable band edge positions for water splitting applications, without the need for an external bias. Some basic characteristic properties of anatase and rutile  $\text{TiO}_2$  are presented in Table 1.3. The bandgap of anatase is slightly larger than that of rutile, but anatase is nevertheless often preferred due to its higher electron mobility, higher photocatalytic activity, more open structure (possibility to incorporate dopants), and lower temperature of deposition.

**Table 1.3:** Properties of TiO<sub>2</sub>.

Properties	Anatase	Rutile
Bandgap (eV) [37,38]	3.26	3.05
Density (g/cm <sup>3</sup> ) [39]	3.84	4.26
Dielectric constant [40]	55	170
Hardness (Mohs) [39]	5.5	6.5
Melting point (°C) [39]	Converts to rutile	1830
Refractive index [41]	2.49-2.55	2.61-2.90

### 1.5.2 General introduction of Fe<sub>2</sub>O<sub>3</sub>

Iron oxide is another transition metal oxide that can be found in a variety of forms: FeO (wüstite),  $\alpha$ -Fe<sub>2</sub>O<sub>3</sub> (hematite),  $\beta$ -Fe<sub>2</sub>O<sub>3</sub>,  $\gamma$ -Fe<sub>2</sub>O<sub>3</sub> (maghemite), and Fe<sub>3</sub>O<sub>4</sub> (magnetite). Fe<sub>2</sub>O<sub>3</sub> is used in the pigment industry for a large variety of red brown colors and in cosmetics due to its non-toxicity and moisture resistance. Hematite Fe<sub>2</sub>O<sub>3</sub> is also known as “rust” and is a widely available oxide, inexpensive and with good chemical stability. It is able to absorb photons from the green-blue part of the spectrum, between 300-600 nm, which represents ~32% of the photons of the solar spectrum. Its small band gap of 2.1 eV makes it one of the most promising candidates for photoelectrochemical devices.

However, there are some challenges with regard to other properties of hematite Fe<sub>2</sub>O<sub>3</sub>. It has a short hole diffusion length (2-4 nm [42] or 20 nm [43]), a low absorption coefficient and slow surface reaction kinetics. Moreover, the conduction band of Fe<sub>2</sub>O<sub>3</sub> is positioned at too positive potentials to be able to reduce water directly, and an external bias is necessary. To overcome these limitations, a morphology based on nanowires has been proposed for hematite-based photoelectrodes. By controlling the radius of the nanowires, which should be less than the hole diffusion length of the Fe<sub>2</sub>O<sub>3</sub>, hole transport limitations can be avoided.

A recent theoretical study suggested that the ideal material for water splitting should have a bandgap of about 2 eV, which is close to that of  $\alpha$ -Fe<sub>2</sub>O<sub>3</sub> [16]. In Table 1.4 a summary of theoretical solar-to-hydrogen efficiencies for different materials are presented. With an estimated theoretical efficiency of 12.9%, Fe<sub>2</sub>O<sub>3</sub> is indeed one of the most promising candidates. Some other general characteristic properties of Fe<sub>2</sub>O<sub>3</sub> are presented in Table 1.5. The requirements needed for an ideal material/semiconductor to function as a photoelectrode for water splitting are presented in paragraph 1.4.2.

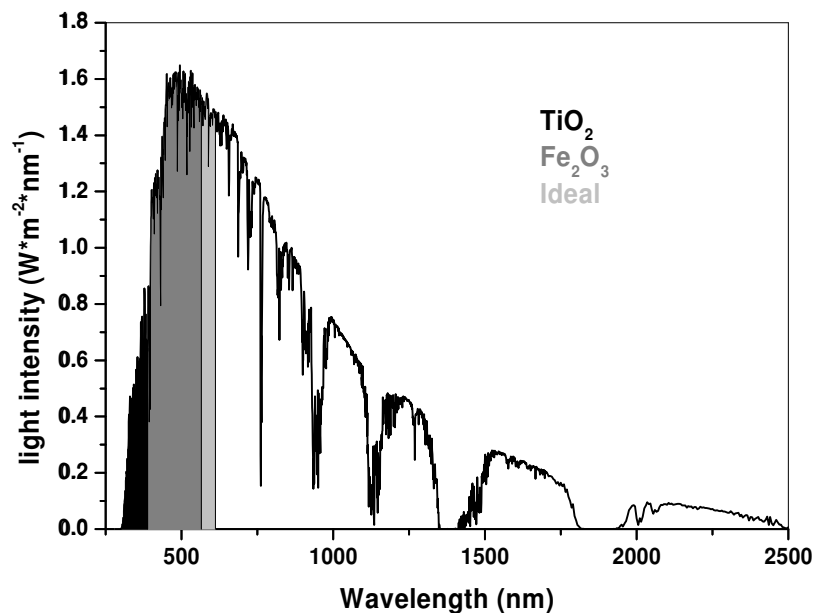
Figure 1.8 shows how the bandgaps of TiO<sub>2</sub>, Fe<sub>2</sub>O<sub>3</sub> and an ideal material match with the solar spectrum. Clearly, only a part of the solar spectrum can be used to split water directly.

**Table 1.4:** Overview of different photoanode materials with their bandgaps and estimated theoretical efficiencies for water splitting [16].

Material	Bandgap (eV)	Cut-off Wavelength (nm)	Max Theoretical Efficiency (%)
Anatase TiO <sub>2</sub>	3.26	387	1.3
Rutile TiO <sub>2</sub>	3.05	413	2.2
WO <sub>3</sub>	2.7	459	4.8
$\alpha$ -Fe <sub>2</sub> O <sub>3</sub>	2.1	564	12.9
Ideal material	2.03	610	16.8

**Table 1.5:** Properties of Fe<sub>2</sub>O<sub>3</sub> (hematite)

Properties	$\alpha$ -Fe <sub>2</sub> O <sub>3</sub>
Bandgap (eV) [44-46]	2.0-2.2
Density (g/cm <sup>3</sup> ) [39]	5.25
Dielectric constant [47]	100
Melting point (°C) [39]	1565
Refractive index [39]	2.94

**Figure 1.8:** Intensity of sunlight versus wavelength for AM1.5 conditions. Also indicated are the regions in which TiO<sub>2</sub>, Fe<sub>2</sub>O<sub>3</sub>, and the hypothetically ideal material absorb light [16].

### 1.5.3 General introduction of $\text{InVO}_4$

Most research on photoanodes for water splitting has been focused on  $\text{TiO}_2$ , which was mainly due to its excellent photochemical stability and high activity under UV illumination. Ye et al. proposed  $\text{InVO}_4$  as a promising alternative material for water splitting applications due to its relatively small bandgap, which they reported to be about 2 eV [48]. As can be seen in Figure 1.9 the absorption of  $\text{InVO}_4$  is higher than that of  $\text{TiO}_2$  and is also present in the visible part of the spectrum. Moreover, Ye et al. reported that the band edges of this material are suitable for water splitting (see Figure 1.10). However, their study was performed exclusively on powders, which makes the understanding and optimization of this material more difficult. In this thesis, thin films of  $\text{InVO}_4$  are studied, which allows detailed investigation of the optical and electronic properties of this material. The results are reported in Chapter 4.

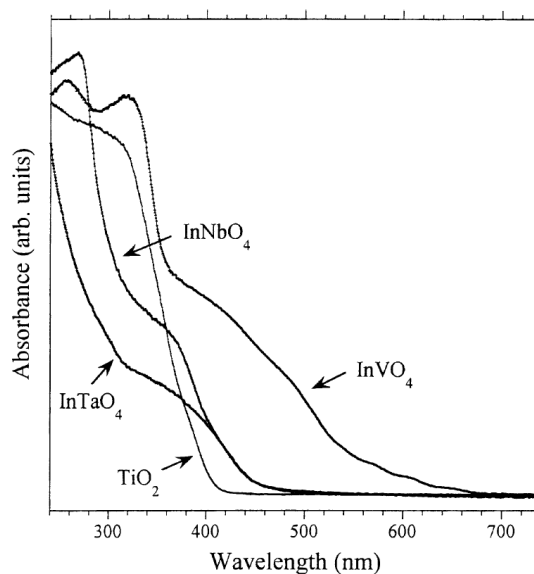


**Figure 1.9:** Diffuse reflectance spectra of  $\text{InVO}_4$  compared to  $\text{TiO}_2$  (P25),  $\text{InTaO}_4$ , and  $\text{InNbO}_4$  [27,48].

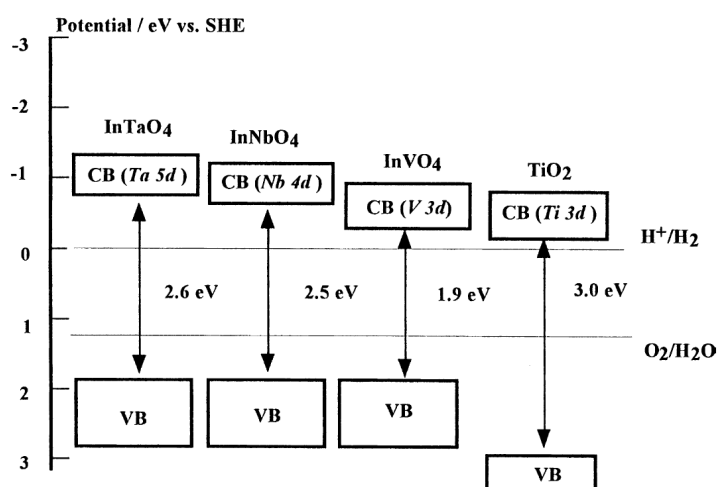


**Figure 1.10:** Suggested locations of conduction and valence bands of  $\text{InTaO}_4$ ,  $\text{InNbO}_4$ ,  $\text{InVO}_4$ , and  $\text{TiO}_2$  [27].

## 1.6 Deposition techniques

There are many techniques that can be used to deposit thin films of metal oxides. Depending on the nature of the deposition process that is involved they can be classified as physical or chemical methods. Examples of physical deposition techniques are sputtering, laser ablation, physical vapor deposition (PVD), and molecular beam epitaxy (MBE). The chemical methods include both gas- and liquid-phase techniques, such as chemical vapor deposition (CVD), atomic layer deposition (ALD), spray pyrolysis (SP), and dip coating and spin coating of particle-containing solutions made with sol-gel techniques. In this thesis the attention will be focused on spray pyrolysis and electrodeposition (ED) as techniques for deposition.

### 1.6.1 Spray Pyrolysis Deposition

During spray pyrolysis, aerosol droplets of the precursor solution are formed using an atomization nozzle and transported to the heated substrate using a carrier gas. At the heated substrate, the solvent evaporates and the metal ions react with oxygen from the atmosphere, forming the thin metal oxide film.

Different types of methods have been developed for spray pyrolysis, mainly differing in the way in which the aerosol is formed. For instance, the aerosol can be formed by electrostatic forces (Electrostatic Spray Deposition, ESD), by ultrasonic agitation (Ultrasonic Spray Pyrolysis, USP), or by pressurized gas [49]. The latter method is also known as pneumatic spray pyrolysis, and is used in this thesis to produce various oxides ( $\text{TiO}_2$  in Chapter 2 and 3,  $\text{InVO}_4$  in Chapter 4). A schematic diagram of the used spray set-up is presented in Figure 1.11.

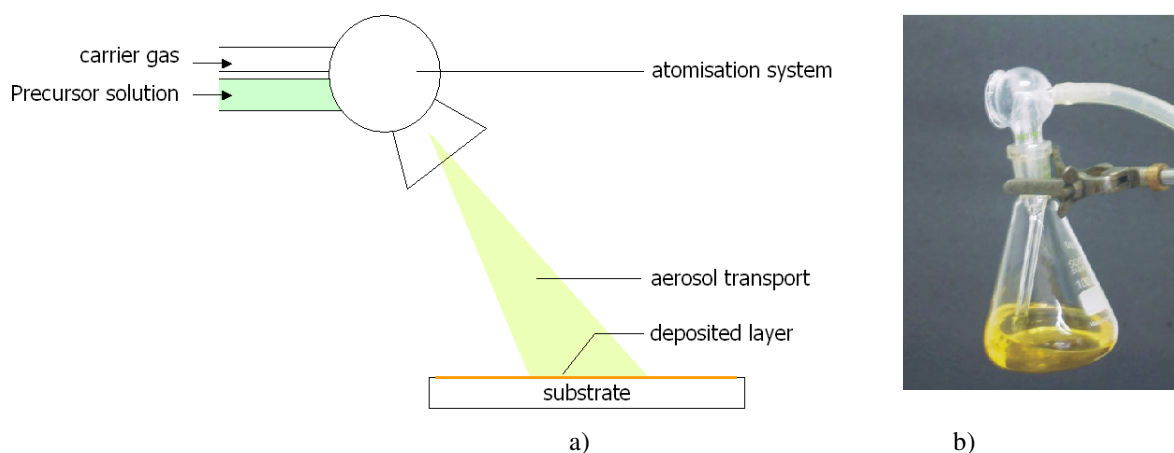


**Figure 1.11:** a) Schematic drawing of the experimental set-up used for spray pyrolysis; b) spray nozzle (pneumatic atomizer) used in the spray pyrolysis process. (Courtesy to David Lloyd).

### **1.6.1.1 Process parameters**

The spray pyrolysis conditions need to be carefully controlled to yield layers with the desired properties. Systematic variation of various process parameters, such as substrate temperature, gas flow rate, substrate-nozzle distance, precursor solution concentration, and time between spray cycles (for intermittent spraying), is often necessary before good quality films can be obtained. To complicate matters further, certain parameters may depend on each other. In general, the surface temperature is a critical parameter regarding the influence on crystallinity, film roughness, and cracking.

The size and the uniformity of the formed aerosol are important factors that determine the quality of the film. They can be influenced by the surface tension, density, and concentration of the precursor liquid, and the pressure of the carrier gas used.

### **1.6.1.2 Mechanism**

The exact mechanism of spray pyrolysis is still somewhat speculative. There are many sub-processes that occur either sequentially or simultaneously, which makes it difficult to model the overall process accurately. The process can be divided in the following steps:

- a) aerosol formation
- b) transport and evaporation
- c) precipitation (reaching the surface)
- d) drying/ decomposition

Prednis and Gauckler describe in their review paper more details about the mechanism by which the metal oxide film is formed at the substrate by using spray pyrolysis [50].

Compared to other deposition techniques, spray pyrolysis (SP) enjoys the advantages of low equipment costs, simple operation, and relatively low deposition temperatures. Another advantage of this technique is the easy incorporation of dopants by adding the desired dopant and its concentration in the precursor solution. Thin films obtained by SP have attracted much attention because of their good electrical and optical properties. Furthermore, the spray pyrolysis technique generally shows good reproducibility, the possibility of depositing large areas in a short time, and a wide variety of materials that can be deposited.

## **1.6.2 Electrodeposition**

Electrodeposition is the process of producing a coating/film on a desired surface from a liquid electrolyte by applying an external electrical current. A schematic drawing of an electrodeposition cell is shown in Figure 1.12. The deposition of the film/coating onto the surface is achieved by putting a negative potential on the electrode to be coated and immersing it into a solution that contains a salt of the metal to be deposited. The metallic ions of the salt carry a positive charge and are thus attracted to the negatively polarized surface/substrate, where they are reduced to form a metallic film. Clearly, the substrate needs to be electrically conductive in order to facilitate the deposition.

The process does not need sophisticated equipment, and by choosing a suitable electrolyte solution good quality films can be obtained in a short time at relatively low temperatures (25 - 80°C). By varying the applied current and the electrolyte solution, as well as the deposition time, various morphologies can be obtained (Chapter 5). More detailed

information on electrodeposition can be found in the book of Pandey that offers an excellent introduction into the topic [51,52].

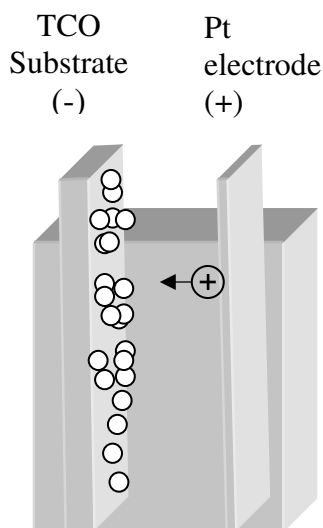


**Figure 1.12:** Schematic drawing of the working principle of electrodeposition.

It is also possible to deposit a semiconductor directly by anodic or cathodic electrodeposition. However, in this thesis the electrodeposition of a metal followed by a thermal oxidation is used because the oxidation conditions are easier to control.

## 1.7 Aim and outline of this thesis

In this thesis semiconductor thin films of three different metal oxides, i.e.  $\text{TiO}_2$ ,  $\text{InVO}_4$ , and  $\text{Fe}_2\text{O}_3$ , are investigated as photoanodes for water splitting. The direction of research ranged from trying to improve the visible-light absorption of  $\text{TiO}_2$ , to preparation of new  $\text{InVO}_4$  catalysts in thin film form, and seeking alternative methods to deposit efficient nanostructured  $\text{Fe}_2\text{O}_3$  photoelectrodes.

The aim of the work presented in this thesis is two-fold. First, the use of low-cost deposition techniques for the preparation of efficient thin-film photoanodes is explored. Special attention is given to the possibility to introduce dopants in a controlled manner. Second, the influence of the presence of ionic point defects on the photoelectrochemical performance of the materials is investigated.

Chapters 2 and 3 present a detailed study on the properties of undoped, Fe-doped, and C doped  $\text{TiO}_2$  films prepared by spray pyrolysis. Cation doping (Fe) is used as a case study and from Mott-Schottky analysis it is shown that it is present as an acceptor-type dopant in  $\text{TiO}_2$ . Carbon doping can, in principle, be used to shift the absorption of  $\text{TiO}_2$  to the visible part of the spectrum without the disadvantages of the more usual cation dopants. Different strategies to introduce carbon as a dopant are investigated.

In Chapter 4, spray pyrolysis is explored as a novel method to produce thin films of InVO<sub>4</sub> at low temperatures. Detailed electrochemical impedance analysis of the prepared electrodes is performed to show the limitations of InVO<sub>4</sub> thin-film photoelectrodes. The presence of deep donor-type defects in the bandgap of the material and their influence on the photoelectrochemical properties are discussed in detail.

In Chapter 5, the focus is on the preparation of nanostructured Fe<sub>2</sub>O<sub>3</sub> electrodes. Electrodeposition is explored as a new method to obtain those photoelectrodes efficiently in a short time and with the possibility to control the morphology. The main goal of the research described in this chapter is to obtain Fe<sub>2</sub>O<sub>3</sub> nanorods perpendicular to the substrate. Such morphology could improve the efficiency of Fe<sub>2</sub>O<sub>3</sub> photoanodes by decreasing the diffusion path length for the photo-generated holes.

## References

- [1]. D. D. Doniger, A. V. Herzog, and D. A. Lashof, *Science*, **314**, 764 (2006).
- [2]. N. S. Lewis and D. G. Nocera, *PNAS*, **103**, 15729 (2006).
- [3]. US Department of Energy, Office of Basic Energy Sciences. Basic research needs for solar energy utilization (report). 2005.
- [4]. E. Wilhelm and M. Fowler, *Bull. Sci. Tech. Soc.*, **26**, 278 (2006).
- [5]. [http: www.eia.doe.gov/](http://www.eia.doe.gov/)
- [6]. [http: www.fuelcellstore.com/information/hydrogen\\_safety.html](http://www.fuelcellstore.com/information/hydrogen_safety.html)
- [7]. A. T-Raissi and D. L. Block, *IEEE power & energy magazine*, **11/12**, 40 (2004).
- [8]. J. D. Holladay, J. Hu, D. L. King, and Y. Wang, *Catal. Today*, **139**, 244 (2009).
- [9]. E. Becquerel, *C. R. Acad. Sci.*, **9**, 145 (1839).
- [10]. A. J. Bard and L. R. Faulkner, *"Electrochemical methods, Fundamentals and Applications"*, John Wiley & Sons, New York (1980).
- [11]. S. R. Morrison, *"Electrochemistry at semiconductor and oxidized Metal Electrodes"*, Plenum Press, New York and London (1980).
- [12]. Y.-M. Chiang, P. B. Dunbar, and W. David Kingery, *Physical Ceramics - Principle for Ceramics Science and Engineering*, John Wiley; Sons, Inc., New York (1997).
- [13]. D. M. Smyth, *The defect chemistry of metal oxides*, Oxford University Press, Inc., New York (2000).
- [14]. H. O. Finklea, *Semiconductors electrodes*, Elsevier, Amsterdam (1988).
- [15]. A. Kudo, K. Omori, and H. Kato, *J. Am. Chem. Soc.*, **121**, 11459 (1999).
- [16]. A. B. Murphy, P. R. F. Barnes, L. K. Randeniya, I. C. Plumb, I. E. Grey, M. D. Horne, and J. A. Glasscock, *Int. J. Hydrogen Energy*, **31**, 1999 (2006).
- [17]. J. R. Bolton, S. J. Strickler, and J. S. Connolly, *Nature*, **316**, 495 (1985).
- [18]. L. A. Harris and R. H. Wilson, *Ann. Rev. Mater. Sci.*, **8**, 99 (1978).
- [19]. M. Nanu, J. Schoonman, and A. Goossens, *Adv. Mater.*, **16**, 453 (2004).
- [20]. Meissner, D. In *Ullmann's Encyclopedia of Industrial Chemistry*; Anonymous Willey-VCH: Germany, 1999; pp 1-11.
- [21]. R. van de Krol, Y. Q. Liang, and J. Schoonman, *J. Mater. Chem.*, **18**, 2311 (2008).
- [22]. A. Fujishima and K. Honda, *Nature*, **238**, 37-38 (1972).
- [23]. O. Khaselev, A. Bansal, and J. A. Turner, *Int. J. Hydrogen Energy*, **26**, 127 (2001).
- [24]. P. A. Lehman, C. E. Chamberlin, G. Pauletto, and M. A. Rocheleau, *Int. J. Hydrogen Energy*, **22**, 465 (1997).
- [25]. G. R. Bamwenda and H. Arakawa, *Sol. Energ. Mat. Sol. C.*, **70**, 1 (2001).
- [26]. H. Yang, L. Guo, W. Yan, and H. Liu, *J. Power Sources*, **159**, 1305 (2006).
- [27]. J. Ye, Z. Zou, H. Arakawa, M. Oshikiri, M. Shimoda, A. Matsushita, and T. Shishido, *J. Photochem. Photobiol. A: Chem*, **148**, 79 (2002).
- [28]. D. Wang, Z. Zou, and J. Ye, *Chem. Phys. Lett.*, **373**, 191 (2003).

- [29]. Z. Zou, J. Ye, and H. Arakawa, *Topics in Catalysis*, **22**, 107 (2003).
- [30]. A. Kudo, *Int. J. Hydrogen Energy*, **31**, 197 (2006).
- [31]. M. Grätzel, *Nature*, **414**, 338 (2001).
- [32]. C. Santato, M. Ulmann, and J. Augustynski, *J. Phys. Chem. B*, **105**, 936 (2001).
- [33]. I. Cesar, A. Kay, J. A. Gonzalez Martinez, and M. Grätzel, *J. Am. Chem. Soc.*, **128**, 4582 (2006).
- [34]. S. Licht, *J. Phys. Chem. B*, **105**, 6281 (2001).
- [35]. S. Licht, B. Wang, S. Mukerji, T. Soga, M. Umeno, and H. Tributsch, *J. Phys. Chem. B*, **104**, 8920 (2000).
- [36]. O. Khaselev and J. A. Turner, *Science*, **280**, 425 (1998).
- [37]. G. K. Boschloo, A. Goossens, and J. Schoonman, *J. Electrochem. Soc.*, **144**, 1311 (1997).
- [38]. R. G. Breckenridge and W. R. Hosler, *Phys. Rev.*, **91**, 793 (1953).
- [39]. *Handbook of Chemistry and Physics*, CRC Press, Boca Raton (1992).
- [40]. R. van de Krol, A. Goossens, and J. Schoonman, *J. Electrochem. Soc.*, **144**, 1723 (1997).
- [41]. N. N. Greenwood and A. Earnshaw, *Chemistry of the Elements*, Butterworth-Heinemann, Oxford (1997).
- [42]. J. H. Kennedy and J. Frese, *J. Electrochem. Soc.*, **125**, 709 (1978).
- [43]. M. P. Dare-Edwards, J. B. Goodenough, A. Hamnett, and P. R. Trevellick, *J. Chem. Soc., Faraday Trans. 1*, **79**, 2027 (1983).
- [44]. L. A. Marusak, R. Messier, and W. B. White, *J. Phys. Chem. Solids*, **41**, 981 (1980).
- [45]. N. C. Debnath and A. B. Anderson, *J. Electrochem. Soc.*, **129**, 2169 (1982).
- [46]. A. Duret and M. Grätzel, *J. Phys. Chem. B*, **109**, 17184 (2005).
- [47]. C. Sanchez, K. D. Sieber, and G. A. Somorjai, *J. Electroanal. Chem.*, **252**, 269 (1988).
- [48]. J. Ye, Z. Zou, M. Oshikiri, A. Matsushita, M. Shimoda, M. Imai, and T. Shishido, *Chem. Phys. Lett.*, **356**, 221 (2002).
- [49]. P. S. Patil, *Mater. Chem. Phys.*, **59**, 185 (1999).
- [50]. D. Perednis and L. J. Gauckler, *J. Electroceram.*, **14**, 103 (2005).
- [51]. R. K. Pandey, *Handbook of semiconductor electrodeposition*, Dekker, New York (1996).
- [52]. R. Greef, R. Peat, and L. M. Peter, *Instrumental methods in electrochemistry*, John Wiley & Sons, New York (1985).

# Chapter 2

## The Photoresponse of Iron- and Carbon-Doped TiO<sub>2</sub> (Anatase) Photoelectrodes \*

### Abstract

*Fe-doped and C-doped anatase TiO<sub>2</sub> films were prepared by spray pyrolysis. For Fe:TiO<sub>2</sub>, a small sub-bandgap photoresponse is observed which is attributed to the presence of additional states located just above the valence band. Although no visible-light photoresponse is observed for carbon-doped TiO<sub>2</sub> due to the low carbon content, the photocurrent at  $h\nu > E_g$  is significantly larger than for undoped TiO<sub>2</sub>. At the same time, the donor density of oxidized C-doped TiO<sub>2</sub> is  $>1.9 \times 10^{19} \text{ cm}^{-3}$ , compared to  $2.5 \times 10^{16} \text{ cm}^{-3}$  for undoped TiO<sub>2</sub>. Assuming that only light absorbed in the depletion layer contributes to the photocurrent, the photoresponse of C-doped anatase (at 330 nm) is 16 times larger than that predicted for undoped TiO<sub>2</sub> under similar conditions. The strong enhancement of the absorption is most likely caused by a change in the electronic structure of the material due to the presence of carbon and/or related defects. Photoluminescence measurements suggest that the defects present in oxidized carbon-doped anatase resemble those present in undoped and reduced TiO<sub>2</sub>.*

---

\* This chapter is based on: Cristina S. Enache, Joop Schoonman, and Roel van de Krol, *Journal of Electroceramics*, **13** (2004), 117-182.

## 2.1 Introduction

In 1972, Fujishima and Honda first demonstrated that water could be split into hydrogen and oxygen at a TiO<sub>2</sub> (rutile) photoanode under illumination with ultraviolet light [1]. Since then, many other photoelectrode materials have been investigated, but wide-bandgap transition metal oxides, in particular TiO<sub>2</sub>, remain popular because of their high photochemical stability. A substantial part of the research on photocleavage of water by TiO<sub>2</sub> has been devoted to the use of transition metal dopants to improve the visible light photoresponse. These dopants introduce additional energy levels in the bandgap, so that sub-bandgap illumination can be used to excite electrons to the conduction band. While this works in principle, the efficiency of transition metal-doped photoelectrodes is still too low for practical use.

The prospect of a future ‘Hydrogen Economy’ has renewed interest in the photocatalytic splitting of water. Recently, Asahi et al. showed that anion dopants can also be used to sensitize TiO<sub>2</sub> to visible light [2]. Promising results have already been obtained for anatase TiO<sub>2</sub> doped with nitrogen [3], and for rutile TiO<sub>2</sub> doped with carbon [4] or sulfur [5]. The p-orbitals of these anions show significant overlap with the valence band O-2p orbitals, which facilitates the transport of photo-generated charge carriers to the surface of the catalyst [2]. In contrast, transition metal dopants generally have strongly localized d-states deep in the bandgap. These often act as recombination centers and slow down hole transport.

In this work, the photoelectrochemical properties of iron- and carbon-doped anatase TiO<sub>2</sub> photoelectrodes are investigated. Compared to rutile TiO<sub>2</sub>, the anatase phase is preferred because of its higher photocatalytic activity [6]. The results will be discussed in relation to the ionic defects present in the material, an important aspect that is often ignored in studies on metal oxide photoelectrodes.

## 2.2 Experimental details

### 2.2.1 Film preparation

Spray Pyrolysis (SP) was used to prepare undoped and Fe- and C-doped TiO<sub>2</sub> thin films. The precursor solution consisted of 2.4 ml TTiP (titanium-tetraisopropoxide, 99.999%) in 54 ml ethanol (>99.9%), with 3.6 ml acetyl-acetonate (99+%) added to prevent cracking of the films. Iron (Fe) was introduced as a dopant by adding iron nitrate (Fe(NO<sub>3</sub>)<sub>3</sub>) in a ratio of Fe:Ti = 0.01. Carbon is incorporated as dopant by carrying out the deposition under a mixed CO<sub>2</sub>/O<sub>2</sub> atmosphere. The substrate temperature was 350 °C, and a 3 s on, 60 s off spraying-cycle was used. The film thickness was typically 100±20 nm. F:SnO<sub>2</sub> on glass (Libbey Owens Ford) and fused silica (quartz, ESCO S1-UV) were used as substrates.

### 2.2.2 Characterization techniques

The surface morphology of doped and undoped TiO<sub>2</sub> films was characterized using a high-resolution scanning electron microscope equipped with a field emission gun (Philips XL-SFEG). Acceleration voltages between 5 and 30 kV were used.

Optical transmission and reflection spectra of the deposited films were recorded using a Perkin-Elmer Lambda 900 spectrophotometer, equipped with an integrating sphere (Labsphere).

Photoelectrochemical measurements were performed using a three-electrode cell with a platinum counter electrode and a saturated calomel reference electrode (SCE). An aqueous solution of 0.1M KOH was used as an electrolyte. The potentiostat (Solartron 1286) used for current measurements was combined with a frequency response analyser (Solartron 1250) for impedance measurements. A 200 W tungsten halogen lamp in combination with a grating monochromator (Acton SPro 150) was used to irradiate the sample. High-pass filters (Schott) were used to remove the second order of the diffracted light. The light intensity was measured as a function of wavelength with a calibrated photodiode (PD 300-UV, Ophir).

The Raman spectra were recorded with a home-built setup using a continuous-wave Nd:YVO<sub>4</sub> laser with a wavelength of 532 nm (Millennia, Spectra Physics). The backscattered light was recorded by a CCD camera, cooled with liquid nitrogen (model LN/CCD-1100PB, Princeton Instruments), via a monochromator (model 340E, Spex) having an 1800 grooves/mm grating.

Photoluminescence (PL) measurements were recorded with a home-built set-up using a pulsed Nd:YAG (yttrium-aluminium-garnet) laser (Spectra Physics) with a wavelength of 355 nm. The spectra were recorded in the back-scatter mode using a CCD camera cooled with liquid nitrogen (LN/CCD-1100PB, Princeton Instruments) and a grating monochromator (Spex 340E). Stray laser light was removed with two Supernotch filters (Kaiser Optical Systems). Corrections for the sensitivity of the CCD camera, monochromator, filters were applied, and the luminescence intensity,  $W(\lambda)$ , was converted to spectral density as a function of energy,  $W(E)$ , by multiplying with a factor of  $\lambda^2$  [7]. For low-temperature measurements a closed-cycle helium cryostat (APD Cryogenics CSW 204SL-6.5K) was used. The luminescence remains detectable up to room temperature for both undoped and doped TiO<sub>2</sub>. All the luminescence peaks are fitted with Gaussian peak profiles.

## 2.3 Results and discussion

### 2.3.1 Morphology of the films

All deposited films are optically transparent, uniform, smooth, crack-free, and well adherent to the transparent conductive substrate, as can be observed in Figure 2.1A, B. The films consist of small crystallites preferentially spherically shaped. The small variation in thickness is caused by the roughness of the substrate (Figure 2.1C, D).

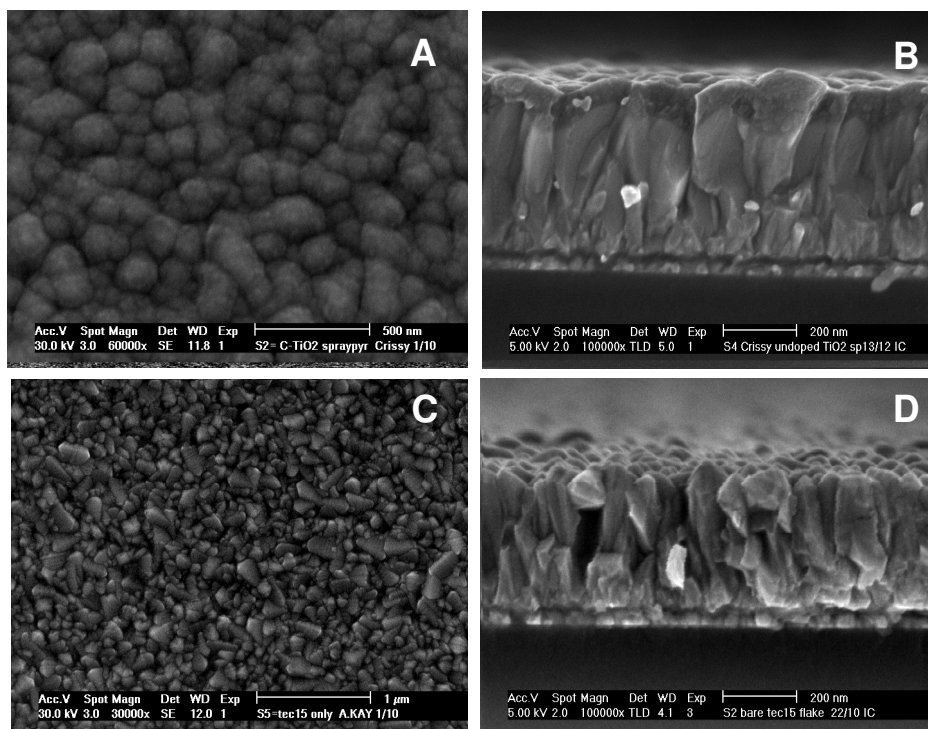


**Figure 2.1:** Scanning electron microscopy (SEM) images of undoped  $\text{TiO}_2$  films (A, B) deposited by spray pyrolysis; B) cross-section of undoped  $\text{TiO}_2$  deposited on conductive glass; C, D) transparent conductive glass substrate (F:  $\text{SnO}_2$ -glass coated) top view and cross-section, respectively.

In Figure 2.1B the slightly darker surface represents the deposited  $\text{TiO}_2$  film and can be clearly distinguished from the conductive substrate (lighter). A film thickness of  $\sim 100 \pm 20$  nm is estimated from the SEM cross-section images for undoped as well as C-doped  $\text{TiO}_2$  electrodes. There is no difference in the film morphology for Fe- or C-doped  $\text{TiO}_2$  films. Intermediate annealing steps under reducing or oxidizing atmospheres do not change the morphology of those films.

### 2.3.2 Structure characterization

Grazing-incidence X-ray diffraction (GI-XRD) (not shown) and Raman spectroscopy are used to investigate the crystal structure of the undoped and doped  $\text{TiO}_2$  films. As shown in Figure 2.2 as-deposited films are crystalline with clear anatase peaks. A post-deposition anneal at  $450^\circ\text{C}$  in air further improves the crystallinity of the films. Subsequent reduction of the Fe-doped films in an  $\text{Ar:H}_2$  (10:1) mixture results in an anatase-to-rutile phase transformation, which has also been observed by Bally et al. [8]. No transformation to rutile is observed during a thermal anneal under oxidizing conditions. Furthermore, no traces of rutile or any other intermediate phases are observed after oxidation or reduction of undoped or C-doped anatase  $\text{TiO}_2$  films. More details on this topic are presented also in Chapter 3, which contains a detailed XRD study of C-doped and undoped  $\text{TiO}_2$  samples oxidized at different temperatures.

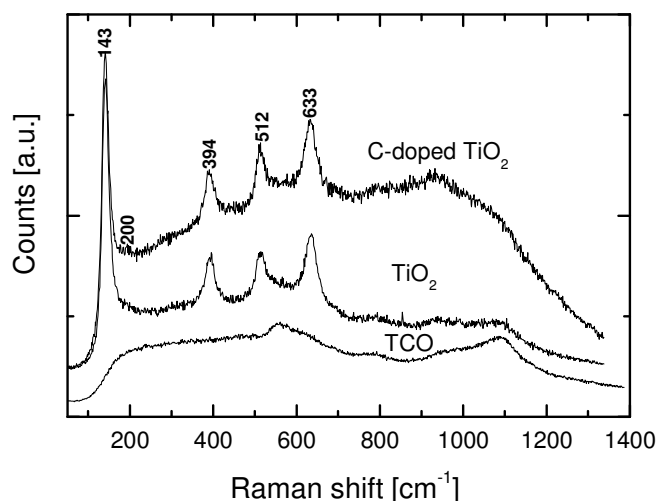


**Figure 2.2:** Raman spectra of undoped and C-doped TiO<sub>2</sub> films, deposited on transparent conductive oxide (F: SnO<sub>2</sub>) at a substrate temperature of 350 °C. The indicated peaks correspond to anatase TiO<sub>2</sub>. For reference the Raman spectrum of the transparent conductive substrate (F:SnO<sub>2</sub>) is shown.

### 2.3.3 Photoelectrochemical properties

To investigate the influence of the Fe and C dopant on the optical properties of TiO<sub>2</sub>, photocurrent spectra are recorded. The incident photon-to-current conversion efficiencies (IPCE) of undoped and C-doped TiO<sub>2</sub> are shown in Figure 2.3. The insert reveals an indirect bandgap of  $3.26 \pm 0.05$  eV for undoped anatase TiO<sub>2</sub>, in excellent agreement with previously reported values [9,10]. For Fe-doped TiO<sub>2</sub>, a small photocurrent is observed just below the bandgap. Bally et al. [8] observed a similar effect and attributed it to the presence of rutile, which has a smaller bandgap than anatase ( $E_{g, \text{rutile}} = 3.05$  eV [11]). In our case, however, X-ray diffraction and Raman spectroscopy reveal no traces of rutile in the oxidized Fe:TiO<sub>2</sub> samples. A more likely explanation is that the Fe<sup>3+</sup> dopants introduce sub-bandgap energy levels in anatase, located just above the valence band, from which electrons can be excited. A similar explanation has been offered for the small sub-bandgap photocurrents observed in Fe-doped rutile [12,13].

In the case of C-doped anatase TiO<sub>2</sub> films, no photocurrent is observed in the visible part of the spectrum. Khan et al. observed significant optical absorption at  $h\nu > 2.32$  eV for rutile TiO<sub>2</sub> heavily doped with carbon [4]. They also observed larger photocurrents than for undoped TiO<sub>2</sub> under white light illumination. Although one cannot directly compare optical absorption spectra to photocurrent action spectra (not all absorbed photons will result in an external current), a comparison with the results of Khan et al. shows that the optical absorption of the present carbon-doped anatase is markedly different from that of carbon-doped rutile TiO<sub>2</sub>. A further observation from Figure 2.3 is that the band-to-band absorption ( $h\nu > 3.2$  eV) of C-doped anatase is  $\sim 2.4$  times stronger than that of undoped anatase. In a recent publication, Sakthivel et al. [14] also observed an enhanced UV photoresponse without any visible-light photoresponse for anatase TiO<sub>2</sub> containing 0.03% carbon. Since larger

concentrations of carbon (e.g. 0.42%) do lead to a visible-light photoresponse [14], we conclude that the carbon content in our films is (too) low.

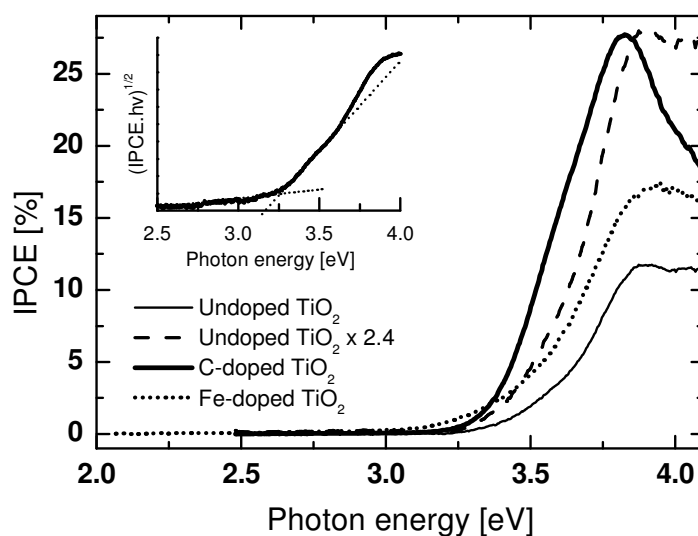


**Figure 2.3:** Photocurrent action spectra of undoped, iron- and carbon-doped anatase  $\text{TiO}_2$ , recorded at a potential of 0 V vs. SCE. All the samples are post-annealed at 450 °C for 6h to ensure that the measurements are performed on stable and crystalline samples. The insert shows the photocurrent spectra of undoped  $\text{TiO}_2$ , plotted as  $(\text{IPCE}\cdot h\nu)^{1/2}$  vs.  $h\nu$  to determine the bandgap of the  $\text{TiO}_2$

## 2.3.4 Defect characterization

### 2.3.4.1 Mott-Schottky measurements

The film thickness of C-doped  $\text{TiO}_2$  is approximately equal to that of undoped  $\text{TiO}_2$ , so this cannot explain the large increase in the UV photocurrent. However, if the minority carrier diffusion length is much smaller than the film thickness, as is generally the case in polycrystalline oxide semiconductors, the relevant parameter is not the film thickness but the depletion layer width, since only the photons that are absorbed in the depletion layer will contribute to the photocurrent. To determine the width of the depletion layer, capacitance measurements are carried out. The impedance spectrum shown in Figure 2.4 reveals that the response of the system is purely capacitive between 100 Hz and 50 kHz, and it is assumed that the overall response is dominated by the space charge capacitance. This allows us to determine the donor density and the space charge width from Mott-Schottky measurements [15].

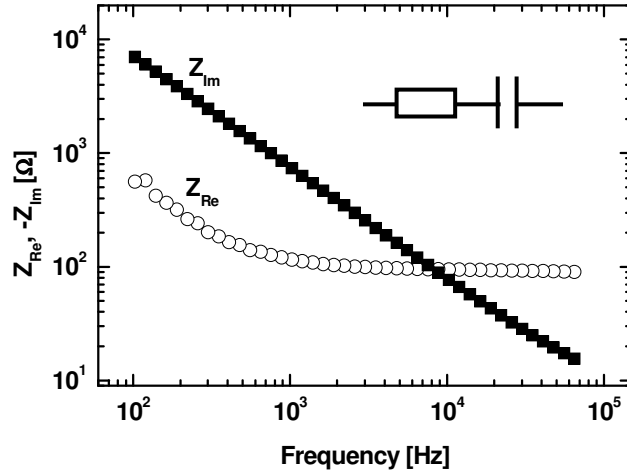


**Figure 2.4:** Electrochemical impedance spectrum (Bode plot representation) of undoped TiO<sub>2</sub> at 0 V vs. SCE, indicating the frequency range in which reliable Mott-Schottky data can be measured. The real part of the impedance ( $Z_{Re}$ ) is indicated by open circles, and the imaginary part ( $Z_{Im}$ ) by filled squares. The real part of the impedance at low frequencies represents the combined resistance of the leads, electrolyte, contacts, and TiO<sub>2</sub> bulk resistance ( $\sim 100 \Omega$ ).

The Mott-Schottky curves for undoped and carbon-doped anatase TiO<sub>2</sub>, both oxidized in air, are shown in Figure 2.5. The donor density,  $N_D$ , can be calculated from the slope of the curve according to:

$$\frac{1}{C^2} = \frac{2}{eN_D\epsilon_0\epsilon_r A^2} \left( \phi - \phi_{fb} - \frac{kT}{e} \right) \quad (2.1)$$

Here,  $C$  is the capacitance,  $\phi$  the applied potential,  $\phi_{fb}$  the flat band potential,  $A$  the surface area ( $=2.83 \times 10^{-5} \text{ m}^2$ ),  $\epsilon_r$  the relative dielectric constant ( $=55$  [15]), and all other symbols have their usual meaning.

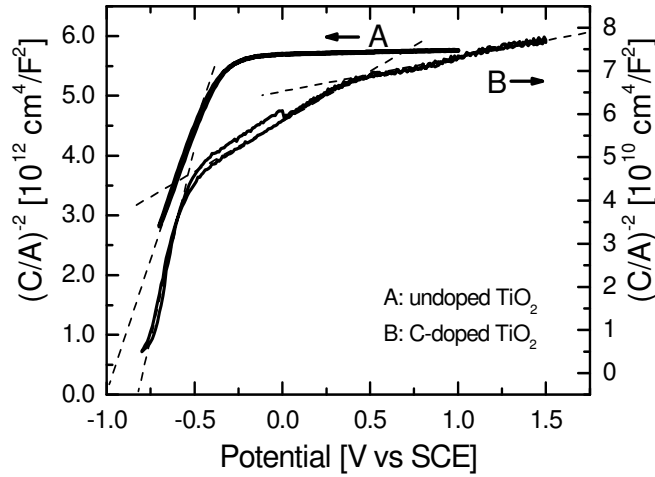


**Figure 2.5:** Mott-Schottky plots of undoped and carbon-doped anatase  $\text{TiO}_2$  (both oxidized at  $450\text{ }^\circ\text{C}$  in air), recorded with frequencies of 12 kHz and 2 kHz, respectively. The perturbation amplitude is 10 mV and the scan rate 10 mV/s.

The flatband potential ( $\phi_{\text{fb}}$ ) for undoped  $\text{TiO}_2$  is  $-1.06\text{ V vs. SCE}$ , in good agreement with previous reports [15,16]. For the C-doped film,  $\phi_{\text{fb}}$  is shifted to a  $\sim 0.2\text{ V}$  more positive value, i.e.,  $-0.83\text{ V vs. SCE}$ . The origin of this shift is not clear and calls for further investigation.

For as-deposited undoped  $\text{TiO}_2$  a donor density of  $1.5 \times 10^{19}\text{ cm}^{-3}$  is found. This value decreases to  $3.2 \times 10^{17}\text{ cm}^{-3}$  after oxidation for 6 hours at  $450\text{ }^\circ\text{C}$  in air (curve A). After an additional 12 hour post-deposition anneal treatment at  $450\text{ }^\circ\text{C}$ , the donor density decreases by another order of magnitude. These values are about as low as can be achieved for this oxide and demonstrates the high film quality that can be obtained with spray pyrolysis. The horizontal part of the curve at  $\phi > -0.2\text{ V vs. SCE}$  indicates that the film is fully depleted, as described in detail elsewhere [15]. From this plateau value of the capacitance curve the film thickness can be calculated using the formula:

$$d = \frac{\epsilon_0 \epsilon_r A}{C} \quad (2.2)$$

A value of  $\sim 115\text{ nm}$  is obtained, in good agreement with the thickness determined from the cross-section of the scanning electron microscopy image (Fig. 2.1B).

For the carbon-doped  $\text{TiO}_2$  (curve B), three distinct slopes are observed, corresponding to donor densities of  $1.9 \times 10^{19}\text{ cm}^{-3}$ ,  $1.0 \times 10^{20}\text{ cm}^{-3}$ , and  $2.8 \times 10^{20}\text{ cm}^{-3}$  (from left to right). These values are more than two orders of magnitude higher than for undoped  $\text{TiO}_2$ , despite the fact that both films have been oxidized at  $450\text{ }^\circ\text{C}$  in air. The non-uniform donor density indicates segregation of shallow donors or compensating acceptors away from or towards the surface, respectively. Before the post-deposition thermal anneal, the carbon-doped films show only a single slope, corresponding to a donor density of  $\sim 10^{18}\text{ cm}^{-3}$ . Hence, the post-deposition thermal-anneal results in a segregation of dopants and a large increase in the density of shallow donors close to the surface. The origin of the shallow donors in anatase  $\text{TiO}_2$  is still

under debate, both oxygen vacancies or titanium interstitials have been proposed [17]. While the high donor density in carbon-doped anatase TiO<sub>2</sub> can most likely be attributed to one of these native defects, the possibility that carbon itself acts as a shallow donor cannot be entirely dismissed.

The high donor density implies a small depletion layer width,  $w$ , which can be calculated with:

$$w = \sqrt{\frac{2\epsilon_0\epsilon_r}{eN_D} \left( \phi - \phi_{fb} - \frac{kT}{e} \right)} \quad (2.3)$$

At 0 V *vs.* SCE, the potential at which the Mott-Schottky plots in Figure 2.5 are recorded, the depletion layer widths for undoped and C-doped TiO<sub>2</sub> are ~115 nm (i.e., full depletion) and ~12 nm, respectively (calculated using equation 2.3). The fraction of the incident light absorbed in the depletion layer,  $f$ , can be calculated using Beer's law:

$$f(\alpha, w) = \frac{\int_0^w I_0 e^{-\alpha z} dz}{\int_0^\infty I_0 e^{-\alpha z'} dz'} = (1 - e^{-\alpha w}) \quad (2.4)$$

Here,  $\alpha$  is the absorption coefficient and  $I_0$  the light intensity at  $z=0$ . Here, we assume that: i) only the light absorbed in the space charge (SC) region contributes to the photocurrent, and ii) all the light absorbed in the space charge region contributes to the photocurrent. With  $\alpha \approx 9 \times 10^6 \text{ m}^{-1}$  at 330 nm for anatase TiO<sub>2</sub> [18],  $f(\alpha, w)$  is ~10% for the C-doped TiO<sub>2</sub>, and ~66% for undoped film. Therefore, the photocurrent of C-doped TiO<sub>2</sub> at 330 nm is expected to be ~6.6 times smaller than that of undoped TiO<sub>2</sub>. This factor is based solely on the values of  $w$  and  $\alpha$ , assuming as we mentioned above that the photocurrent originates entirely from the photo-generated electron-hole pairs in the depletion layer.

To investigate why the measured photocurrents for carbon-doped anatase TiO<sub>2</sub> are ~2.4×6.6=16 times higher (at 330 nm) than expected, two material parameters need to be considered. The first parameter is the dielectric constant of the material, which was assumed to be the same as that for undoped TiO<sub>2</sub>. If one or more of the defects introduced by the carbon dopant results in an increase in the dielectric constant, as is observed for anatase TiO<sub>2</sub> doped with Li [19] or H [20], the actual donor density is much smaller, and the depletion layer width is much larger than the values calculated above. While this effect may indeed occur, a larger value of  $w$  for the C-doped TiO<sub>2</sub> films does not explain a 2.4 times higher value for the measured photocurrent, since Figure 2.5 shows that the undoped TiO<sub>2</sub> is fully depleted at 0 V *vs.* SCE. Further work is in progress to determine the actual value of the dielectric constant of C-doped TiO<sub>2</sub>. For this, thinner films with a well known thickness are being used, following our previously reported approach [15].

The second parameter is the optical absorption coefficient of C-doped TiO<sub>2</sub>. Asahi et al. calculated the density of states before and after substitutional doping of carbon on the oxygen anion sites in anatase TiO<sub>2</sub> [2]. Their calculations suggest the presence of additional states in

the bandgap at  $\sim 1$  eV above the valence band, which is consistent with the visible-light photoresponse observed by others [4,14]. However, no additional states were found that could explain the enhanced photocurrents at energies  $>3.2$  eV. Therefore, it seems more likely that the enhanced photocurrent is related to changes in the electronic structure caused by other defects which are simultaneously introduced with carbon in order to satisfy the conservation of mass, charge, and lattice sites. Alternatively, carbon itself may reside on other sites than the oxygen anion sites, since it can have many different oxidation states and corresponding ionic radii.

#### **2.3.4.2 Photoluminescence characterization**

##### *General aspects*

Many important properties of metal oxide photoelectrodes, such as optical absorption and electronic charge transport, are determined by the nature and concentration of ionic point defects. Examples of ionic point defects in  $\text{TiO}_2$  are oxygen vacancies, titanium interstitials, and deliberately added dopants (C) that occupy either interstitial or substitutional lattice sites. To reveal the nature of the defects involved in undoped and doped anatase  $\text{TiO}_2$ , low-temperature photoluminescence (PL) measurements have been carried out. PL can be observed when an excited electron in the conduction band recombines with a hole in the valence band. Alternatively, the electron may become trapped at a defect (e.g. an impurity/dopant or an oxygen vacancy) at an energy level somewhere within the bandgap. This may also give rise to a PL signal, although it should be noted that non-radiative recombination is perhaps even more common. The energy of the emitted radiation can provide information on the nature of the defects involved. In an indirect semiconductor (for example  $\text{TiO}_2$ ), electrons and holes relax to the bottom of their bands by phonon emission before recombining by emitting a photon [21]. As a consequence, PL signals of indirect semiconductors are usually quite weak. In practice, luminescence processes that involve defects can be quite complicated and depend on the material investigated.

##### *Photoluminescence of undoped and C-doped $\text{TiO}_2$*

The photoluminescence measurements performed for undoped and C-doped  $\text{TiO}_2$  anatase using 355 nm (3.49 eV) irradiation, which is  $\sim 0.2$  eV above the band edge absorption of  $\text{TiO}_2$ , are shown in Figure 2.6. For undoped  $\text{TiO}_2$ , three peaks are observed. The peak at  $\sim 2.4$  eV is attributed to self-trapped excitons (STEs) [9,22,23]. Oxidation (A) or reduction (B) treatments do not significantly affect this peak, confirming its intrinsic character. The peak at  $\sim 2$  eV increases in intensity after reduction, and may be related to oxygen vacancies/ titanium interstitials, or excitons bound to one of these defects. The broadening of this peak indicates an increase in the amount of disorder due to the increase in the number of defects upon reduction. The peak at  $\sim 1.6$  eV is significantly shifted and virtually disappears after reduction. Hence, it is reasonable to assume that this peak is also related to the presence of ionic point defects, or to excitons bound to these defects. Since titanium vacancies are the only defects in

undoped TiO<sub>2</sub> whose concentration increases with increasing oxygen partial pressure [24], we tentatively attribute the 1.6 eV peak to the presence of titanium vacancies.

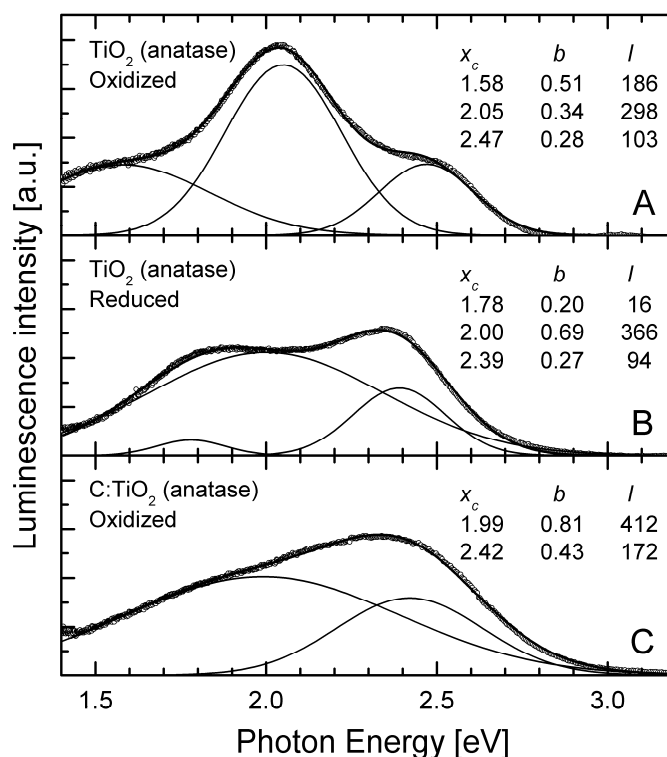


**Figure 2.6:** Photoluminescence spectra of undoped and carbon-doped anatase TiO<sub>2</sub>, measured at 10 K. Oxidation took place at 450 °C in air, reduction at 450 °C in an Ar/H<sub>2</sub> (10:1) mixture. The excitation wavelength is 355 nm (3.49 eV). The open circles are the measured data and the solid lines represent a fit of the data with Gaussian-shaped curves. The position ( $x_c$ ), width ( $b$ ), and integrated intensity ( $I$ ) of the individual peaks are indicated.

The PL of oxidized carbon-doped anatase TiO<sub>2</sub> only shows the two peaks at 1.99 and 2.42 eV, indicating the presence of oxygen vacancies (and/or titanium interstitials) and STEs, respectively, Figure 2.6C. The integrated intensities and widths of these peaks are significantly larger than those of reduced undoped TiO<sub>2</sub>, indicating a large number of defects and substantial disorder. It should be noted that this disorder is not related to a decrease in the crystallinity, since XRD analysis shows well-defined anatase diffraction peaks for the carbon-doped samples. The similarities in the PL spectra of reduced undoped TiO<sub>2</sub> and oxidized carbon-doped TiO<sub>2</sub> suggest that the same types of defects are present. This provides an important clue for further work aimed to unravel the defect chemistry of carbon-doped anatase TiO<sub>2</sub>. For clarity a summary of the luminescence peaks discussed in Figure 2.6 is presented in Figure 2.7 to offer an easy illustrative image of peak variation in different TiO<sub>2</sub> thin film samples.

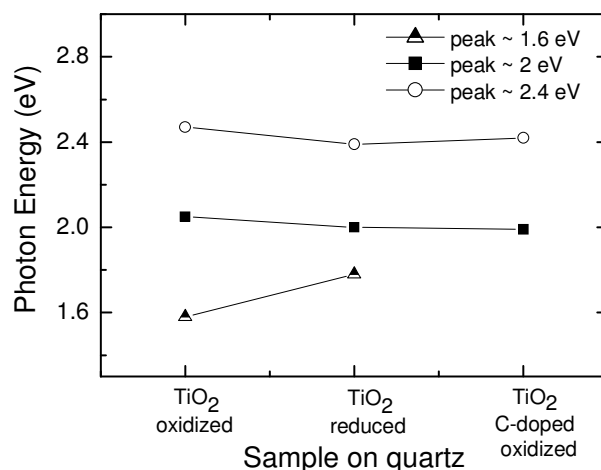


**Figure 2.7:** Variations of the luminescence peak positions for various anatase TiO<sub>2</sub> thin film samples measured at 3.49 eV laser irradiation.

It should be noted that many of the more subtle features in the luminescence spectra only become apparent after applying the various corrections from  $I/d\lambda$  to  $E/dE$  with the factor  $\lambda^2$ . In most articles on the luminescence of anatase TiO<sub>2</sub> these corrections were not carried out, and only a single, broad emission band around 2.3-2.4 eV attributed to the self-trapped excitons was observed when excitation energy above the optical bandgap was used (>3.2 eV) [9,23,25,26].

## 2.4 Conclusions

High quality undoped and iron- and carbon-doped TiO<sub>2</sub> thin films have been prepared by Spray Pyrolysis. As deposited films are crystalline and the post-deposition anneal does not change the morphology. The small, sub-bandgap photocurrent observed for Fe-doped anatase TiO<sub>2</sub> can be explained by Fe<sup>3+</sup> dopants introducing additional energy levels in the bandgap, just above the valence band.

The photoelectrochemical properties of carbon-doped anatase TiO<sub>2</sub> have been investigated for the first time. Little or no photocurrent is observed in the visible part of the spectrum, which is attributed to a (too) low carbon content. However, the photocurrent due to band-to-band excitation is significantly higher than that of undoped TiO<sub>2</sub>, despite the high donor density and correspondingly small depletion layer in oxidized, C-doped anatase TiO<sub>2</sub>. The origin of the enhanced photocurrent is most likely a change in the electronic structure of the material due to the incorporation of carbon and/or related defects. Although the exact nature and concentration of these defects is not known, photoluminescence measurements suggest that defects in oxidized carbon-doped anatase closely resemble those present in undoped and reduced TiO<sub>2</sub>. Further work is aimed to determine the dielectric constant of C-doped anatase and to measure and control the concentration of carbon. Detailed knowledge of these parameters is required for a better understanding of the optical properties and defect chemistry of carbon-doped anatase TiO<sub>2</sub>.

## References

- [1]. A. Fujishima and K. Honda, *Nature*, **238**, 37-38 (1972).
- [2]. R. Asahi, T. Morikawa, T. Ohwaki, K. Aoki, and Y. Taga, *Science*, **293**, 269 (2001).
- [3]. T. Morikawa, R. Asahi, T. Ohwaki, K. Aoki, and Y. Taga, *Jpn. J. Appl. Phys. 2*, **40**, L561 (2001).
- [4]. S. U. M. Khan, M. Al Shahry, and W. B. Ingler, Jr., *Science*, **297**, 2243 (2002).
- [5]. T. Umebayashi, T. Yamaki, H. Itoh, and K. Asai, *Appl. Phys. Lett.*, **81**, 454 (2002).
- [6]. A. L. Linsebigler, G. Lu, and J. T. Yates, *Chem. Rev.*, **95**, 735 (1995).
- [7]. G. Blasse and B. C. Grabmaier, *Luminescent materials*, Springer (1994).
- [8]. A. R. Bally, E. N. Korobeinikova, P. E. Schimid, F. Lévy, and F. Bussy, *J. Phys. D: Appl. Phys.*, **31**, 1149 (1998).
- [9]. H. Tang, K. Prasad, R. Sanjines, P. E. Schimid, and F. Levy, *J. Appl. Phys.*, **75**, 2042 (1994).
- [10]. H. Minoura, M. Nasu, and Y. Takahashi, *Phys. Chem.*, **89**, 1064 (1985).
- [11]. H. Tang, F. Levy, H. Berger, and P. E. Schimid, *Phys. Rev. B*, **52**, 7771 (1995).
- [12]. H. P. Maruska and A. K. Ghosh, *Solar Energy Mater.*, **1**, 237 (1979).
- [13]. K. Mizushima, M. Tanaka, A. Asai, S. Iida, and J. B. Goodenough, *J. Phys. Chem. Solids*, **40**, 1129 (1979).
- [14]. S. Sakthivel and H. Kisch, *Angew. Chem. Int. Ed.*, **42**, 4908 (2003).
- [15]. R. van de Krol, A. Goossens, and J. Schoonman, *J. Electrochem. Soc.*, **144**, 1723 (1997).
- [16]. F. Möllers, H. J. Tolle, and R. Memming, *J. Electrochem. Soc.*, **121**, 1160 (1974).
- [17]. P. Knauth and H. L. Tuller, *J. Appl. Phys.*, **85**, 897 (1998).
- [18]. H. Takikawa, T. Matsui, T. Sakakibara, A. Bendavid, and P. J. Martin, *Thin Sol. Fi.*, **348**, 145 (1999).
- [19]. R. van de Krol, A. Goossens, and J. Schoonman, *J. Phys. Chem. B*, **103**, 7151 (1999).
- [20]. M. F. Weber, L. C. Schumacher, and M. J. Dignam, *J. Electrochem. Soc.*, **129**, 2022 (1982).
- [21]. F. Mark, *Optical Properties of Solids*, Oxford University Press, New York (2001).
- [22]. N. Hosaka, *J. Lumines.*, **72-74**, 874 (1997).
- [23]. M. Watanabe, S. Sasaki, and T. Hayashi, *J. Lumines.*, **87-9**, 1234 (2000).
- [24]. D. M. Smyth, *The defect chemistry of metal oxides*, Oxford University Press, Inc., New York (2000).
- [25]. M. Watanabe, T. Hayashi, H. Yagasaki, and S. Sasaki, *Int. J. Mod. Phys. B*, **28**, **29&30**, 3997 (2001).
- [26]. T. Sekiya, S. Kamei, and S. Kurita, *J. Lumines.*, **87-89**, 1140 (2000).



# Chapter 3

## **Addition of Carbon to Anatase TiO<sub>2</sub> by *n*-hexane treatment – surface or bulk doping? \***

### **Abstract**

*Anatase TiO<sub>2</sub> can be sensitized to visible light by adding carbon as a dopant. Towards this end, TiO<sub>2</sub> photoelectrodes were subjected to a thermal treatment in a hexane-rich environment. By comparing the optical and photoelectrochemical characteristics of both thin films and nanocrystalline nanoporous photoelectrodes, carbon is found to be located mainly at the surface of the TiO<sub>2</sub>. The amount of carbon that diffuses into the bulk of the material is too small to significantly enhance the visible light response and only a small shift of the absorption edge towards higher wavelengths is observed. The presence of carbon in TiO<sub>2</sub> shifts the anatase-to-rutile transformation temperature beyond 800 °C, and X-ray diffraction shows that spray deposition of TiO<sub>2</sub> under a CO<sub>2</sub> atmosphere results in a higher bulk carbon concentration than a post-deposition thermal treatment in a hexane-rich environment.*

---

\* This chapter is based on: Cristina S. Enache, Joop Schoonman, and Roel van de Krol, *Applied Surface Science*, **252** (2006), 6342-6347.

### 3.1 Introduction

Transition metal oxide photoelectrodes continue to receive widespread attention because they appear to be the only low-cost and stable class of materials that enables photo-assisted splitting of water. Titanium dioxide ( $\text{TiO}_2$ ) is a particularly interesting photocatalyst due to its high catalytic activity and excellent photochemical stability. However, it only absorbs in the near UV region of the solar spectrum due to its large band gap (3.2 eV). UV radiation represents only 4% of the incoming solar energy and, therefore, considerable efforts have been directed to extend the absorption of  $\text{TiO}_2$  towards the visible part of the solar spectrum. Numerous attempts have been made during the last three decades to enhance the visible light absorption of  $\text{TiO}_2$  by introducing cation dopants, for example Fe [1,2], Cr [3,4], and V [5]. These dopants introduce additional energy levels in the bandgap from which electrons can be excited into the conduction band with less energy than is needed for band-to-band excitation. Unfortunately, the localized nature of these electronic states presents two problems: i) it prevents efficient transport of photo-generated holes to the surface of the photoelectrodes (holes have to ‘hop’ from one dopant site to the next), and ii) the energy levels of these states are often located deep within the bandgap, which makes them efficient recombination centers [6]. Clearly, efficient sensitization of  $\text{TiO}_2$  to visible light requires a different approach.

Recently, various anion dopants, such as carbon [7-11], nitrogen [12-20], and sulfur [21-23] have been shown to significantly enhance the visible light absorption of  $\text{TiO}_2$ . Theoretical calculations by Asahi et al. [12] suggest that the p-orbitals of these anions, which were assumed to reside on the oxygen sites, show a significant overlap with the O-2p orbitals from the valence band of  $\text{TiO}_2$ . This orbital overlap should facilitate hole transport, while the less localized nature of the anion dopants would limit the amount of recombination.

Most studies on carbon-doped  $\text{TiO}_2$  have been carried out on suspensions of nano- or micro-sized particles [8-11,24-26]. In contrast, the number of reports on carbon-doped  $\text{TiO}_2$  photoelectrodes is limited [7,27]. Recently, we reported on the deposition of dense carbon-doped anatase  $\text{TiO}_2$  thin films prepared by spray pyrolysis of an ethanolic titanium(IV)-tetra-isopropoxide solution under a  $\text{CO}_2$  atmosphere [28]. More details are presented in Chapter 2 of this thesis. The use of the thin dense films allowed us to measure, for the first time, photocurrent and donor densities of carbon-doped  $\text{TiO}_2$ . The carbon-doped  $\text{TiO}_2$  photoelectrodes showed a significant increase of the photocurrent in the UV region compared to undoped  $\text{TiO}_2$ . However, no photocurrent was observed in the visible part of the spectrum due to a too low carbon content [8]. Here, we report on our study to incorporate carbon into anatase  $\text{TiO}_2$  by a post-deposition thermal treatment in an argon/hexane gas mixture. Special attention will be given to the high-temperature stability of these hexane-treated photoelectrodes under oxidizing conditions.

## 3.2 Experimental details

### 3.2.1 Film preparation

#### *Thin dense $\text{TiO}_2$ films*

Spray Pyrolysis (SP) was used to prepared undoped  $\text{TiO}_2$  thin films. The precursor solution consisted of 1.8 ml TTiP (titanium(IV)-tetra-isopropoxide, 99+%, Acros Organics) in 27 ml ethanol (>99.9%, J.T. Baker) with 1.2 ml 2,4-pentanedione (99+%, Aldrich) added to prevent cracking of the films [29]. The substrate temperature was 350 °C, and a 3s on, 60s off spraying-cycle was used to allow the solvent to evaporate before depositing the next layer. The film thickness was typically  $200 \pm 20$  nm. The films were deposited on 1 mm thick fused silica (quartz) substrates (Heraeus, Suprasil 1) for optical characterization and on transparent conducting glass ( $15 \Omega \text{ cm}^{-2}$  F:SnO<sub>2</sub>, TEC 15, Libbey-Owens-Ford) for photoelectrochemical studies.

#### *Nanocrystalline $\text{TiO}_2$ films*

Nanocrystalline nanoporous (mesoporous) films with a thickness of 1  $\mu\text{m}$  were prepared by doctor-blading a paste of 9 nm  $\text{TiO}_2$  particles (Solaronix, surface area  $165 \text{ m}^2 \text{ g}^{-1}$ ) onto the spray-deposited thin film samples described above. The underlying dense  $\text{TiO}_2$  film is necessary to avoid direct contact and, therefore, high leakage currents between the aqueous electrolyte and the conducting F:SnO<sub>2</sub> substrate.

### 3.2.2 Experimental set-up for the annealing treatment

All films are subjected to a post-deposition annealing procedure at 450 °C in air for 6 hours in order to further improve the stoichiometry and crystallinity, and to sinter the particles in case of the mesoporous films. To incorporate carbon, the films were annealed in a *n*-hexane/argon atmosphere for 4 hours at 500 °C. The gas mixture was prepared by bubbling argon through pure hexane at room temperature at a flow rate of  $58 \text{ cm}^3 \text{ min}^{-1}$ . A schematic drawing of the experimental set-up used in the hexane treatment is shown in Figure 3.1.

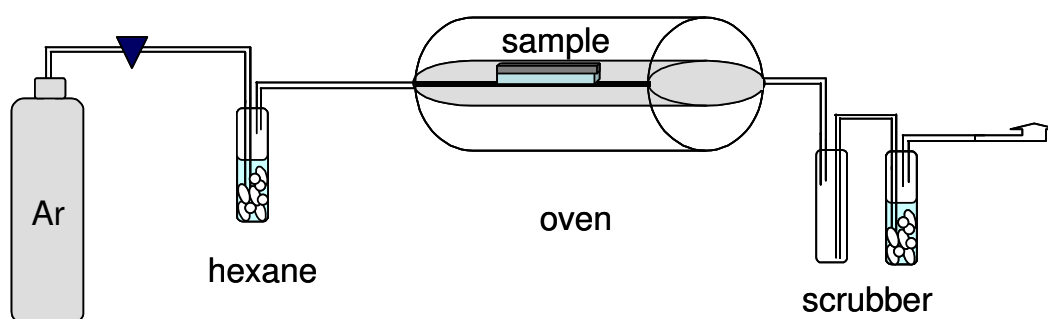


**Figure 3.1:** Schematic drawing of the experimental set-up used for hexane treatment and reduction of  $\text{TiO}_2$  samples under controlled atmosphere.

### 3.2.3 Characterization techniques

The morphology of doped and undoped TiO<sub>2</sub> films was characterized using a high-resolution scanning electron microscope equipped with a field emission gun (Philips XL-SFEG). Acceleration voltages between 5 and 30 kV were used for TiO<sub>2</sub> and TCO respectively.

Optical transmission and reflection spectra of the thin and mesoporous TiO<sub>2</sub> films were recorded using a Perkin-Elmer Lambda 900 spectrophotometer equipped with an integrating sphere (Labsphere).

X-ray diffraction (XRD) measurements were carried out using a Bruker D8 Advance diffractometer in grazing incidence mode, using Cu-K $\alpha$  radiation.

Photoelectrochemical experiments were performed using a three-electrode cell, with a quartz window, a platinum counter electrode, and a saturated calomel reference electrode (XR 300, Radiometer Analytical). A solution of 0.1M KOH (J.T. Baker) in demineralised and deionized water (Milli-Q, 18.2 M $\Omega$  cm) was used as the electrolyte. N<sub>2</sub> was bubbled through the solution to remove any dissolved oxygen. Electrical contacts were made by glueing copper wires to the conducting substrate with silver paint (Bison Electro). The working area of the electrodes was  $2.83 \times 10^{-5}$  m<sup>2</sup> ( $\phi$  6 mm) for all samples. Potential control was provided by an EG&G model 283 potentiostat. A 200 W tungsten halogen lamp in combination with a grating monochromator (Acton SPro 150) was used to irradiate the sample. High-pass filters (Schott) were used to remove the second order of the diffracted light. The light intensity was measured as a function of wavelength with a calibrated photodiode (PD 300-UV, Ophir).

## 3.3 Results and discussion

### 3.3.1 Film morphology

As-prepared all deposited thin dense films (TD) as well as mesoporous films (MP) are homogeneous, optically transparent and well adherent to the substrate. Figure 3.2 shows scanning electron microscopy (SEM) images of CO<sub>2</sub>-sprayed TiO<sub>2</sub> dense films. The films consist of near-spherical particles with an average diameter of ~160 nm. The TiO<sub>2</sub> film thickness is  $\sim 200 \pm 20$  nm. The surface morphology of the undoped TiO<sub>2</sub> films (not shown) is similar to that of the CO<sub>2</sub>-deposited films, i.e., no significant differences can be discerned.

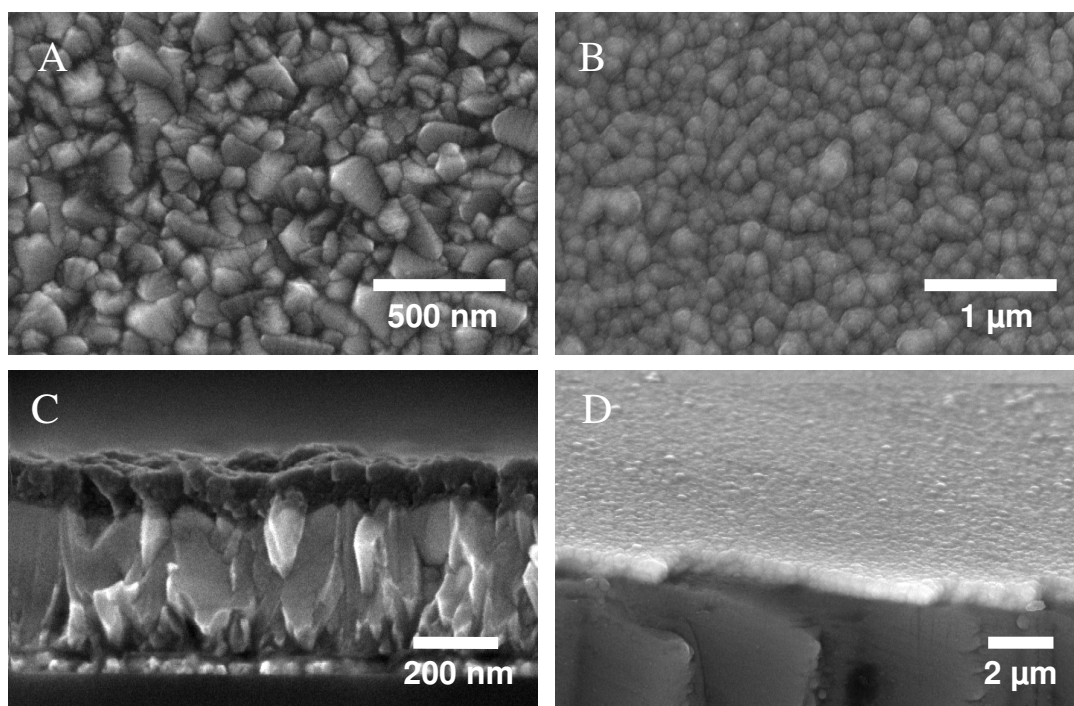


**Figure 3.2:** Scanning electron micrographs of A) the transparent conducting substrate (F:SnO<sub>2</sub>-coated glass); B-D) TiO<sub>2</sub> films sprayed under a CO<sub>2</sub>-containing atmosphere. Similar surface morphologies are obtained for TiO<sub>2</sub> films deposited in air, i.e., without CO<sub>2</sub>. In Figure 1C, the TiO<sub>2</sub> film (dark) can be clearly distinguished from the conducting substrate (light).

It is observed that after the hexane/argon treatment, the mesoporous TiO<sub>2</sub> films turn completely black (Figure 3.3C), while the thin dense TiO<sub>2</sub> films have only a slightly blackish appearance (Figure 3.3A).

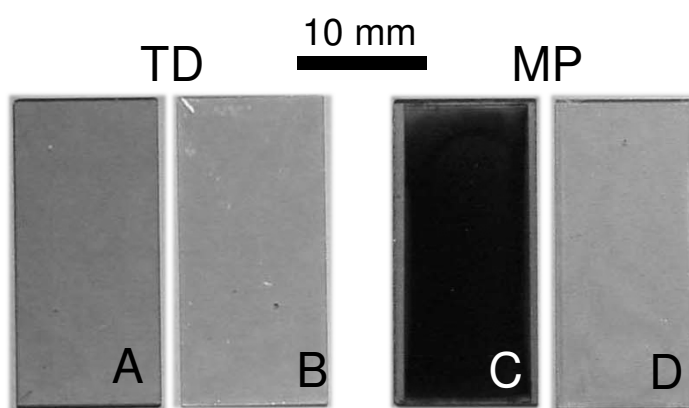
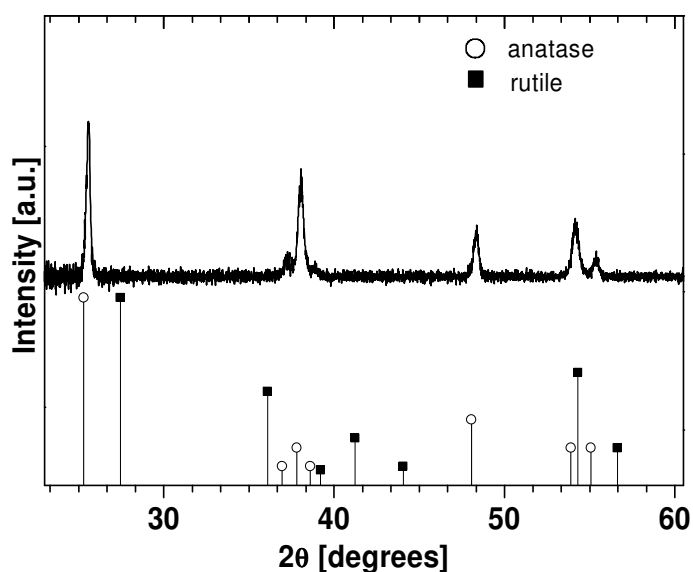


**Figure 3.3:** Photograph of thin dense (TD) and mesoporous (MP) TiO<sub>2</sub> films after the hexane/argon treatment at 500 °C for 4h (A, C), and after subsequent re-oxidation in air for 6h at 450 °C (B, D).

To study the stability of the hexane-treated films, they were re-oxidized in air for 6 hours at 450 °C. The black colour disappears completely after re-oxidation (see Figure 3.3B and D). Since no blackening is observed on bare quartz substrates after the hexane treatment, it appears that the hexane reacts with reactive sites at the TiO<sub>2</sub> surface.<sup>†</sup> The amount of material in the thin dense films (thickness ~200 nm) is about 3.5 times less than for the mesoporous films (~200 nm dense film + ~1 μm mesoporous film with a porosity of ~50%). The difference in the blackening of the TD vs. MP films in Figures 3.3A and 3.3C is, however, much larger than a factor of 3.5. From this, we conclude that the black colour of the mesoporous films is caused by the presence of carbon species at the surface of the TiO<sub>2</sub>, as opposed to a bulk doping effect.

### 3.3.2 Structure characterization

X-ray diffraction shows that the as-deposited films are crystalline with clear anatase peaks, as can be seen in Figure 3.4. The anatase structure is retained during the hexane-treatment and subsequent re-oxidation at elevated temperature, above 800 °C, as is discussed in more details in subchapter 3.3.5, Figures 3.7 and 3.8.



The results, corrected for reflections, are shown in Figure 3.5.<sup>‡</sup> The black colour of the hexane-treated mesoporous TiO<sub>2</sub> film corresponds to an overall increase of the absorption over the entire range of the measured spectrum (Figure 3.5E). After re-oxidation (Figure 3.5F), the absorption changes back to that of the untreated sample (Figure 3.5D), except for a small permanent shift of the absorption edge towards longer wavelengths. In the case of the thin dense films, the much smaller specific area results in a much smaller change in optical absorption upon hexane treatment (Figure 3.5B). Interestingly, these samples also show a small permanent shift after re-oxidation (Figure 3.5C vs. 3.5A). Assuming that all carbon at the surface is removed during re-oxidation, we attribute this small permanent shift to a small amount of carbon that diffuses into the bulk of the TiO<sub>2</sub> during the high-temperature hexane treatment.

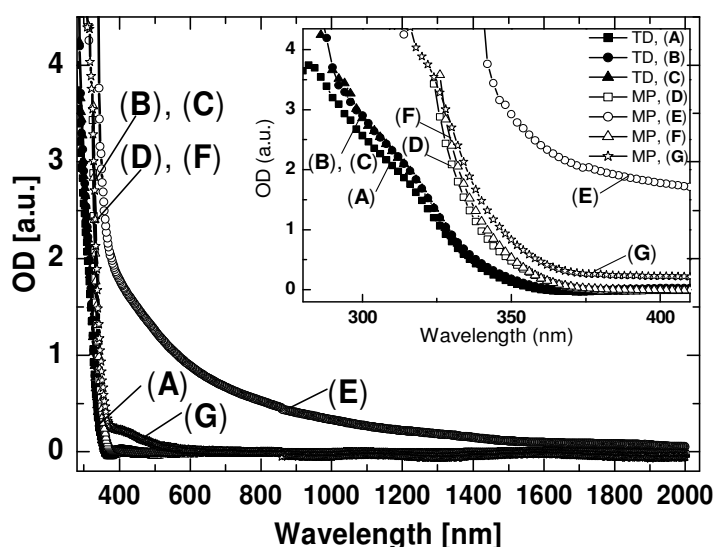


**Figure 3.5:** Optical absorption spectra for TD and MP TiO<sub>2</sub> films. (A, D) Undoped TiO<sub>2</sub>; (B, E) Annealed in hexane/argon at 500 °C for 4h; (C, F) Re-oxidized in air for 6h at 450 °C; (G) MP TiO<sub>2</sub> film reduced in an argon/hydrogen atmosphere at 500 °C for 4h.

Since the hexane treatment takes place under chemically reducing conditions, oxygen vacancies are formed. These are charge-compensated by electrons, which cause a dark coloring of the material. To investigate the extent of this contribution, a mesoporous TiO<sub>2</sub> film was reduced in a carbon-free atmosphere consisting of argon +1% hydrogen at 500 °C. As shown in Figure 3.5G, this results in a relatively small increase of the optical density (OD) between 400 and 500 nm, and the sample appears slightly brownish. Clearly, oxygen vacancies cannot be held responsible for the black colour observed after the hexane treatment. After re-oxidation, the original spectrum (Figure 3.5D) is fully recovered, which supports our conclusion that carbon is either directly or indirectly responsible for the small permanent shift of the absorption edge after the hexane treatment.

<sup>‡</sup> The optical densities (absorption spectra) of the films were corrected for reflection and are calculated using:  $OD = -\log_{10}(T/(1-R))$ , where *R* and *T* are the fractions of reflected and transmitted light, respectively.

### 3.3.4 Photoelectrochemical properties

To determine, if the observed changes in the optical absorption also result in changes in the photoelectrochemical activity, incident photon-to-current conversion efficiencies (IPCE) have been measured (Figure 3.6).<sup>§</sup> It should be noted that the hexane-treated films require a minimum re-oxidation time of 30 minutes before any photocurrent could be measured. Presumably, the carbonaceous species deposited on the TiO<sub>2</sub> surface prevent electron transfer across the semiconductor/electrolyte interface. The differences in the magnitudes of the IPCE responses of the mesoporous TiO<sub>2</sub> films are attributed to variations in the actual exposed surface area of these highly porous films.

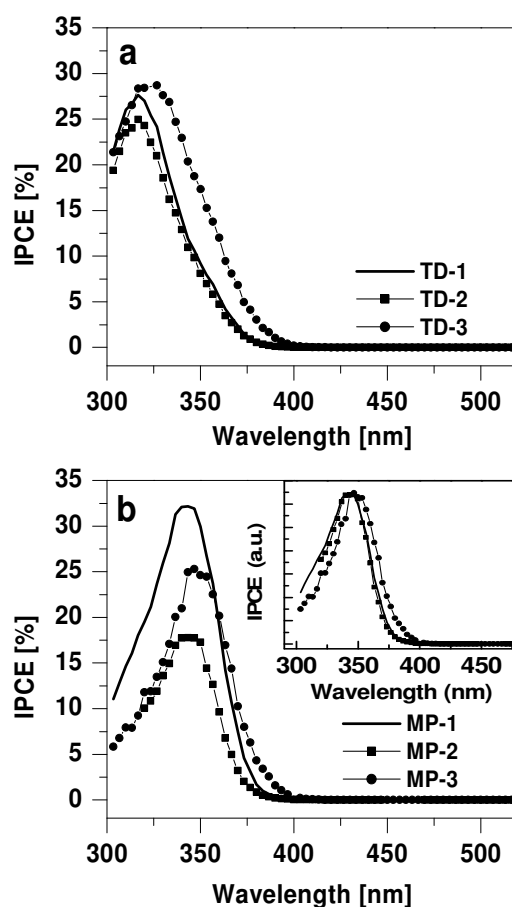


**Figure 3.6:** (a and b) Photocurrent action spectra of TD and MP TiO<sub>2</sub> films. TD-1, MP-1: before hexane treatment; TD-2, MP-2: reduced in argon/hydrogen at 500 °C for 4h and re-oxidized in air for 1h at 450 °C; TD-3, MP-3: treated in hexane at 500 °C for 4h and re-oxidized in air for 1h at 450 °C. The spectra were obtained using an aqueous 1.0 M KOH solution, at a potential of +0.5V vs. SCE. The insert shows the normalized IPCE of MP TiO<sub>2</sub>.

<sup>§</sup> The IPCE was calculated according to:  $IPCE = (hc \cdot I_{ph}) / (e \cdot P \cdot \lambda)$ , where  $I_{ph}$  is the photocurrent in Amperes,  $P$  is the power intensity of the light in Watts,  $\lambda$  is the wavelength in meters, and all other symbols have their usual meanings.

To compare the shape of the spectra, normalized IPCE values are plotted in the insert of Figure 3.6b. A small, but distinct permanent shift ( $\sim 0.1$  eV) of the absorption response edge towards the visible part of the spectrum is observed for both thin dense and mesoporous hexane-treated TiO<sub>2</sub> films after re-oxidation. Straightforward reduction of TiO<sub>2</sub> in an argon/hydrogen atmosphere followed by re-oxidation does not result in any shift of the absorption edge (see Figure 3.6, TD-3 and MP-3). Hence, the photoelectrochemical results indeed correspond to the optical absorption data.

The red-shift of the photocurrent is consistent with the theoretical calculations by Asahi et al. [14] for carbon-doped anatase TiO<sub>2</sub>, which showed an enhanced density-of-states (DOS) just above the valence band edge. However, the measured shift in our samples ( $\sim 0.05$ - $0.1$  eV) is significantly smaller than that predicted by Asahi et al. ( $\sim 0.3$ - $1.2$  eV). A possible explanation for this is the difference in carbon concentration; the calculated DOS is based on 1 carbon per 8 TiO<sub>2</sub> units, whereas the carbon concentration in our films is estimated to be much lower. Specifically, from the absence of any visible-light photoresponse ( $> 400$  nm), the carbon content in the bulk of our hexane-treated films is estimated to be below 0.1 at%. This upper limit estimation is based on a comparison of our optical absorption spectra with the diffuse reflectance spectra reported by Sakhivel *et al.* for carbon-modified TiO<sub>2</sub> powders with known carbon concentration [8]. In general, a reliable quantitative measurement of such low amounts of carbon is rather difficult, since the total amount of material in our thin-film samples is small. Furthermore, the sensitivity of most analytical techniques based on ion- or electron-scattering is generally poor for light elements such as carbon.

### **3.3.5 Phase transformation investigation**

An indirect method to determine the presence of small amounts of dopant ions is by examining its effect on the phase transformation characteristics. The presence of carbon has been reported to suppress the anatase-to-rutile phase transformation [24,25], whereas cation dopants seem to favour the transformation to rutile [1]. Figure 3.7 shows the X-ray diffraction spectra of undoped and hexane-treated TiO<sub>2</sub> after thermal treatments at increasingly higher temperatures. At 850 °C, the relative amount of rutile in hexane-treated TiO<sub>2</sub> is less than that for undoped TiO<sub>2</sub>, which is indeed consistent with the assumption that a small amount of carbon is present in the bulk of the material. A similar series of measurements was carried out on carbon-doped TiO<sub>2</sub> samples made by spraying under a CO<sub>2</sub> atmosphere [28], see Figure 3.8. (More details on these films are presented in Chapter 2). Here, the transformation to rutile is much more strongly suppressed, and no traces of rutile are found even after annealing at 950 °C. This suggests that the amount of carbon in the bulk of these samples is higher than that of the hexane-treated samples, which is indeed a reasonable assumption since the CO<sub>2</sub>-sprayed samples were exposed to a carbon-containing environment during growth. It should be noted, however, that the different thicknesses of the CO<sub>2</sub>-sprayed samples and the hexane-treated samples might also have affected the phase transformation kinetics to some extent.

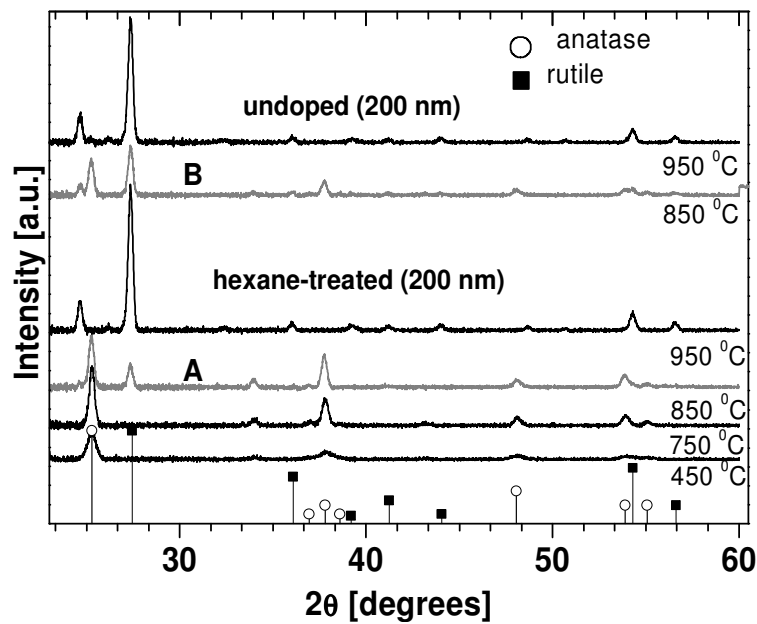


**Figure 3.7:** XRD spectra of undoped and hexane-treated TiO<sub>2</sub> films on quartz, after baseline correction. The undoped TiO<sub>2</sub> sample was annealed in air for 6h. The hexane-treated TiO<sub>2</sub> was annealed in hexane/argon at 500 °C for 4h and successively re-oxidized in air between 450 °C and 950 °C. The annealing time was 6 hours at each temperature. Spectra are vertically offset for clarity.

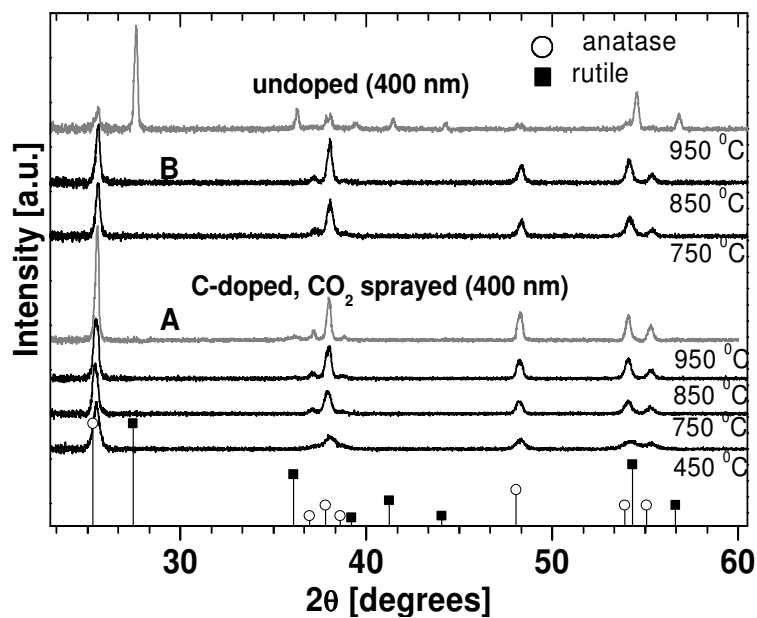


**Figure 3.8:** XRD spectra of undoped and CO<sub>2</sub>-sprayed TiO<sub>2</sub> films on quartz, after baseline correction. The undoped TiO<sub>2</sub> sample was annealed in air for 6h. The CO<sub>2</sub>-sprayed TiO<sub>2</sub> was deposited under a CO<sub>2</sub> atmosphere [28] and successively oxidized in air between 450 °C and 950 °C. The annealing time was 6 hours at each temperature. Spectra are vertically offset for clarity.

### 3.4 Conclusions

Good quality undoped and C-doped TiO<sub>2</sub> anatase films have been obtained by spray pyrolysis. Also good quality homogeneous nanoporous films have been prepared by doctor blading. It has been shown that carbon, introduced into anatase TiO<sub>2</sub> by a post-deposition thermal treatment in a hexane-containing environment, is mainly located at the surface of the TiO<sub>2</sub>. These surface species are responsible for the black colouring of the nanocrystalline nanoporous TiO<sub>2</sub> film and do not lead to enhanced photocatalytic activities in the visible part of the spectrum. A small fraction of the carbon is located in the bulk of the material, where it causes a small shift (~0.05-0.1 eV) of the absorption edge towards the visible part of the spectrum. Furthermore, the presence of the carbon in anatase TiO<sub>2</sub> increases the anatase-to-rutile transformation temperature. From the amount by which the phase transformation temperature increases, it is found that TiO<sub>2</sub> samples sprayed under a CO<sub>2</sub> atmosphere contain significantly more carbon than samples subjected to a high-temperature post-deposition hexane treatment. In both cases, however, the amount of carbon incorporated into the anatase TiO<sub>2</sub> is not sufficient to generate a visible-light photoresponse. To sensitize anatase TiO<sub>2</sub> to visible light, other methods, such as the oxidative annealing of TiC [9,10] seem more suited.

### References

- [1]. A. R. Bally, E. N. Korobeinikova, P. E. Schimid, F. Lévy, and F. Bussy, *J. Phys. D: Appl. Phys.* **31** (1998) 1149.
- [2]. C. Y. Wang, C. Bottcher, D. W. Bahnemann, and J. K. Dohrmann, *J. Mater. Chem.* **13** (2003) 2322.
- [3]. E. Borgarello, J. Kiwi, G. Michael, E. Pellizzetti, and M. Viscald, *J. Am. Chem. Soc.* **104** (1982) 2996.
- [4]. A. K. Ghosh and H. P. Maruska, *J. Electrochem. Soc.* **124** (1977) 1516.
- [5]. Z. Luo and Q. H. Gao, *J. Photochem. Photobiol. A* **63** (1992) 367.
- [6]. W. Choi, A. Termin, and M.R. Hoffmann, *J. Phys. Chem.* **98** (1994) 13669.
- [7]. S. U. M. Khan, M. Al Shahry, and W. B. Ingler, Jr., *Science* **297** (2002) 2243.
- [8]. S. Sakthivel and H. Kisch, *Angew. Chem. Int. Ed.* **42** (2003) 4908.
- [9]. Y. Choi, T. Umebayashi, and M. Yoshikawa, *J. Mater. Sci.* **39** (2004) 1837.
- [10]. H. Irie, Y. Watanabe, and K. Hashimoto, *Chem. Lett.* **32** (2003) 772.
- [11]. C. Lettmann, K. Hildenbrand, H. Kisch, W. Macyk, and W. F. Maier, *Appl. Catal. B: Environ.* **32** (2001) 215.
- [12]. R. Asahi, T. Morikawa, T. Ohwaki, K. Aoki, and Y. Taga, *Science* **293** (2001) 269.
- [13]. G. R. Torres, T. Lindgren, J. Lu, C. G. Granqvist, and S. E. Lindquist, *J. Phys. Chem. B* **108** (2004) 5995.
- [14]. T. Lindgren, J. M. Mwabora, E. Avendano, J. Jonsson, A. Hoel, C. G. Granqvist, and S. E. Lindquist, *J. Phys. Chem. B* **107** (2003) 5709.
- [15]. C. Burda, Y. B. Lou, X. B. Chen, A. C. S. Samia, J. Stout, and J. L. Gole, *Nano Lett.* **3** (2003) 1049.
- [16]. T. Morikawa, R. Asahi, T. Ohwaki, K. Aoki, and Y. Taga, *Jpn. J. Appl. Phys.* **2**, (40) (2001) L561.
- [17]. S. Sakthivel, M. Janczarek, and H. Kisch, *J. Phys. Chem. B* **108** (2004) 19384.
- [18]. H. Irie, Y. Watanabe, and K. Hashimoto, *J. Phys. Chem. B* **107** (2003) 5483.
- [19]. R. Nakamura, T. Tanaka, and Y. Nakato, *J. Phys. Chem. B* **108** (2004) 10617.
- [20]. S. M. Prokes, J. L. Gole, X. Chen, C. Burda, and W. E. Carlos, *Adv. Funct. Mater.* **15** (2005) 161.
- [21]. T. Umebayashi, T. Yamaki, H. Itoh, and K. Asai, *Appl. Phys. Lett.* **81** (2002) 454.
- [22]. T. Ohno, M. Akiyoshi, T. Umebayashi, K. Asai, T. Mitsui, and M. Matsumura, *Appl. Catal. A: Gen* **265** (2004) 115.

- [23]. T. Tachikawa, S. Tojo, K. Kawai, M. Endo, M. Fujitsuka, T. Ohno, K. Nishijima, Z. Miyamoto, and T. Majima, *J. Phys. Chem. B* **108** (2004) 19299.
- [24]. B. Tryba, A. W. Morawski, and M. Inagaki, *Appl. Catal. B: Environ.* **46** (2003) 203.
- [25]. M. Janus, B. Tryba, M. Inagaki, and A. W. Morawski, *Appl. Catal. B: Environ.* **52** (2004) 61.
- [26]. B. Tryba, T. Tsumura, M. Janus, A. W. Morawski, and M. Inagaki, *Appl. Catal. B: Environ.* **50** (2004) 177.
- [27]. K. Noworyta and J. Augustynski, *Electrochem. Solid St.* **7** (2004) E31.
- [28]. C. S. Enache, J. Schoonman, and R. Van de Krol, *J. Electroceram.* **13** (2004) 177.
- [29]. L. Kavan and M. Gratzel, *Electrochim. Acta* **40** (1995) 643.

# Chapter 4

## Photoelectrochemical properties of thin film $\text{InVO}_4$ photoanodes: the role of deep donor states<sup>\*</sup>

### Abstract

*The material properties and photoelectrochemical performance of compact thin film  $\text{InVO}_4$  photoanodes prepared by spray pyrolysis are investigated. Nearly phase-pure orthorhombic  $\text{InVO}_4$  can be obtained by a postdeposition annealing in air between 450-550 °C. Optical absorption spectra indicate that  $\text{InVO}_4$  has an indirect bandgap of ~3.2 eV with a pronounced sub-bandgap absorption starting at ~2.5 eV. A dielectric constant of 50 and a flatband potential of -0.04 V vs. RHE are determined, which confirms that this material is able to evolve hydrogen. Few shallow donors are present in this material, which is markedly different from what is usually observed for simple binary oxides. The main photocurrent response occurs in the UV (<400 nm) and the incident photon-to-current conversion efficiency is less than 1%. The impedance data show that the poor photoresponse is due to a high density of deep donors and a concomitantly small depletion layer. The visible light absorption of  $\text{InVO}_4$  is attributed to the presence of ionized deep donors in the space charge region of the material, which explains why  $\text{InVO}_4$  powders show a much stronger visible light absorption than thin films. The defect-chemical origin of the deep donor states is discussed and some general considerations for the use of ternary and more complex metal oxides as photoelectrodes are outlined.*

---

<sup>\*</sup> This chapter is based on: Cristina S. Enache, David Lloyd, Martijn R. Damen, Joop Schoonman, and Roel van de Krol, *J. Phys. Chem. C*, **113** (2009), 19351-19360

## 4.1 Introduction

Amidst growing environmental concerns, solar water splitting for clean, renewable production of hydrogen is an appealing prospect. Compared to coupled photovoltaic - electrolysis systems, direct photoelectrolysis with semiconducting photoelectrodes offers the benefit of achieving (in principle) higher efficiencies and lower system costs [1]. While current state-of-the-art systems based on sophisticated multijunction devices combine solar-to-hydrogen (STH) efficiencies of up to 18% with excellent stability against photocorrosion [2], they are too expensive for large-scale terrestrial application [3]. Low-cost transition metal oxides may represent an attractive alternative. Recent breakthroughs in the synthesis of nanostructured electrodes show that STH efficiencies of 2.2% (for  $\alpha\text{-Fe}_2\text{O}_3$ ) and 3.6% (for  $\text{WO}_3$ ) are now within reach when using a tandem cell configuration [4,5].

Despite these advances, no metal oxide has yet been found that combines the three main requirements for water splitting, i.e., good visible light absorption, high photochemical stability, and suitable band energetics so that no additional bias voltage is required. After more than three decades of intensive research on many different undoped and doped oxides, one may tentatively conclude that i) no binary oxide can split water with appreciable efficiencies unless a tandem cell approach is used, and ii) doping wide-bandgap oxides to enhance the visible-light response does not result in higher overall efficiencies. The latter is due to the concomitant increase in recombination when optically active deep donors or acceptors are introduced.

In view of these considerations, many efforts are now geared towards ternary and even more complex metal oxides. While these efforts can be traced back to the 1970s [6], it was the 2001 paper by Zou et al. on Ni-doped  $\text{InTaO}_4$ , which appears to have re-started the more recent interest in these systems [7]. Since then, significant progress has been made and several promising materials have been identified [8]. Examples include  $\text{In}_{1-x}\text{Ni}_x\text{TaO}_4$  [7],  $\text{BaIn}_{0.5}\text{Nb}_{0.5}\text{O}_3$  [9],  $\text{InVO}_4$  [10], and  $\text{BiVO}_4$  [11]. Continued research efforts are motivated by the numerous possible compositions and the fact that only a handful of these have been studied as water splitting photocatalysts. This has even prompted the development of combinatorial studies in photoelectrochemistry [12,13].

It should be noted, however, that most of the reports on complex oxide photocatalysts are on powders. While these have the advantage of being fairly easy to prepare using high-temperature solid state reactions, there are several drawbacks. One is that hydrogen and oxygen are generally produced in the same volume, leading to safety concerns and the need for an additional (energy-consuming) separation step. There are also inherent difficulties in comparing the activity and conversion efficiency of suspension-based systems (usually reported in  $\mu\text{mole}\cdot\text{g}^{-1}\cdot\text{h}^{-1}$ ) with those of photoelectrodes (in  $\text{mA}/\text{cm}^2$ ). Direct comparison of the turnover-frequency at a single surface site appears to favor photoelectrode-based systems [14], although these results show an admittedly strong dependence on extrinsic factors such as particle size and reactor geometry. From a research point of view, however, the single most important difficulty with powder-based systems is that the rate-limiting processes and materials properties are difficult to identify. While some insight can be gained by adding electron or hole scavenging species to the solution, the investigative tools for photoelectrodes (front- vs. back-side illumination, photocurrent transients, and impedance spectroscopy) are far more extensive.

In this paper, we explore the properties of InVO<sub>4</sub> photoelectrodes. As shown by Ye et al. in their work on InVO<sub>4</sub> powders, it is one of the few oxides that shows hydrogen evolution from pure water under visible light illumination [10]. This clearly indicates that the conduction band minimum is more negative than the hydrogen evolution potential, one of the key requirements for unassisted water splitting. Porous InVO<sub>4</sub> electrodes also show a visible-light photoresponse, although the photocurrents are relatively low [15]. Despite several other reports on this material [16-18], very little is known about the intrinsic material properties and the factors that limit its photocatalytic and/or photoelectrochemical performance. We will show that it is possible to make thin, compact films of (nearly) phase-pure orthorhombic InVO<sub>4</sub> at low temperatures (<600 °C) by using spray pyrolysis. The fact that these films are nonporous allows us to determine some of its key optical and electrical properties. Based on these results, the performance-limiting factors for InVO<sub>4</sub> will be identified and some important general considerations for the design of photoelectrodes based on complex oxides will be discussed.

## **4.2 Experimental details**

Undoped, Ni-doped, and Cu-doped InVO<sub>4</sub> thin films were prepared by spray pyrolysis of an ethanolic precursor solution onto a heated substrate in air. The precursor solution consisted of In(NO<sub>3</sub>)<sub>3</sub> (99.99%, Alfa Aesar) and VCl<sub>3</sub> (99%, Alfa Aesar) dissolved in ethanol (>99.9%, J.T. Baker). After the metal salts were dissolved in ethanol, the nitrate groups from the indium precursor rapidly oxidize the V<sup>3+</sup> ions (green) to V<sup>4+</sup> (purple), followed by a much slower overnight oxidation to V<sup>5+</sup> (yellow) [19]. This solution is stable for several months after preparation. The total concentration was 0.2 M and an In/V ratio of 1:1 was used. Nitrogen was used as a carrier gas, and the substrate temperature was 400 °C (measured by pressing a small thermocouple to the sample surface). A 5 s on, 120 s off, spraying-cycle was used to allow the solvent to evaporate before depositing the next layer. The films were deposited onto 1 mm thick fused silica (quartz) substrates (Heraeus, Suprasil 1) for optical characterization and on transparent conducting glass (FTO, 15 Ω cm<sup>-2</sup> F:SnO<sub>2</sub>, TEC-15, Libbey Owens-Ford) or on Pt- or Au-coated quartz for photoelectrochemical studies.

All films were subjected to a post-deposition thermal anneal at 450 °C or 550 °C in air for 6 hours in order to further improve the stoichiometry and crystallinity. Several films deposited on quartz were subjected to additional heat treatments up to 800 °C.

X-ray diffraction (XRD) measurements were carried out with a Bruker D8 Advance diffractometer in grazing incidence mode, using Cu-Kα radiation. The Raman spectra were recorded with a home-built setup using a continuous-wave Nd:YVO<sub>4</sub> laser, with a wavelength of 532 nm (Millennia, Spectra Physics). The back-scattered light was recorded by a CCD camera cooled with liquid nitrogen (model LN/CCD-1100PB, Princeton Instruments), via a monochromator (model 340E, Spex) with an 1800 grooves/mm grating. The 532 nm laser line was removed with a Supernotch filter (Kaiser Optical Systems).

Optical transmission and reflection spectra of the thin InVO<sub>4</sub> films were recorded using a Perkin-Elmer Lambda 900 spectrophotometer equipped with an integrating sphere (Labsphere). The morphology of the films was characterized using a high-resolution scanning

electron microscope equipped with a field emission gun (Philips XL-SFEG). Atomic Force Microscopy (AFM) data were obtained with a Veeco DI EnviroScope, using a tip diameter of 10 nm and a scanning rate of 0.8 Hz (256×256 pixels).

Photoelectrochemical experiments were performed using a conventional three-electrode cell with a quartz window, a platinum counter electrode, a platinum quasi-reference electrode, and an Ag/AgCl reference electrode (3 M KCl, REF 321, Radiometer Analytical). A solution of 0.1 M KOH (J.T. Baker) in demineralized and deionized water (Milli-Q, 18.2 MΩ cm) was used as the electrolyte. Nitrogen gas was bubbled through the solution to remove any dissolved oxygen. Electrical contacts between InVO<sub>4</sub>/FTO were made by connecting copper wires to the conducting substrate with silver paint (Bison Electro). The contact was covered with an epoxy resin to improve mechanical stability. The working area of the electrodes exposed to the electrolyte was  $2.83 \times 10^{-5} \text{ m}^2$  (6 mm diameter) for all samples. Potential control was provided by an EG&G model 283 potentiostat. For impedance analysis a Solartron model 1255 Frequency Response Analyzer was connected to the potentiostat. The measurements were performed using a perturbation amplitude of 10 mV at different potentials.

A 200 W tungsten halogen lamp in combination with a grating monochromator (Acton SPro 150) was used to irradiate the sample. High-pass filters (Schott) were used to remove the second order of the diffracted light. Photocurrent voltammograms were recorded using a 375 nm LED (Roithner, type LED375-06,  $p_{\text{max}}=2.5 \text{ mW}$ ) as a monochromatic light source. The light intensity was measured as a function of wavelength with a calibrated photodiode (PD 300-UV, Ophir). Photocurrent action spectra were recorded using a lock-in amplifier (EG&G PAR model 5210) connected to the potentiostat.

## 4.3 Results and discussion

### 4.3.1 Film morphology

Figure 4.1 shows a photograph of two InVO<sub>4</sub> films with different thicknesses on F:SnO<sub>2</sub> coated glass (FTO), compared to an uncoated FTO substrate. All InVO<sub>4</sub> thin films have a yellow-brownish color, are homogeneous, and crack-free. The films show good adherence to the substrate and cannot be easily removed by mechanical scratching. Scanning electron microscopy (SEM) reveals that the films consist of small irregular crystallites with sizes ranging from 50-200 nm (Figure 4.2A). After an additional annealing at 550 °C in air, the crystallites take on a more defined shape (Figure 4.2B). The morphology of the films does not visibly change when nickel or copper are incorporated as dopants. From a cross-section of the film, presented in Figure 4.2C, the InVO<sub>4</sub> film (dark) can be clearly distinguished from the conducting substrate (light). As can be observed in Figures 4.2C-E, the roughness of the deposited films is comparable to that of the underlying F:SnO<sub>2</sub> film. The InVO<sub>4</sub> film thickness is determined to be  $100 \pm 20 \text{ nm}$  (for 40 spray cycles), the thickness of the F:SnO<sub>2</sub> film (Figures 4.2E-F) is about 400 nm.

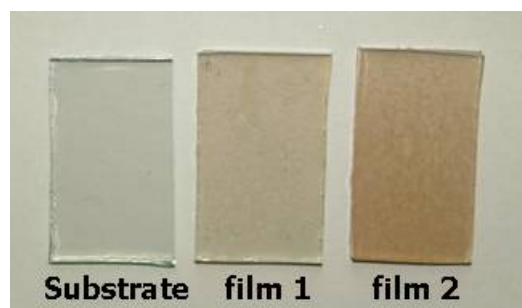


**Figure 4.1:** Photograph of sprayed  $\text{InVO}_4$  thin films with different thicknesses compared to a blank substrate ( $\text{F}:\text{SnO}_2$  on glass). Film 2 is two times thicker than film 1.

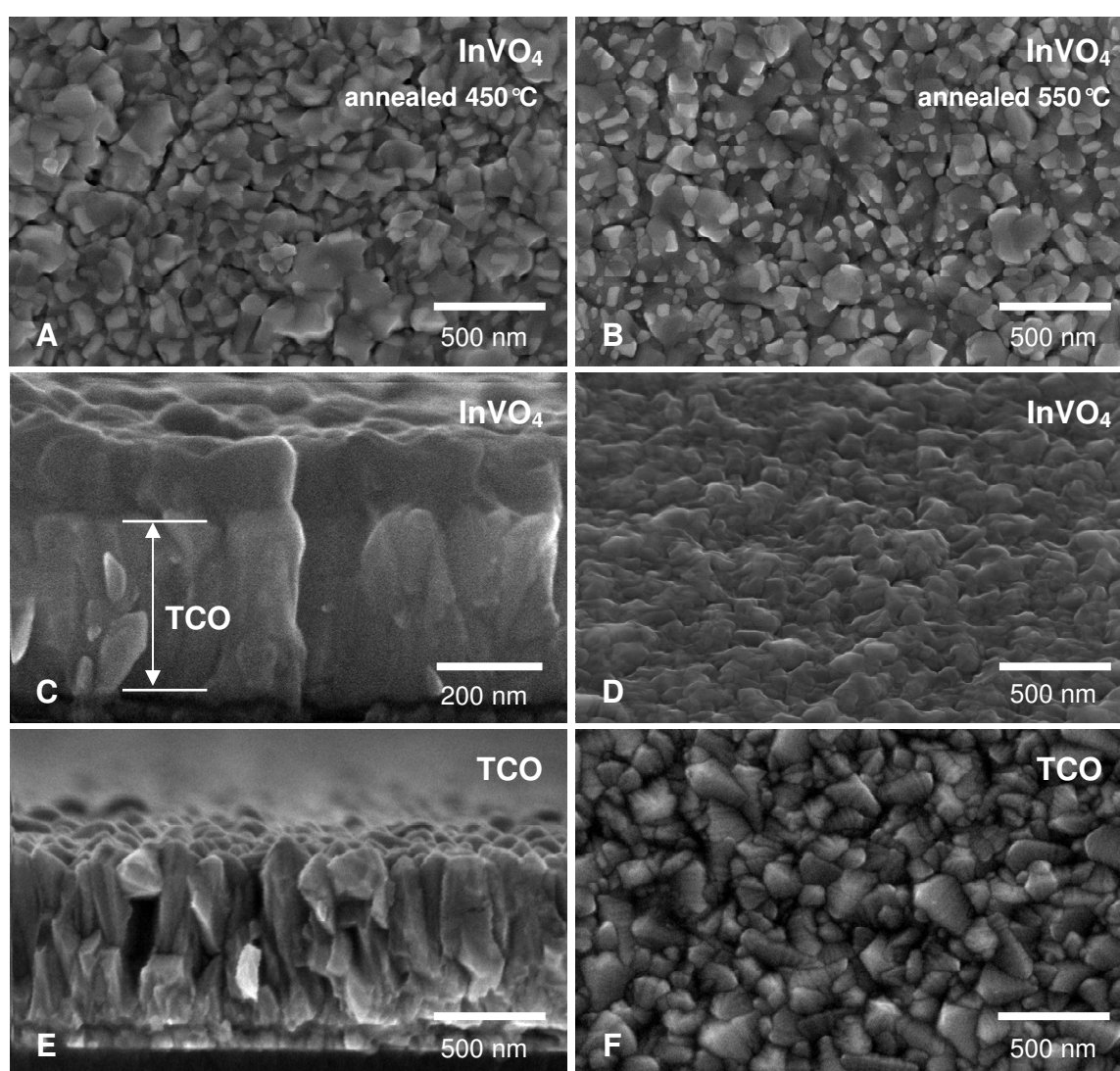
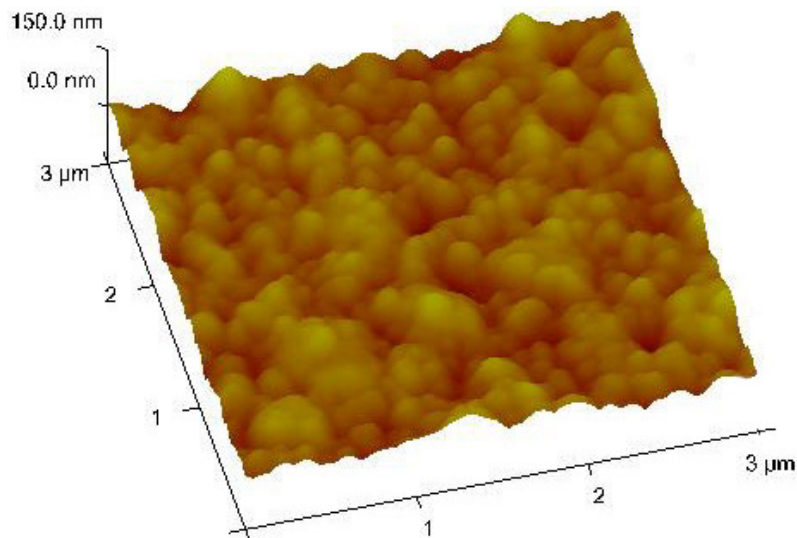
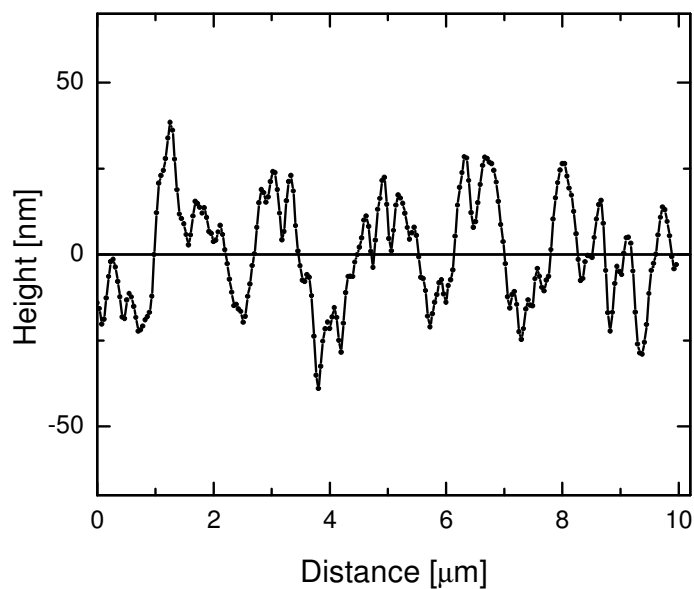


**Figure 4.2:** Scanning electron micrographs of  $\text{InVO}_4$  deposited on conductive glass (A-D), compared to uncoated substrates (E-F). Although the morphology of the  $\text{InVO}_4$  films can be clearly distinguished from that of the underlying  $\text{F}:\text{SnO}_2$  substrate, the typical feature size is about the same.

Figure 4.3A shows a 3D atomic force microscope (AFM) image of the  $\text{InVO}_4$  films deposited on FTO. Analysis shows that the roughness of the  $\text{InVO}_4$  film is comparable to that of the FTO substrate, in agreement with the SEM results. An average (rms) roughness of 15 nm is found, with a peak-to-peak roughness of about 50 nm (Figure 4.3B).



A)



B)

**Figure 4.3:** A) AFM image of a spray-deposited  $\text{InVO}_4$  film deposited on F:SnO<sub>2</sub>. B) line scan showing a peak-to-peak roughness of 50 nm and a root-mean-square (rms) roughness of about 15 nm.

### 4.3.2 Structure characterization

For  $\text{InVO}_4$  samples deposited on bare quartz, X-ray diffraction reveals a mixture of the monoclinic and orthorhombic  $\text{InVO}_4$  phases (Figure 4.4). The monoclinic  $\text{InVO}_4$ -I phase (JCPDS 38-1135) dominates in as-deposited films and no significant structural changes are observed after a post-deposition anneal treatment at 450 °C. However, after an additional anneal treatment at 550 °C in air for 6 hours, the monoclinic peaks at 13.0, 26.1 and 39.6 degrees 2-theta disappear completely and new orthorhombic peaks at 22.9, 32.9 and 35.1 degrees 2-theta appear (Figure 4.4, bottom curve). This indicates an almost complete transformation into the orthorhombic  $\text{InVO}_4$ -III phase (JCPDS 33-0628). Only a very small monoclinic peak at 16.7 degrees persists, even after subsequent annealing at 800 °C, indicating that trace amounts of monoclinic  $\text{InVO}_4$  may remain present.

In contrast,  $\text{InVO}_4$  films sprayed on FTO or platinum- or gold-coated quartz already show the orthorhombic crystal structure after deposition, i.e., without a post-deposition thermal anneal. The X-ray diffraction patterns for these films are almost identical to the lower curve in Figure 4.4. A post-deposition anneal treatment in air at 450 or 550 °C for 6 hours improves the crystallinity somewhat, but does not lead to significant changes in the XRD pattern. Again, a small peak at 16.7 degrees is observed, indicating that trace amounts of the monoclinic phase may still be present.

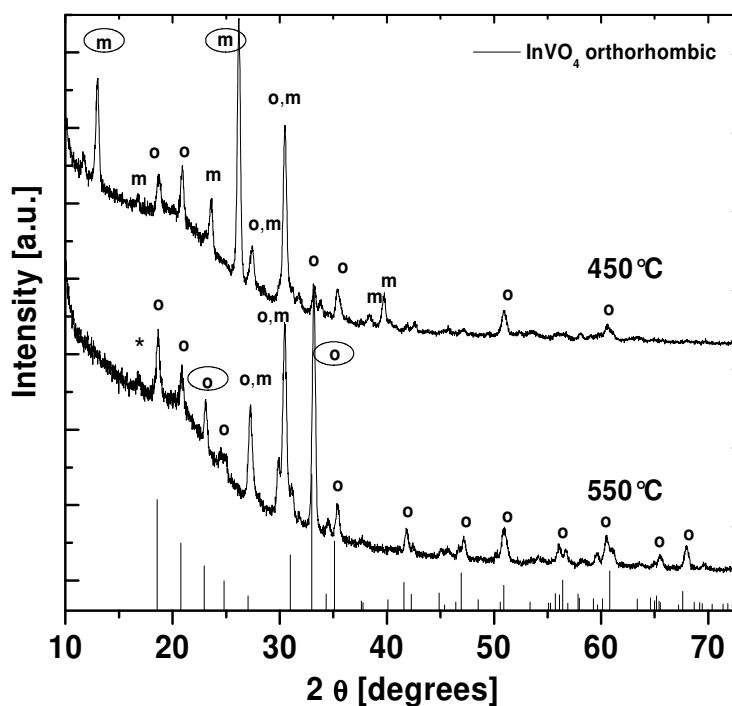


**Figure 4.4:** Grazing Incidence XRD measurements on undoped  $\text{InVO}_4$  on quartz annealed in air at 450 °C and 550 °C. At 450 °C the monoclinic phase (m) dominates, which is almost fully converted to the orthorhombic phase (o) at 550 °C. The vertical lines represent the powder diffraction pattern of orthorhombic  $\text{InVO}_4$ -III (JCPDS 33-0628).

The XRD results are confirmed by the Raman spectrum shown in Figure 4.5. The peaks at 217, 342, 404, 456, 640, 755, and, 915  $\text{cm}^{-1}$  correspond to the orthorhombic  $\text{InVO}_4$ -III phase [15,20], whereas the origin of the peak at 881  $\text{cm}^{-1}$  is not clear. None of the related binary oxides, such as  $\text{V}_2\text{O}_5$ ,  $\text{V}_2\text{O}_3$ , or  $\text{In}_2\text{O}_3$ , has a peak at this position [21-25].

These results show that it is possible to deposit thin, dense orthorhombic  $\text{InVO}_4$  films at relatively low temperatures (450 °C) using spray pyrolysis. This temperature is significantly lower than the temperature of 680 °C required to convert  $\text{InVO}_4$  powders to the orthorhombic phase, as reported by Touboul et al. [26,27]. Raman spectroscopy and X-ray diffraction show no traces of binary oxides. The main difficulty is to obtain a 100% orthorhombic crystal structure, as minor traces of the monoclinic phase remain present even after annealing at 800 °C. A recent publication by Zang et al. shows that it is possible to obtain phase-pure orthorhombic  $\text{InVO}_4$  films by pyrolysing an amorphous complex precursor at 500 °C [15]. However, it should be noted that these films are highly porous, in contrast to our dense films.

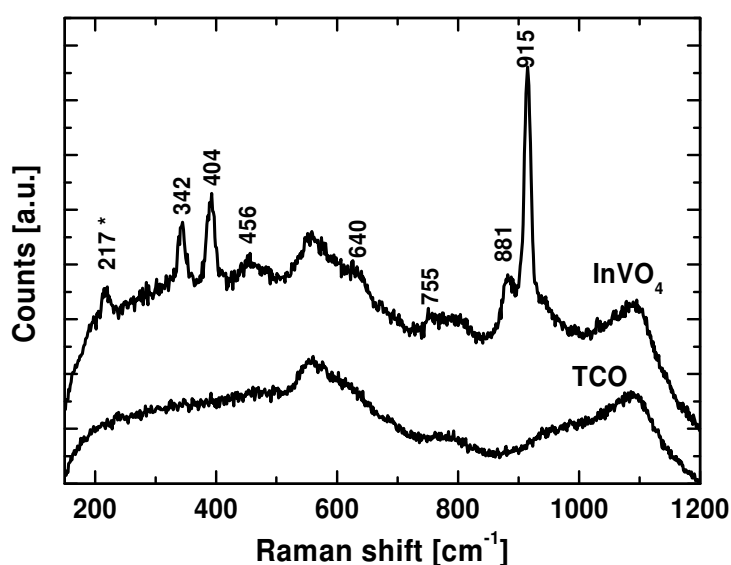


**Figure 4.5:** Raman spectrum of an undoped  $\text{InVO}_4$  film deposited on a conductive glass substrate (FTO) compared to that of an uncoated substrate.

### 4.3.3 Optical and photoelectrochemical characterization

Figure 4.6 shows the optical density spectra of  $\text{InVO}_4$  films deposited on quartz, after annealing at 450 °C and 550 °C. The optical density is calculated from the transmission and reflection data according to  $OD = -\text{Log}(T/(1-R))$ . The transmission ( $T$ ) and reflection ( $R$ ) fringes cancel each other almost perfectly and the absorption ( $A$ ) measured by placing the sample in the integrating sphere never deviates more than a few percent from  $(1-T-R)$  over the entire wavelength range. As discussed in the preceding section, the films annealed at 450 °C contain mainly monoclinic  $\text{InVO}_4$ , whereas the films treated at 550 °C are almost fully converted to the orthorhombic phase. With this in mind, the data in Figure 4.6 show that the optical absorption characteristics of monoclinic and orthorhombic  $\text{InVO}_4$  are very similar.

The main absorption feature starts at around 450 nm ( $\sim 2.8$  eV). When plotting  $(\text{OD} \times \text{h}\nu)^{1/2}$  vs.  $\text{h}\nu$  (insert Figure 4.6), two linear regimes are observed. Extrapolation of the data between  $\sim 3.7$  and  $\sim 4.2$  eV yields an indirect bandgap of  $2.5 \pm 0.2$  eV. A plot of  $(\text{OD} \times \text{h}\nu)^2$  vs.  $\text{h}\nu$  does not show a linear regime, which confirms that the bandgap of this semiconductor is indeed indirect. Figure 4.6 also shows a second linear regime between 2.5 and 3.7 eV, with an onset absorption at  $2.5 \pm 0.02$  eV. Since this absorption is rather weak, it is unlikely to be caused by a band-to-band transition. Instead, an alternative explanation based on optical transitions from or to defect levels in the bandgap seems more appropriate.

It should be noted that  $\text{InVO}_4$  powders show similar absorption features, but with a much stronger response in the visible part of the spectrum ( $>400$  nm). Ye et al. interpreted the visible light response as a transition from the valence band to the conduction band, and reported a bandgap of 1.9-2.0 eV for  $\text{InVO}_4$  [10,18]. However, the modest variation of the absorbance vs. wavelength between 400 and 650 nm (Figure 1 in ref. [10]) seems more consistent with our interpretation of an optical transition involving defects (sub-bandgap absorption). Moreover, the steep absorption increase of these powders below 400 nm is consistent with the (indirect) 3.2 eV band-to-band transition mentioned above. The nature of the defects responsible for the sub-bandgap absorption and their energetic position in the bandgap will be discussed in more detail below.

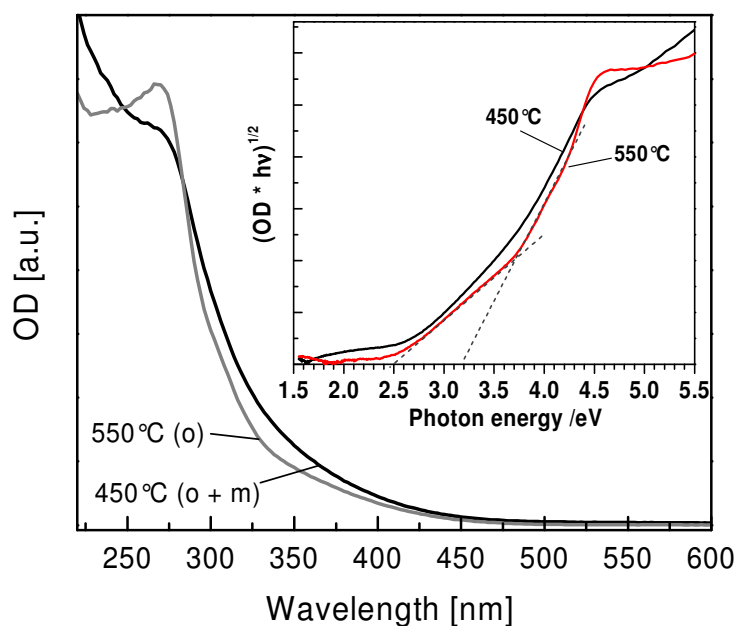


**Figure 4.6:** Optical absorption spectra of undoped  $\text{InVO}_4$  on quartz. Orthorhombic films (annealed at 550 °C) show similar absorption characteristics as films that are predominantly monoclinic (annealed at 450 °C). The insert shows the OD spectra plotted as  $(\text{OD} \times \text{h}\nu)^{1/2}$  vs.  $\text{h}\nu$  and reveal an indirect bandgap of 3.2 eV for the  $\text{InVO}_4$  photoelectrodes.

Figure 4.7 shows the optical absorption coefficient,  $\alpha$ , as a function of wavelength for an orthorhombic  $\text{InVO}_4$  thin film deposited on quartz (insert Figure 4.7). The thickness of the film is  $180 \pm 20$  nm. The values are calculated from the data in Figure 4.6 and the thickness of

the film,  $L$ , using the expression  $\alpha = (OD \times \ln 10) / L$ . The absorption coefficient reaches a maximum of  $2.2 \times 10^7 \text{ m}^{-1}$  at  $\sim 270 \text{ nm}$ , which is comparable to that of  $\text{TiO}_2$  at the same wavelength [28].

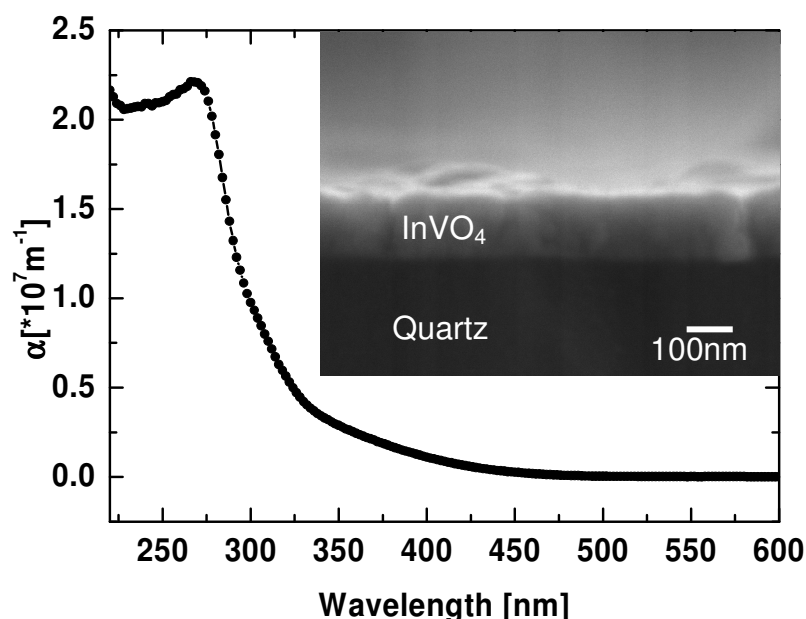


**Figure 4.7:** Absorption coefficient ( $\alpha$ ) of undoped orthorhombic  $\text{InVO}_4$  on quartz annealed at  $550 \text{ }^\circ\text{C}$ . The thickness of the film is determined by a cross-sectional SEM image (insert).

To investigate the photoactivity of the material, a voltammogram was measured while illuminating the film with chopped 375 nm light. Figure 4.8 reveals good rectifying properties with low leakage currents, indicating high-quality films with few pinholes. An anodic photocurrent is observed, confirming that orthorhombic  $\text{InVO}_4$  is an n-type semiconductor. The insert shows a rather modest IPCE of 0.45% at  $1.2 \text{ V}_{\text{SCE}}$ . It should be realized that these  $\sim 70 \text{ nm}$  thick films absorb less than 13% of the incident 375 nm light ( $\alpha = 1.9 \times 10^6 \text{ m}^{-1}$ , Figure 4.6), which results in an absorbed photon-to-current efficiency (APCE) of  $0.45\% / 0.13 \approx 3.5\%$ . Clearly, this is a very low value for a photoanode, indicating a significant amount of recombination.

The photocurrent onset potential is difficult to estimate from the insert in Figure 4.8, but appears to lie somewhere between  $+0.3$  and  $+0.4 \text{ V vs. Ag/AgCl}$ . The response of the photocurrent is fast,  $< 500 \text{ ms}$ , with little over- or undershoot. The absence of pronounced transient effects indicates that there is little or no accumulation of holes at the surface and that charge transfer across the semiconductor/electrolyte interface is not rate limiting. Since only 13% of the incident light is absorbed, the light intensity does not vary much over the thickness of the film. Hence, differences between front- and back-side illumination are negligible and cannot be used to distinguish between electron and hole transport limitations.

The insert of Figure 4.8 reveals that the photocurrent gradually increases with the applied voltage and shows no signs of saturation up to a potential of  $1.4 \text{ V vs. Ag/AgCl}$  for undoped  $\text{InVO}_4$ . The absence of photocurrent saturation over a potential range of  $\sim 1 \text{ Volt}$  for such a

thin film suggests that the depletion layer width is rather small, and that the donor density is high. A small depletion layer is consistent with the increase in the dark anodic current observed at potentials  $>1.0 \text{ V}_{\text{SCE}}$ . This anodic current originates from electrons being injected from the electrolyte into the semiconductor via tunneling, which requires the depletion layer width to be less than  $\sim 3 \text{ nm}$  [29].

In order to decrease the donor density, Ni and Cu were added as acceptor-type dopants. The insert of Figure 4.8 shows that this does not lead to improved photocurrents and that there is still an anodic tunneling current under depletion conditions. Hence, Ni and Cu do not seem to act as efficient acceptors and the decrease of the photocurrent suggests that they may in fact act as recombination centers.

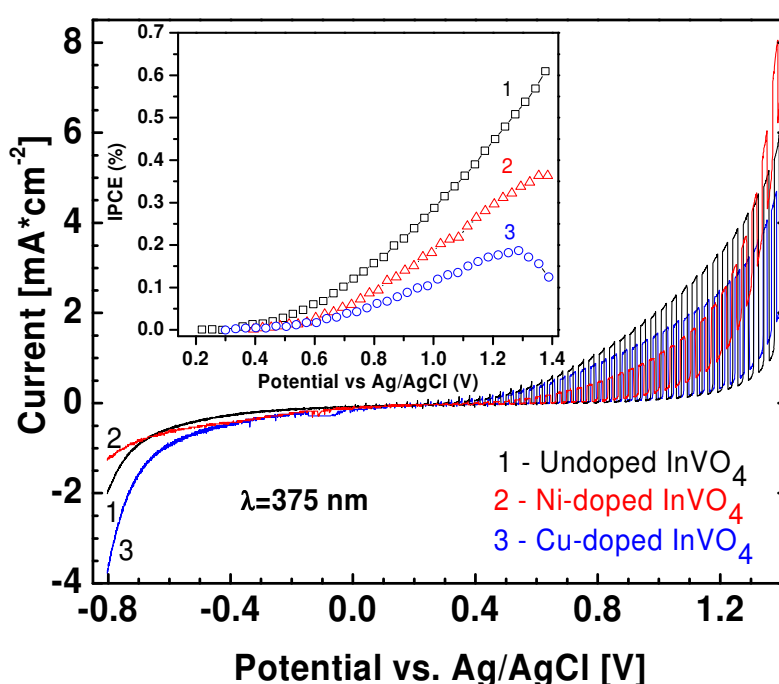


**Figure 4.8:** Current-voltage characteristic of undoped, Ni-doped and Cu-doped  $\text{InVO}_4$  films with a thickness of 70 nm, measured using a chopped 375 nm LED light source. The insert shows the calculated incident photon-to-current conversion efficiencies. Measurements are performed in a 0.1 M KOH aqueous electrolyte ( $\text{pH}=13.6$ ) using a scan rate of 0.5 mV/s.

To determine if the optical absorption corresponds to the photoelectrochemical activity, incident photon-to-current conversion efficiencies (IPCE) have been measured and are presented in Figure 4.9. The photocurrent action spectrum corresponds well with the optical absorption data of Figure 4.6 and the onset of absorption starts at about 450 nm ( $\sim 2.8 \text{ eV}$ ). The measurements are performed at  $0.8 \text{ V}_{\text{Ag/AgCl}}$ , since at this potential the anodic background currents are still small for all samples. For undoped  $\text{InVO}_4$  a maximum IPCE of 0.31% is observed at 330 nm. For such a small photoresponse the contribution of the transparent conducting substrate ( $\text{F}:\text{SnO}_2$ ) to the photocurrent is no longer negligible, especially at

wavelengths below  $\sim 350$  nm (Figure 4.9). While the IPCE increases somewhat for more positive potentials, it would still be limited to less than 1% as can be seen in Figure 4.8. Cu-doping leads to comparable or somewhat smaller photocurrents than for undoped samples, whereas doping with Ni decreases the photocurrent by a factor of about 2. A correction for the actual amount of absorbed light in the films reveals APCE values less than 1.5% for all wavelengths, which confirms the limited photoelectrochemical activity of these films.

While it is not possible to directly compare the efficiency of the presented photoanodes to that of powder-based photocatalysts, one may gain some insight by converting photocurrents to equivalent amounts of hydrogen. Imagine a 70 nm thick  $\text{InVO}_4$  film with an average IPCE of 0.01% between 420 and 450 nm (Figure 4.9). Upon illumination with AM1.5 light, this 30 nm interval alone would generate a photocurrent of  $\sim 0.13 \mu\text{A}/\text{cm}^2$  (obtained by integration of the standard AM1.5 spectrum) [30]. This corresponds to a hydrogen evolution rate of  $76 \mu\text{mole}\cdot\text{g}^{-1}\cdot\text{h}^{-1}$ . By contrast, a hydrogen evolution rate of only  $5 \mu\text{mole}\cdot\text{g}^{-1}\cdot\text{h}^{-1}$  has been reported for  $\text{NiO}_x$ -loaded (i.e., catalyzed)  $\text{InVO}_4$  powders illuminated with a 300 W Xe lamp using a 420 nm high pass filter [10]. This suggests that despite the low IPCE values, thin film  $\text{InVO}_4$  photoanodes are at least an order of magnitude more efficient on a per-gram basis than their powder counterparts in the visible part of the spectrum.

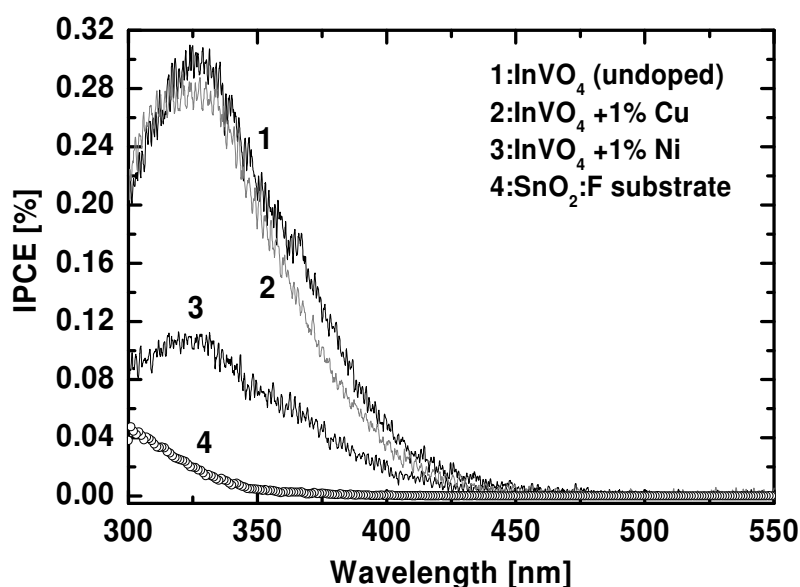


**Figure 4.9:** IPCE spectra of undoped, Cu-doped and Ni-doped  $\text{InVO}_4$  recorded at a potential of 0.8 V vs. Ag/AgCl using front-side illumination. The photoresponse of uncoated FTO is presented for comparison.

#### 4.3.4 Impedance spectroscopy

In order to further investigate the factors that limit the photoresponse of the  $\text{InVO}_4$  thin films, impedance measurements are employed to determine the electrical properties of the material. The measurements have been performed on undoped  $\text{InVO}_4$  films with different thicknesses, as well as on Ni- and Cu-doped  $\text{InVO}_4$ .

Figure 4.10 shows the results for undoped  $\text{InVO}_4$  for three different values of the film thickness and at various applied potentials. The impedance plots contain two regions, a semi-

circle at high frequencies and the beginning of a much larger semi-circle at low frequencies. Based on these observations, the data were fitted using the equivalent circuit shown in Figure 4.11A. During the fit, parameter  $R_l$  was kept fixed (see below), while all other parameters were left free. The fit results are shown as the solid lines in Figure 4.10. From this figure, we conclude that the equivalent circuit of Figure 4.11A provides a good representation of the experimental data for all three film thicknesses in a potential range between  $-0.5$  and  $+0.5$  V vs. Ag/AgCl.

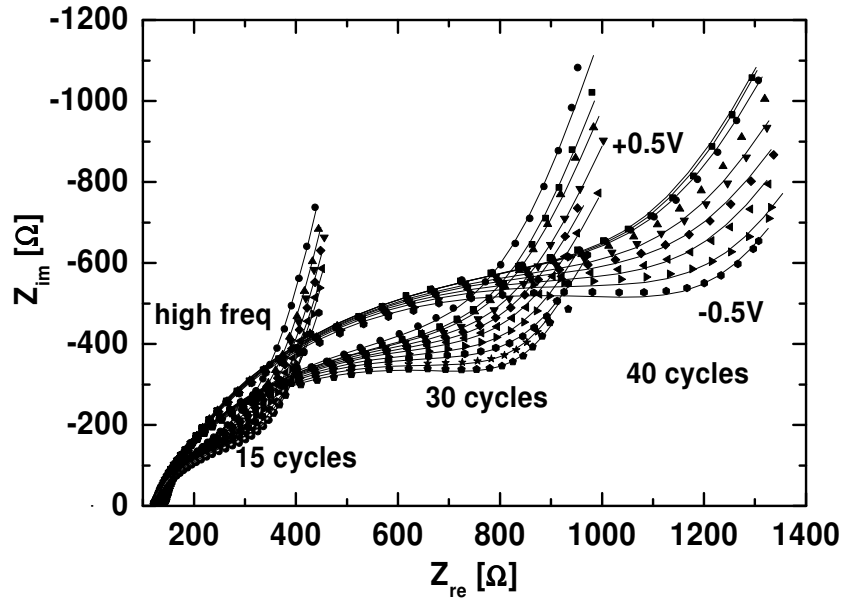


**Figure 4.10:** Impedance spectra of undoped  $\text{InVO}_4$  films with different thicknesses. The perturbation amplitude is 10 mV and the frequency range is  $10^2 - 5 \times 10^5$  Hz. The solid points represent the measured data, whereas the solid lines represent the results from a NLLS fit using the circuit shown in Figure 4.11A. The bulk resistance is about 100  $\Omega$ .

Before interpreting the fitted values for the various equivalent circuit elements, it should be noted that the semicircles are somewhat depressed. This behavior is often observed in practical systems and can be usually attributed to surface or bulk inhomogeneities [31]. This deviation of purely capacitive behavior is commonly modeled by introducing a constant phase element (CPE) to fit the data, as was also done here. The impedance of a CPE is given by  $Z_Q = Y_Q^{-1} (j\omega)^{-n}$ . Depending on the value of  $n$ , the electrical behavior of a CPE ranges between purely resistive ( $n=0$ ) and purely capacitive ( $n=1$ ). For the fitted data in Figure 4.10,  $n$  varied between 0.8 and 0.9. The use of a CPE instead of a pure capacitance complicates its physical interpretation, since the units of  $Q$  are  $\Omega^{-1} \text{s}^n$  instead of  $\Omega^{-1} \text{s}$  ( $=\text{F}$ , for Farad). Hence, one cannot directly calculate the characteristic time constant,  $\tau$ , for an  $RQ$  circuit as one would normally do for an  $RC$  circuit ( $\tau = RC$ ). Hsu and Mansfield showed that the equivalent capacitance of a CPE can be calculated using  $C_Q = Y_0 (\omega_{\max})^{n-1}$  [32]. Here,  $\omega_{\max} = (2\pi f)_{\max}$  is the frequency at which the imaginary value of the impedance has a maximum and  $C_Q$  has the dimension of  $\Omega^{-1} \text{s}$ . Using this expression, the characteristic time constant for an  $RQ$  circuit is given by  $\tau = RC_Q$ .

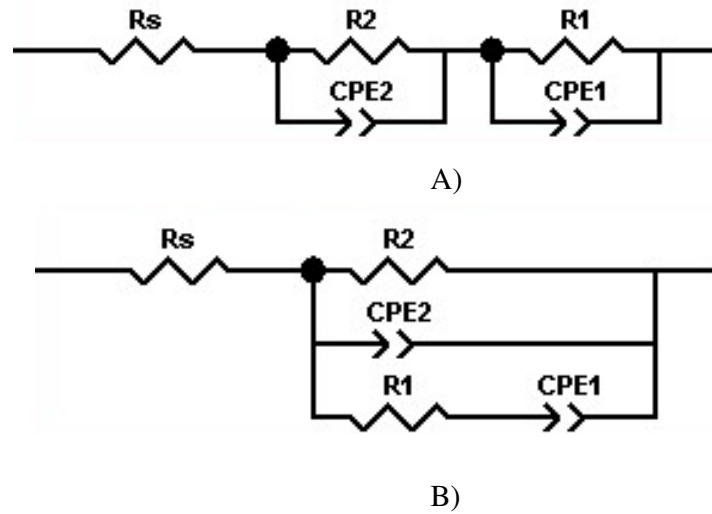


**Figure 4.11:** Two equivalent circuits that both accurately describe the measured impedance data. In circuit (A) the bulk and space charge contributions can be recognized, while circuit (B) is generally used to distinguish space charge ( $R_2$ ,  $CPE2$ ) from surface state ( $R_1$ ,  $CPE1$ ) contributions.

The values for the circuit elements obtained from the fit in Figure 4.10 are shown in Figure 4.12 and Table 4.1. The parameters for the CPE elements have been converted into equivalent capacitances using the procedure outlined above, i.e.,  $C_1$  and  $C_2$  are the equivalent capacitances for CPE elements  $Q_1$  and  $Q_2$ , respectively. Resistance  $R_s$  (not shown) represents the combined ohmic resistance of the wires, the electrolyte, the transparent conducting substrate, and the contact between the wire and the conducting substrate (carbon paste). Its value ranges between 80 and 170  $\Omega$  for different samples and the fitted values for an individual sample vary less than  $\sim 3\%$  over the entire potential range.

As shown in Figures 4.12A and B, the values of  $R_2$  and  $1/C_2$  depend linearly on the film thickness and do not show any significant dependence on the applied potential. This can also be observed in Figure 4.10, where the combination of  $R_2$  and  $C_2$  is responsible for the small semi-circle at high frequencies. Based on these observations, the combination of  $R_2$  and  $C_2$  is attributed to the bulk of the  $\text{InVO}_4$  film. The bulk resistance and capacitance of a material are given by  $R = L/(\sigma A)$  and  $C = \epsilon_0 \epsilon_r A/L$ , respectively, where  $\sigma$  is the conductivity of the material,  $L$  the thickness,  $A$  the surface area of the sample exposed to the electrolyte ( $=2.83 \times 10^{-5} \text{ m}^2$ ),  $\epsilon_r$  the dielectric constant, and  $\epsilon_0 = 8.854 \times 10^{-12} \text{ A}\cdot\text{s}/\text{V}\cdot\text{m}$ . From these expressions and the values of  $R_2$  and  $C_2$ , the conductivity, dielectric constant, and dielectric relaxation time ( $\tau_{\text{bulk}} = R_2 C_2 = \epsilon_0 \epsilon_r / \sigma$ ) of undoped  $\text{InVO}_4$  are calculated for the three different values of the film thickness. A similar analysis is performed for the Ni- and Cu-doped  $\text{InVO}_4$  films.

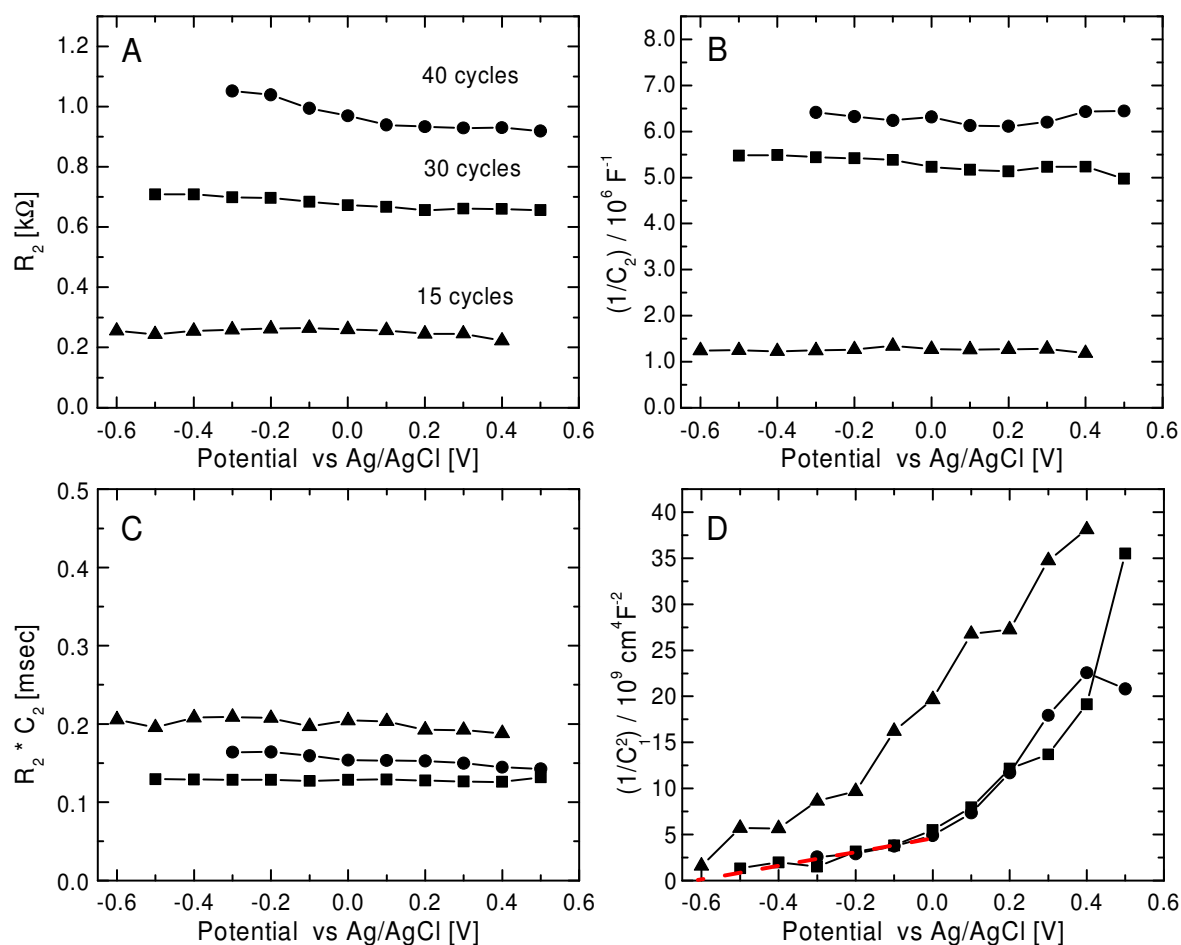


**Figure 4.12:** Results of the NLLS fits of the measured impedance spectra to the circuit of Figure 4.11A, showing the potential dependence of  $R_1$ ,  $C_1$ ,  $R_2$  and  $C_2 C_1$  and  $C_2$  are the equivalent capacitance values that correspond to  $CPE1$  and  $CPE2$ , respectively (see text).  $R_2$  and  $1/C_2$  scale linearly with the film thickness and are attributed to the bulk of the  $\text{InVO}_4$  film, while  $R_1$  and  $C_1$  vary with the applied potential and represent the space charge.

As shown in Table 4.1, all samples show similar values for the conductivity and the dielectric constant of the material, except for the thinnest undoped sample (15 cycles, estimated thickness  $\sim 35$  nm). For such thin films, the surface roughness can no longer be ignored and a correction for the surface area needs to be applied. Indeed, if the actual surface area for an about 35 nm film exceeds the geometrical area by a factor of 2, both the conductivity and the dielectric constant of the film would be in line with those of the thicker films. From the data in Table 4.1 (excluding the results for the 35 nm film), an average dielectric constant of  $50 \pm 3$  is calculated for  $\text{InVO}_4$ .

**Table 4.1:** Values for the equivalent circuit elements, the dielectric relaxation time, the conductivity, the dielectric constant, and the depletion layer width (at  $V=0.4$  V vs. Ag/AgCl) as calculated from the fitted impedance spectra.

InVO <sub>4</sub> (spray cycles)	$L$ [nm]	$R_1$ [ $\Omega$ ]	$R_2$ [ $\Omega$ ]	$\tau(R_2 \times C_2)$ [s]	$\sigma$ [ $\Omega^{-1}m^{-1}$ ]	$\epsilon_r$	$W$ [nm]
Undoped (15)	35	$1.2 \times 10^6$	250	$2 \times 10^{-4}$	$5 \times 10^{-6}$	120	6
Undoped (30)	70	$2.5 \times 10^6$	679	$1.3 \times 10^{-4}$	$3.6 \times 10^{-6}$	53	2
Undoped (40)	100	$1 \times 10^6$	967	$1.5 \times 10^{-4}$	$3.6 \times 10^{-6}$	63	2.4
Ni-doped (30)	70	$8 \times 10^6$	813	$1.4 \times 10^{-4}$	$3 \times 10^{-6}$	49	2.3
Cu-doped (30)	70	$6.1 \times 10^6$	1267	$2.2 \times 10^{-4}$	$2 \times 10^{-6}$	50	2.1

While  $R_2$  and  $C_2$  represent the bulk of the InVO<sub>4</sub> films,  $R_1$  and  $C_1$  are attributed to the space charge region present at the semiconductor/electrolyte interface.  $R_1$  represents the leakage current through the space charge layer that is caused by the presence of pin-holes or other surface imperfections. Its value could be independently determined from the linear slope observed for I-V curves recorded in the dark and was, therefore, kept fixed while fitting the impedance spectra. Its numerical value ranges between 1 and 8 M $\Omega$  for the films under study (Table 4.1).

We briefly note that an alternative interpretation of the impedance spectrum is possible in the form of the equivalent circuit of Figure 4.11B. In this case,  $CPE1$  is usually attributed to the capacitance of surface states, while  $CPE2$  corresponds to the space charge capacitance. Analysis of the impedance data using this circuit yields physically unrealistic values for both these elements, and this interpretation is, therefore, discarded.

As expected for an n-type semiconductor,  $1/C_1^2$  increases when a more positive (anodic) potential is applied (Figure 4.12D), corresponding to an increase in the space charge width  $W$ . From the value of  $C_1$  and the dielectric constant determined above, the space charge width is calculated using the expression for a parallel plate capacitor,  $C_1 = \epsilon_0 \epsilon_r A / W$ . The results, shown in Table 4.1 for a potential of +0.4 V<sub>Ag/AgCl</sub>, indicate that the space charge width is limited to only a few nanometers.

The slope of  $1/C_1^2$  and the intercept with the potential axis can be used to calculate the donor density,  $N_D$ , and the flat band potential,  $V_{FB}$ , respectively, using the Mott-Schottky equation  $\frac{1}{C^2} = \left( \frac{2}{e \epsilon_0 \epsilon_r N_D A^2} \right) \left( V - V_{FB} - \frac{kT}{e} \right)$ . It should be noted that instead of the expected linear dependence on the applied potential,  $1/C^2$  the curve is found to concave upwards. This is attributed to the surface roughness of the film, which leads to an under-estimation of  $A$  at high donor densities and at potentials close to the flatband potential [33]. Therefore, the donor density is calculated from the linear part of the curve at potentials positive of 0 V<sub>Ag/AgCl</sub>, resulting in a donor density of  $6 \times 10^{19}$  cm<sup>-3</sup>. This rather high value and concomitantly small

depletion layer width is indeed consistent with the manifestation of surface roughness effects in the Mott-Schottky plot.

### 4.3.5 Deep donor states

At first sight, the high donor density ( $6 \times 10^{19} \text{ cm}^{-3}$ ) appears to contradict the low value found for the conductivity of bulk  $\text{InVO}_4$  ( $\sim 3 \times 10^{-8} \Omega^{-1} \text{ cm}^{-1}$ , Table 4.1). This can be explained by the donor levels being located deep within the bandgap, so that only a small fraction of the donors are ionized at room temperature. Communication with the conduction band will be slow for such a deep donor level. This is consistent with the low frequencies at which the space charge capacitance response is observed in the impedance spectrum of Figure 4.10, and the large characteristic time constant of the  $R_1C_1$  combination ( $\sim 10$  seconds).

The constant capacitance at high frequencies resembles the behaviour of an insulator and confirms the absence of ionized (shallow) donors in the material. In semiconductor terminology, the  $\text{InVO}_4$  is in the ‘freeze-out’ regime [34,35]. Under these conditions, the concentration of free electrons is equal to the number of ionized (deep) donors, and the Fermi level is located halfway between the donor level and the conduction band minimum [35]. The proposed band diagram is shown in Figure 4.13. When the applied potential,  $(V_A - V_{fb})$ , is smaller than  $\frac{1}{2}(E_C - E_D)/e$ , no donors are ionized and the potential distribution over the film is linear (Figure 4.13A,B). If  $(V_A - V_{fb})$  exceeds  $\frac{1}{2}(E_C - E_D)/e$ , ionization of the deep donors occurs and the additional potential drop is confined to the depletion layer (Figure 4.13C). Due to the high donor density ( $6 \times 10^{19} \text{ cm}^{-3}$ ), the width of the depletion layer ( $W$ ) is small and the Fermi level is effectively ‘pinned’ by the deep donor states.

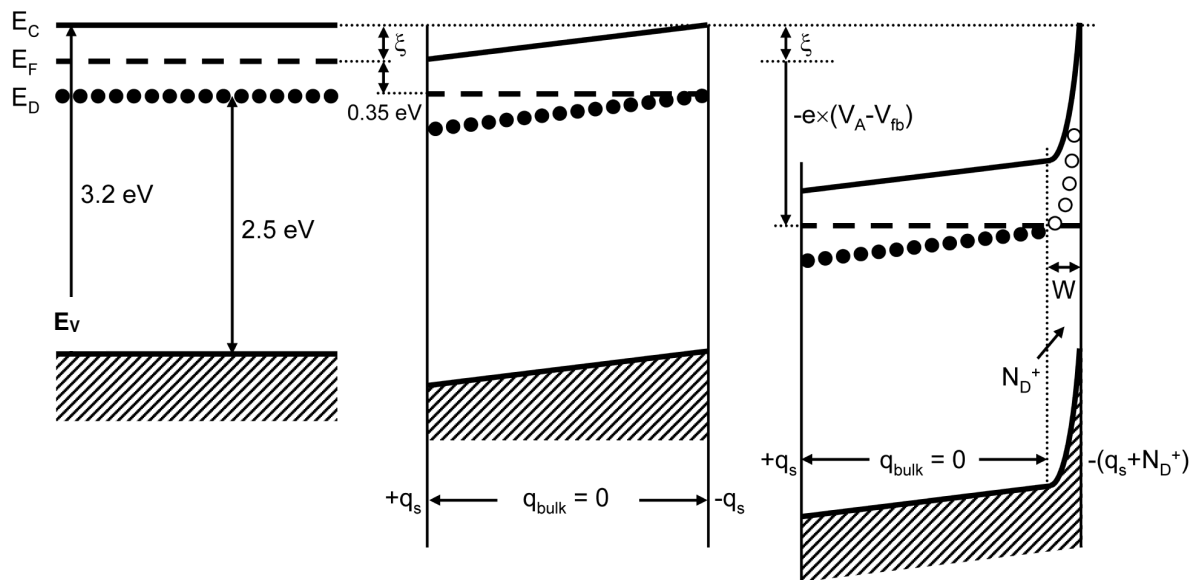


**Figure 4.13:** Proposed band diagram for the spray-deposited  $\text{InVO}_4$  thin films. The (indirect) bandgap is 3.2 eV, with a deep donor level at 0.7 eV below the conduction band edge. When the potential drop across the depletion layer exceeds 0.35 V, the deep donors are ionized. For smaller potential drops, the films behave as an insulator. The visible-light photoresponse of the material between 400 and 650 nm is attributed to optical excitation from the valence band to the ionized (empty) deep donor states.

The presence of empty donor states in the depletion layer is believed to be responsible for the sub-bandgap absorption of InVO<sub>4</sub>. More specifically, the 2.5 eV difference between  $E_D$  and  $E_V$  shown in Figure 4.13 corresponds to the onset of sub-bandgap absorption (insert Figure 4.6). Since  $W$  is limited to a few nanometers from the surface, the amount of sub-bandgap absorption is proportional to the total surface area of the material. For powders prepared with the solid state reaction method, typical crystallite sizes are ~85 nm [16], which corresponds to a specific surface area of 15 m<sup>2</sup>/g. For a 180 nm thick film (Figure 4.7), the specific surface area is 1.2 m<sup>2</sup>/g. This large difference explains why the sub-bandgap absorption in InVO<sub>4</sub> powders [10,36] is much more pronounced than that observed for our thin dense films (Figures 4.6 and 4.7).

Defects with energy levels deep in the bandgap are known to act as efficient recombination centers for electrons and holes. As a result of the high concentration of deep donors, the minority carrier diffusion length in our InVO<sub>4</sub> is presumably limited to a few nanometers and most (if not all) charge carriers generated in the bulk of the material will recombine. Only the electron-hole pairs generated within the depletion layer can contribute to the photocurrent, and it is the small value of  $W$  that explains the poor photocurrent efficiency of the InVO<sub>4</sub> films. The fact that  $W$  is much smaller than both the film thickness and the penetration depth of the light explains why no saturation of the photocurrent is observed over a fairly large (~1 Volt) potential range (insert Figure 4.8).

#### 4.3.6 Photocurrent onset and flat band potential

From Figure 4.12D, the intercept of  $I/C_{SC}^2$  with the potential axis ( $V_0$ ) is estimated to be at ~0.6 V vs. Ag/AgCl. Since the system has a fairly high donor density, a significant part of the potential may drop across the Helmholtz layer. This leads to a correction term of  $(e\epsilon_0\epsilon_r N_D / 2C_H^2)$  [37], assuming that the deep donor states are in thermal equilibrium with the conduction band. This is a reasonable assumption, since the impedance measurements are carried out at a constant (dc) potential. In addition, the potential drop over the bulk needs to be considered. Inspection of Figures 4.13A and 4.13B shows that ionisation of the deep donors requires that  $V_A > (V_{FB} + \zeta)$ , where  $\zeta$  is the potential drop over the bulk. When this is taken into account, the flatband potential can be obtained from the expression:

$$V_{FB} = V_0 - \frac{kT}{e} + \frac{e\epsilon_0\epsilon_r N_D}{2C_H^2} + \zeta \quad (4.1)$$

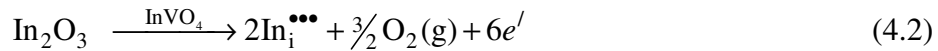
Using  $\epsilon_r=50$ ,  $N_D=6 \times 10^{19}$  cm<sup>-3</sup>,  $\zeta=0.35$  V, and an estimated Helmholtz capacitance of  $C_H=20$   $\mu$ F/cm<sup>2</sup>, a flatband potential of -0.97 V vs. Ag/AgCl is calculated. Only a very small part of the potential drops across the Helmholtz layer (~5 mV). For a pH of 13.6, the flatband potential corresponds to a value of -0.04 V vs. reversible hydrogen (RHE). This implies that hydrogen evolution is thermodynamically possible with InVO<sub>4</sub>, as was indeed observed by Ye et al. in their work on Pt-loaded InVO<sub>4</sub> photocatalyst powders [10].

When comparing Figures 4.8 and 4.12D, the photocurrent onset potential (+0.3-0.4 V<sub>Ag/AgCl</sub>) is found to be ~1.3 V more positive than the flatband potential. Large anodic shifts of the flatband potential under illumination have been observed for many

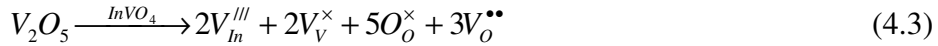
systems [38], and are usually attributed to either recombination in the space charge layer [39], hole trapping at surface defects [40], or hole accumulation at the surface due to poor charge transfer kinetics [38]. Recombination in the space charge layer is a distinct possibility in our case because of the high concentration of deep donors (recombination centers). In addition, structural defects associated with, e.g., grain boundaries may be present and act as recombination centers. A large positive potential is necessary to ensure that the electric field is strong enough to separate the charges before trapping occurs. In view of the fact that no O<sub>2</sub> evolution is observed for InVO<sub>4</sub> powder [10], the material may also suffer from intrinsically poor hole transfer kinetics. However, this probably plays a minor role in our material since hole accumulation at the surface is expected to lead to transients in the photocurrent response, and these are not observed in Figure 4.8.

#### 4.3.7 Defect chemistry considerations

Further improvement of InVO<sub>4</sub> photocatalysts requires a better understanding of the chemical nature of the deep donor states observed in this work. Although the presence of impurities cannot be excluded (a donor density of 6×10<sup>19</sup> cm<sup>-3</sup> corresponds to a concentration of ~0.05%), deviations from the ideal In/V ratio of 1:1 seem a more likely explanation. For example, excess indium ions may act as donors when incorporated on interstitial sites. Using the standard Kröger-Vink notation [41], this reaction can be written as:



Alternatively, an excess of vanadium may result in the formation of indium and oxygen vacancies:

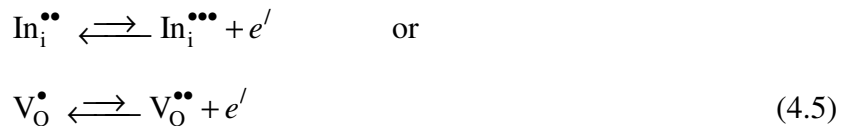


For the tri-valent indium vacancies the following reaction is possible:



The formation of highly charged vanadium interstitial ( $V_i^{\bullet\bullet\bullet\bullet}$ ) or vanadium vacancies ( $V_{\text{V}}^{\text{IV}}$ ) is energetically very unfavorable and will not be considered here.

Both indium interstitials and oxygen vacancies may act as deep donors, and the corresponding ionization reactions can be written as:



Analogous defect reactions can be written for the case of an excess of vanadium. According to Figure 4.13, the ionization energy of the donor is ~0.7 eV. Oxygen vacancies usually have ionization energies between 0.5 - 2.0 eV, whereas somewhat smaller values are usually reported for cation interstitials [41]. Although this slightly favors the possibility of

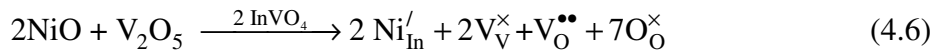
oxygen vacancies being the source of the deep donors, a more definite assignment requires further investigation and is beyond the scope of this paper.

Actual deviations from the ideal molecularity are impossible to avoid and may easily exceed the 0.05% that corresponds to the measured donor density. Since the  $\text{In}_2\text{O}_3\text{-V}_2\text{O}_5$  phase diagram indicates that  $\text{InVO}_4$  is a line compound [42], the solubility limit is quickly reached and segregation of one of the binary oxides will readily occur. However, the concentration of these oxides will be rather low and may be impossible to observe with x-ray diffraction or Raman spectroscopy. This is especially true for synthesis methods using liquid solutions, in which the ions are mixed on a molecular level and any segregated binary oxide phase will be finely dispersed.

We will now briefly discuss the effects of the incorporation of the Ni and Cu dopants into the  $\text{InVO}_4$  lattice. The ionic radius of 6-fold coordinated  $\text{In}^{3+}$  is 80 pm, slightly larger than the ionic radii for  $\text{Cu}^{2+}$  (73 pm) and  $\text{Ni}^{2+}$  (69 pm). In contrast, the ionic radius of 4-fold coordinated  $\text{V}^{5+}$  is 36 pm, significantly less than the corresponding radii for  $\text{Cu}^{2+}$  (57 pm) and  $\text{Ni}^{2+}$  (55 pm). Hence,  $\text{Cu}^{2+}$  and  $\text{Ni}^{2+}$  are presumably located on the  $\text{In}^{3+}$  sites, especially when one considers that the formation of singly-charged acceptor defects is energetically much more favorable than the formation of the triply-charged defects that would be formed if either Cu or Ni would substitute for  $\text{V}^{5+}$ .

From Figures 4.8 and 4.9, it is clear that doping with Ni or Cu does not lead to improved photocurrents. Moreover, Table 4.1 shows no significant effect on the space charge width, which implies that these dopants do not form ionized donors or acceptors. Presumably, Ni and Cu substitute for indium to form recombination centers (deep acceptors). Similar phenomena have been observed in numerous studies on  $\text{TiO}_2$  doped with transition metal ions, where cation doping was found to enhance visible light absorption but to decrease the overall efficiency due to enhanced recombination in the UV part of the spectrum [43]. Alternatively, the dopants may segregate out to form NiO or  $\text{Cu}_x\text{O}$  phases. As mentioned before, these highly dispersed phases would be difficult to observe experimentally because of the small dopant concentrations (1%).

From defect-chemical considerations, it would actually be quite difficult to dope a ternary metal oxide with a binary metal oxide. This is illustrated by Eq. (4.3) above, where substitutional doping on the indium sublattice requires the creation of highly charged vanadium vacancies in order to conserve the stoichiometry of lattice sites. A possible solution to facilitate the incorporation of divalent acceptor-type dopants into  $\text{InVO}_4$  would be to use co-dopants. For example, by adding equimolar amounts of vanadium oxide the energetically unfavorable formation of highly charged defects can be avoided:



For a 1% dopant concentration, the resulting composition would be  $\text{Ni}_{0.01}\text{In}_{0.99}\text{VO}_{3.995}$ . The success of this approach for ternary oxides in general will depend on the solubility limits of the individual compounds, which in turn depend on the energy required to form compensating defects versus the energy required to form a second phase.

Finally, we briefly point out that the Ni-doped  $\text{InTaO}_4$  photocatalysts reported by Zou et al. can be described in a similar manner, with a composition formally given by

Ni<sub>x</sub>In<sub>1-x</sub>TaO<sub>4-x/2</sub> [7]. The sub-bandgap photoresponse was attributed to internal d-d transitions in the Ni ion but, as the authors point out, it is unclear how such a transition can result in electron-hole separation. The results presented in this paper suggest that oxygen vacancies acting as deep donors may provide an alternative explanation for the observed visible-light photoresponse in Ni-doped InTaO<sub>4</sub>.

#### 4.4 Conclusions

Table 4.2 summarizes the intrinsic material properties of compact n-type InVO<sub>4</sub> films as determined in this study. The flatband potential of -0.04 V<sub>RHE</sub> confirms its previously reported ability to evolve hydrogen, while the (indirect) bandgap of 3.2 eV indicates that the material is primarily active in the UV part of the spectrum. A striking feature of these InVO<sub>4</sub> thin films is the virtual absence of shallow donors, as evidenced by the long dielectric relaxation time (~10<sup>-4</sup> s). This behavior is very different from that of most binary metal oxide photoanodes, such as TiO<sub>2</sub> and Fe<sub>2</sub>O<sub>3</sub>, for which shallow donor concentrations in the order of 10<sup>17</sup> cm<sup>-3</sup> or higher are usually found. The small sub-bandgap absorption at 2.5 eV is attributed to the presence of ionized deep donors in the space charge region of the material. The high concentration of deep donors results in a very narrow space charge region in which the photogenerated electrons and holes are separated (few nm). Hence, the amount of visible light absorption scales with the total surface area, which explains why InVO<sub>4</sub> powders absorb much more visible light than compact films.

**Table 4.2:** Intrinsic properties of orthorhombic InVO<sub>4</sub> determined in this study.

Properties of InVO <sub>4</sub>	
Bandgap (indirect)	3.2 ± 0.2 eV
Absorption coefficient	2.2×10 <sup>7</sup> m <sup>-1</sup> @270 nm
	9.8×10 <sup>7</sup> m <sup>-1</sup> @300 nm
	2.9×10 <sup>6</sup> m <sup>-1</sup> @350 nm
	1.1×10 <sup>6</sup> m <sup>-1</sup> @400 nm
	2.6×10 <sup>5</sup> m <sup>-1</sup> @450 nm
	4.2×10 <sup>4</sup> m <sup>-1</sup> @500 nm
Dielectric constant	50±3 (see Table 4.1)
Deep donor state	E <sub>D</sub> = E <sub>C</sub> -0.7 eV
Flatband potential	-0.04 V vs. RHE
Conduction band minimum, E <sub>C</sub>	-0.39 V vs. RHE
	( ~4.1 eV vs. vacuum)
Valence band maximum, E <sub>V</sub>	2.81 V vs. RHE
	( ~7.3 eV vs. vacuum)

Although the compact InVO<sub>4</sub> films outperform InVO<sub>4</sub> powders by at least one order of magnitude in terms of μmole·g<sup>-1</sup>·h<sup>-1</sup>, the IPCE is still two orders of magnitude less than current

state-of-the-art metal oxide photoanodes [4]. The main bottleneck appears to be the high concentration of (deep) donors and a concomitantly small depletion layer width. Ni or Cu dopants do not improve the performance and seem to act as recombination centers rather than acceptor-type dopants. To fully determine the potential of InVO<sub>4</sub>-based photoanodes, it is imperative to identify the deep donors responsible for the sub-bandgap photoresponse and to determine whether or not these or other defects, such as grain boundaries, may also act as recombination centers. The next step is to gain control over the shallow and deep donors in InVO<sub>4</sub> during synthesis.

Accurate control over the stoichiometry of metal ions is one of the key challenges that have to be addressed. While this can be easily achieved with simple binary oxides, it is far from trivial for ternary and higher oxides. This is the price one has to pay for the new opportunities offered by the exciting, but largely unexplored class of complex metal oxide photoanodes.

## References

- [1]. R. van de Krol, Y. Q. Liang, and J. Schoonman, *J. Mater. Chem.*, **18**, 2311 (2008).
- [2]. S. Licht, B. Wang, S. Mukerji, T. Soga, M. Umeno, and H. Tributsch, *J. Phys. Chem. B*, **104**, 8920 (2000).
- [3]. M. Grätzel, *Nature*, **414**, 338 (2001).
- [4]. A. Kay, I. Cesar, and M. Grätzel, *J. Am. Chem. Soc.*, **128**, 15714 (2006).
- [5]. B. D. Alexander, P. J. Kulesza, I. Rutkowska, R. Solarzka, and J. Augustynski, *J. Mater. Chem.*, **18**, 2298 (2008).
- [6]. M. A. Butler and D. S. Ginley, *Chem. Phys. Lett.*, **47**, 319 (1977).
- [7]. Z. Zou, J. Ye, K. Sayama, and H. Arakawa, *Nature*, **414**, 625 (2001).
- [8]. F. E. Osterloh, *Chem. Mater.*, **20**, 35 (2008).
- [9]. J. Yin, Z. Zou, and J. Ye, *J. Phys. Chem. B*, **107**, 61 (2003).
- [10]. J. Ye, Z. Zou, M. Oshikiri, A. Matsushita, M. Shimoda, M. Imai, and T. Shishido, *Chem. Phys. Lett.*, **356**, 221 (2002).
- [11]. K. Sayama, A. Nomura, T. Arai, T. Sugita, R. Abe, M. Yanagida, T. Oi, Y. Iwasaki, Y. Abe, and H. Sugihara, *J. Phys. Chem. B*, **110**, 11352 (2006).
- [12]. S. H. Baeck, T. F. Jaramillo, D. H. Jeong, and E. W. McFarland, *Chem. Commun.*, 390 (2005).
- [13]. M. Woodhouse, G. S. Herman, and B. A. Parkinson, *Chem. Mater.*, **17**, 4318 (2005).
- [14]. Assuming a H<sub>2</sub> evolution rate of 5 μmole·g<sup>-1</sup>·h<sup>-1</sup> (which is considered to be promising [7,10]) on a 1 m<sup>2</sup>/g powder with an average particle diameter of 1.3 μm, the average surface site (2x10<sup>15</sup> cm<sup>-2</sup>) releases only one H<sub>2</sub> molecule per 6.6 hours. In contrast, a 2 mA/cm<sup>2</sup> photocurrent at a promising photoanode with a roughness factor of 21 [5] corresponds to a surface site turnover rate of 1 H<sub>2</sub> molecule per 7 seconds.
- [15]. S. Zhang, C. Zhang, H. Yang, and Y. Zhu, *J. Solid State Chem.*, **179**, 873 (2006).
- [16]. L. Zhang, H. Fu, C. Zhang, and Y. Zhu, *J. Solid State Chem.*, **179**, 804 (2006).
- [17]. M. Oshikiri, M. Boero, J. Ye, F. Aryasetiawan, and G. Kido, *Thin Solid Film*, **445**, 168 (2003).
- [18]. J. Ye, Z. Zou, H. Arakawa, M. Oshikiri, M. Shimoda, A. Matsushita, and T. Shishido, *J. Photochem. Photobiol. A: Chem.*, **148**, 79 (2002).
- [19]. When using InCl<sub>3</sub> as an alternative indium precursor the solution remained green, indicating the presence of V<sup>3+</sup> (Indium ions are always colorless in aqueous solutions, regardless of the oxidation state). Films deposited using InCl<sub>3</sub> are powdery and amorphous, with no traces of InVO<sub>4</sub> and small quantities of cubic In<sub>2</sub>O<sub>3</sub>.
- [20]. E. J. Baran and M. E. Escobar, *Spectrochim. Acta A*, **41**, 415 (1985).
- [21]. J. Twu and T.-H. G. a. K.-H. C. Chih-Feng Shih, *J. Mater. Chem.*, **7**, 2273 (1997).
- [22]. W. Chen, L. Mai, J. Peng, Q. Xu, and Q. Zhu, *J. Solid State Chem.*, **177**, 377 (2004).

- [23]. X. J. Wang, H. D. Li, Y. J. Fei, X. Wang, Y. Y. Xiong, Y. X. Nie, and K. A. Feng, *Appl. Surf. Sci.*, **177**, 8 (2001).
- [24]. V. Golovanov, M. A. Maki-Jaskari, T. T. Rantala, G. Korotcenkov, V. Brinzari, A. Cornet, and J. Morante, *Sens. Actuators. B*, **106**, 563 (2005).
- [25]. G. Korotcenkov, V. Brinzari, M. Ivanov, A. Cerneavschi, J. Rodriguez, A. Cirera, A. Cornet, and J. Morante, *Thin Solid Film*, **479**, 38 (2005).
- [26]. M. Touboul, K. Melghit, P. Benard, and D. Louer, *J. Solid State Chem.*, **118**, 93 (1995).
- [27]. M. Touboul, K. Melghit, and P. Benard, *Eur. J. Solid State Inorg. Chem.*, **31**, 151 (1994).
- [28]. H. Takikawa, T. Matsui, T. Sakakibara, A. Bendavid, and P. J. Martin, *Thin Solid Film*, **348**, 145 (1999).
- [29]. S. R. Morrison, "*Electrochemistry at semiconductor and oxidized Metal Electrodes*", Plenum Press, New York and London (1980).
- [30]. A. B. Murphy, P. R. F. Barnes, L. K. Randeniya, I. C. Plumb, I. E. Grey, M. D. Horne, and J. A. Glasscock, *Int. J. Hydrogen Energy*, **31**, 1999 (2006).
- [31]. J. B. Jorcin, M. E. Orazem, N. Pebere, and B. Tribollet, *Electrochim. Acta*, **51**, 1473 (2006).
- [32]. C. H. Hsu and F. Mansfeld, *Corrosion*, **57**, 747 (2001).
- [33]. J. Schoonman, K. Vos, and G. Blasse, *J. Electrochem. Soc.*, **128**, 1154 (1981).
- [34]. S. M. Sze, *Physics of semiconductor devices*, Wiley (1981).
- [35]. R. F. Pierret, *Advanced semiconductor fundamentals, Modular series on solid state devices*, Addison-Wesley (1989).
- [36]. H. L. M. Chang, T. J. Zhang, H. Zhang, J. Guo, H. K. Kim, and D. J. Lam, *J. Mater. Res.*, **8**, 2634 (1993).
- [37]. W. P. Gomes and F. Cardon, *Prog. Surf. Sci.*, **12**, 155 (1982).
- [38]. R. Memming, *Semiconductor Electrochemistry*, Wiley-VCH (2001).
- [39]. J. Reichmann, *Appl. Phys. Lett.*, **36**, 574 (1980).
- [40]. L. M. Peter, J. Li, and R. Peat, *J. Electroanal. Chem.*, **165**, 29 (1984).
- [41]. F. A. Kröger, *The chemistry of imperfect crystals*, Wiley (1964).
- [42]. M. Touboul and A. Popot, *J. Therm. Analysis*, **31**, 117 (1986).
- [43]. X. Chen and S. S. Mao, *Chem. Rev.*, **107**, 2891 (2007).



# Chapter 5

## Characterization of structured $\alpha$ -Fe<sub>2</sub>O<sub>3</sub> photoanodes prepared via electrodeposition and thermal oxidation of iron<sup>\*</sup>

### Abstract

*In this paper we explore the feasibility of using electrodeposition as a low-cost, versatile and easily upscalable technique for preparing  $\alpha$ -Fe<sub>2</sub>O<sub>3</sub> (hematite) photoanodes for water splitting applications. The photoelectrodes are prepared on transparent conducting glass substrates by electrodeposition of Fe, using a non-aqueous precursor solution at room temperature, followed by thermal oxidation in air. Variations in deposition parameters yield films with diverse morphologies. The effects of the different morphologies on the structural, optical, and photoelectrochemical properties are investigated by photocurrent measurements under AM1.5 illumination. The photocurrent could be improved by growing the first part of the Fe film at low current densities, yielding a dense underlayer, followed by the deposition of a more structured, porous film at high current densities. X-ray diffraction (XRD) reveals that high deposition currents result in a smaller crystallites and a (110) preferred orientation. This orientation is favorable when using hematite as a photoanode, since the conductivity in the [110] direction is known to be up to four orders of magnitude higher than in directions perpendicular to this.*

---

<sup>\*</sup> This chapter is based on: Cristina S. Enache, Y. Q. Liang, and Roel van de Krol, *Thin Solid Films*, **520** (2011), 1034-1040.

## 5.1 Introduction

Thin metal oxide films such as  $\text{TiO}_2$ ,  $\text{WO}_3$ ,  $\text{ZnO}$ ,  $\text{CuO}$ , and  $\text{Fe}_2\text{O}_3$  are of major importance for solar cells, chemical sensors, liquid crystal displays, photoelectronics, etc. Of particular interest is the development of metal oxide photoelectrodes that are able to convert water into hydrogen and oxygen using sunlight [1]. Iron oxide ( $\alpha\text{-Fe}_2\text{O}_3$ ) with a bandgap of 2.1 eV is a promising photoanode candidate that can absorb solar radiation below 590 nm, which represents up to 32% of the total solar irradiance ( $1000 \text{ W/m}^2$ ) [2]. Additionally, it exhibits good chemical stability in aqueous solutions, it is non-toxic, and it is a low-cost material. However, iron oxide has two important limitations, i.e, a short hole-diffusion length of 2-4 nm and slow surface reaction kinetics [3,4].

By making highly structured and nanoporous electrodes, both these intrinsic material's limitations can be overcome. With such a morphology the photo-generated holes only have to travel a short distance to the electrolyte, while the large specific surface area avoids charge transfer limitations. Grätzel et al. [5-7] have recently reported promising results on nanostructured  $\alpha\text{-Fe}_2\text{O}_3$  grown by Atmospheric Pressure Chemical Vapor Deposition (APCVD), but scale-up of this technique is challenging due to the use of highly toxic  $\text{Fe}(\text{CO})_5$  as a precursor. Hagfeldt et al. [4,8] have shown that by growing nanorods of hematite (~50 nm in diameter) perpendicular to the substrate, the transport and collection of photo-generated charges is more efficient compared to flat films, or to films with nanorods oriented parallel to the substrate. However, they obtain only modest efficiencies (IPCE of 8% at 350 nm with no applied voltage) even though no grain boundaries are present [3]. From this study and also the study of Björkstén [9], it appears that  $\alpha\text{-Fe}_2\text{O}_3$  grown from aqueous solutions generally gives low photocurrents. One possible explanation is that the formation of intermediate hydroxide phases, such as  $\alpha\text{-FeOOH}$  (goethite) [9] or  $\beta\text{-FeOOH}$  (akaganeite) [10] introduce defects in the final hematite structure.

A further refinement might be possible with an array of individual free-standing nanowires, each with a thickness that is in the order of the hole diffusion length (less than 10 nm). Such nanowire arrays of  $\text{Fe}_2\text{O}_3$  have been successfully prepared by several groups. For example, Chueh et al. [11] reported synthesis of  $\text{Fe}_2\text{O}_3$  nanowires on iron-nickel alloys at temperatures between 400 and 700 °C. Furthermore, Yu et al. [12] showed that by so-called 'substrate friendly oxidation' using a hot plate, an iron foil could be transformed into a network of nanowires of  $\text{Fe}_2\text{O}_3$  at temperatures as low as 300 °C. In our own lab,  $\text{Fe}_2\text{O}_3$  nanowires have been obtained by thermal oxidation of Fe foil at 800 °C in air [13]. However, the photoresponse is quite poor, which is probably due to the unavoidable presence of FeO and/or  $\text{Fe}_3\text{O}_4$  at the interface between the metallic Fe and the  $\text{Fe}_2\text{O}_3$ . By depositing thin Fe films on a conducting substrate we can, in principle, avoid these undesired phases since the film can be completely converted into  $\text{Fe}_2\text{O}_3$ . The first challenge is to synthesize such structures in a controlled fashion with accurate control over the doping density. Practical applications require that this can be done with a low-cost technique that can be easily scaled-up and which uses non-toxic precursors. Spray pyrolysis [14-16] gives reasonable control over dopants and can be easily scaled up. However, it cannot meet the second challenge, which is to obtain a nanostructured morphology.

In this study we explore an alternative synthesis route that consists of growing metallic Fe using non-aqueous electrodeposition, followed by subsequent thermal oxidation treatment to form highly structured Fe<sub>2</sub>O<sub>3</sub>. As a convenient abbreviation for this method, the acronym “*EDOX*” will be used from here on. This method has two important advantages. First, by growing in non-aqueous media, we can easily incorporate transition metal dopants such as Ti. Second, the direct thermal oxidation avoids also the formation of intermediate hydrated phases, such as FeOOH.

## **5.2 Experimental details**

### **5.2.1 Film preparation**

Electrodeposition was carried out in a two-electrode setup. Transparent conducting glass (FTO, 15  $\Omega$ /square F:SnO<sub>2</sub>, TEC 15, Libbey-Owens-Ford) was used as the working electrode with an equally large piece of pure platinum foil as the counter electrode. The distance between the working and the platinum electrode was about ~1.5 cm and was kept constant during the deposition process. Potential control was provided by an EG&G Par 273 potentiostat/galvanostat in galvanostatic mode.

Prior to the film deposition, the FTO substrates were cleaned by ultrasonic rinsing, first in acetone and subsequently in ethanol, and dried using compressed nitrogen. Careful cleaning of the substrate was found to be essential for the deposition of homogeneous films.

Two different non-aqueous solvents, ethylene-glycol (EG) and dimethyl-sulfoxide (DMSO), were used to prepare so-called E-type and D-type electrodes, respectively. E-type electrodes were deposited using 0.01 M FeSO<sub>4</sub>·7H<sub>2</sub>O (Merck, 99.5%) +0.005 M (NH<sub>4</sub>)<sub>2</sub>SO<sub>4</sub> (Lamers & Pleuger, 99%) in EG as an electrolyte. The electrodeposition solution for D-type electrodes was prepared from 0.1 M anhydrous FeCl<sub>2</sub> (Alfa Aesar, 99.5%) dissolved in DMSO (Merck, 99.9%). Silicon-doped films were prepared by adding 0.1 mM tetraethyl-orthosilicate (TEOS, Alfa Aesar 99.9%) to the electrodeposition solution.

After electrodeposition, the Fe films were rinsed in ethanol (99.9%, J.T. Baker with 2% MEK) and dried using a flow of compressed nitrogen. This was followed by thermal oxidation in air at 500 °C for 5 hours using a tube furnace.

### **5.2.2 Characterization techniques**

The morphology was investigated using a JSM 6500F scanning electron microscope (SEM). The film thickness of the sample was measured using a surface profilometer (Veeco Dektak 8). The crystal structures of the as-deposited Fe films and the oxidized electrodes were analysed using X-ray diffraction (XRD) with a Bruker D8 Advance diffractometer, either in the grazing incidence mode with a scintillator detector using Cu-K $\alpha$  radiation, or in the Bragg-Brentano configuration with a LynxEye 1D detector using Cu-K $\alpha$  radiation. The Raman spectra were recorded with a home-built setup using a continuous-wave Nd:YVO<sub>4</sub> laser with a wavelength of 532 nm (Millennia, Spectra Physics). The backscattered light was recorded by a CCD camera cooled with liquid nitrogen (model LN/CCD-1100PB, Princeton

Instruments) via a monochromator (model 340E, Spex) with an 1800 grooves/mm grating. The 532 nm laser line was removed with a holographic notch filter (Supernotch, Kaiser Optical Systems). Optical transmission and reflection spectra of the Fe<sub>2</sub>O<sub>3</sub> films were recorded using a Perkin-Elmer Lambda 900 spectrophotometer equipped with an integrating sphere (Labsphere).

Photoelectrochemical experiments were performed using a conventional three-electrode cell with a quartz window, a Pt counter electrode, and a Ag/AgCl reference electrode with a 3M KCl solution (REF 321, Radiometer Analytical). A solution of 1M KOH (J.T. Baker) in demineralized and deionized water (Milli-Q, 18.2 MΩcm) was used as the electrolyte. Electrical contacts were made by connecting copper wires to an uncoated part of the FTO with conducting carbon paste (Alfa Aesar, 042466). The working area of the electrodes exposed to the electrolyte is  $2.83 \times 10^{-5} \text{ m}^2$  ( $\phi=6 \text{ mm}$ ) for all samples. The potential was controlled by an EG&G model 283 potentiostat.

A 200 W tungsten halogen lamp in combination with a grating monochromator (Acton SPro 150) was used to irradiate the sample for IPCE measurements. High-pass filters (Schott) were used to remove the second order of the diffracted light. The light intensity was measured as a function of wavelength with a calibrated photodiode (PD 300-UV, Ophir). A solar simulator (EPS 1200S, K.H. Steuernagel Lichttechnik GmbH) was used to simulate AM1.5 sunlight ( $100 \text{ mW/cm}^2$ ). A UV-enhanced aluminum mirror (Melles Griot) was used to direct the light from the solar simulator to the vertically mounted sample under an angle of 90°. Unless noted otherwise, the scan rates were 10 mV/s for the I-V curves, and 2 nm/min for the Incident Photon-to-current Conversion Efficiency (IPCE) measurements.

## 5.3 Results and discussion

### 5.3.1 Electrolyte solution and sample preparation

Due to the presence of crystal water in the FeSO<sub>4</sub> powder, a small amount of hydrogen is generated at the working electrode during electrodeposition. This adversely influences the homogeneity of the deposited films and competes with iron deposition. It has been shown previously that hydrogen evolution as a side reaction also causes changes in the crystalline structure of the film [17]. By positioning the working electrode under an angle, as illustrated in Figure 5.1, the hydrogen bubbles easily free themselves from the substrate, resulting in the deposition of homogeneous films. Due to the poor solubility of FeSO<sub>4</sub> in EG, the concentration is rather low and the deposition rate was limited to  $0.8 \text{ mA/cm}^2$ . In contrast, anhydrous FeCl<sub>2</sub> dissolves very well in DMSO, and since this electrolyte solution is water-free no hydrogen generation was observed.

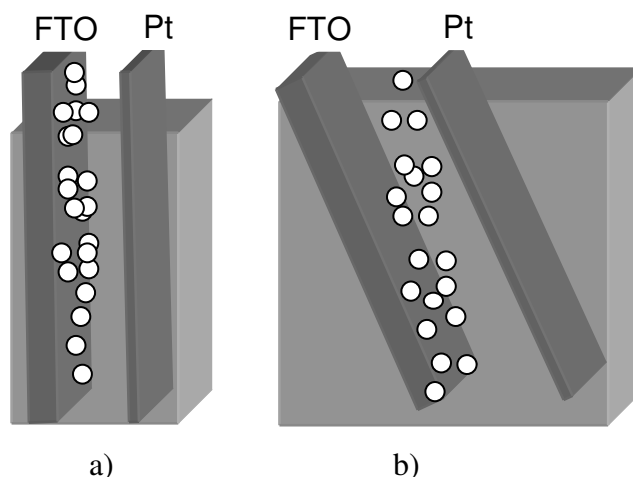


**Figure 5.1:** Schematic diagram of the cell configuration used during the electrodeposition of Fe from  $\text{FeSO}_4 \cdot 7\text{H}_2\text{O}$  in an ethylene-glycol solution, for which hydrogen evolution takes place at the working electrode. a) hydrogen bubbles travel along the electrode surface, causing vertical striations; b) hydrogen bubbles free themselves from the FTO substrate when placed under an angle, resulting in much improved surface quality.

### 5.3.2 Appearance and morphology

The as-deposited iron films show good uniformity, are well adherent to the substrate and have a shiny grey or matte black color depending on the deposition parameters. Typically, samples deposited at low current densities ( $<2 \text{ mA/cm}^2$ ) have a shiny grey appearance and are semi-transparent. In contrast, poorly transparent matte black films are obtained at higher current densities.

After oxidation at  $500 \text{ }^\circ\text{C}$  in air, the resulting  $\text{Fe}_2\text{O}_3$  electrodes have a shiny red-brown color when prepared in DMSO at low current densities, i.e.,  $0.8\text{-}2 \text{ mA/cm}^2$  ( $<2 \text{ V}$ ). A matte red-brown color was obtained for samples prepared at current densities  $\geq 3 \text{ mA/cm}^2$  ( $>3 \text{ V}$ ). An orange-yellowish color is obtained for the thinner E-type electrodes prepared using ethylene-glycol as a solvent. Photographs of these three types of samples are shown in Figure 5.2.

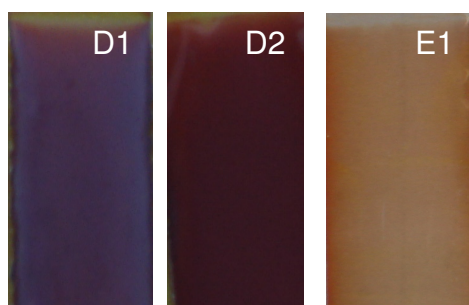


**Figure 5.2:** Pictures of Fe electrodes deposited in a non-aqueous solution after oxidation to  $\text{Fe}_2\text{O}_3$  in air at  $500 \text{ }^\circ\text{C}$  for 5 hours. D1) deposited at  $0.8 \text{ mA/cm}^2$  for 300 s in DMSO; D2) deposited at  $3 \text{ mA/cm}^2$  for 180 s in DMSO; E1) deposited at  $0.8 \text{ mA/cm}^2$  for 2400 s in ethylene-glycol.

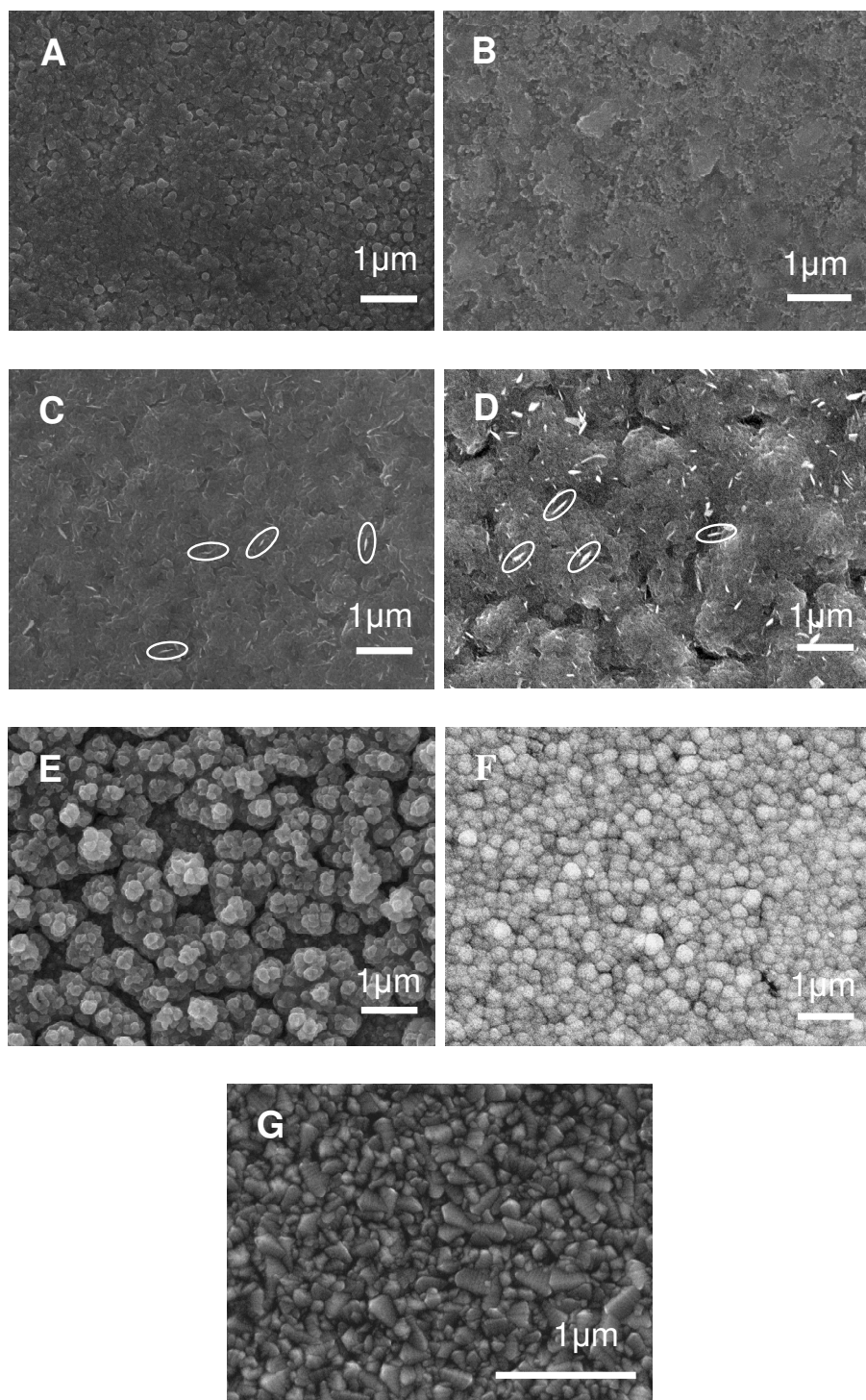


**Figure 5.3:** Scanning electron microscopy (SEM) images of  $\text{Fe}_2\text{O}_3$  electrodes deposited in EG (A) and in DMSO (B-F) at various current densities: A)  $0.3 \text{ mA/cm}^2$ , 2400 s; B)  $0.8 \text{ mA/cm}^2$ , 300 s; C)  $0.8 \text{ mA/cm}^2$ , 600 s; D)  $0.5 \text{ mA/cm}^2$  for 90 s plus  $2 \text{ mA/cm}^2$  for 180 s; E)  $0.5 \text{ mA/cm}^2$  for 90 s plus  $3 \text{ mA/cm}^2$  for 180 s; F)  $0.8 \text{ mA/cm}^2$  for 600 s using 1% Si (TEOS) in the electrolyte solution. G) represents the morphology of F:SnO<sub>2</sub> substrate. All presented electrodes were oxidized in air at 500 °C for 5 hours. The circles in C and D indicate the presence of nano sized needle-like features.

SEM micrographs of the electrodes prepared using EG reveal more or less spherical particles of ~0.1-0.2  $\mu\text{m}$  that have grown together (Fig. 5.3A). Due to the poor solubility of FeSO<sub>4</sub> in EG and correspondingly long time needed for electroplating, these samples were not investigated further.

For the D-type electrodes, grown using dimethyl-sulfoxide (DMSO) as a solvent, various morphologies could be obtained by changing the deposition current and time. As shown in Figs. 5.3B-E, the porosity increases with increasing current density. At low current densities, the particles merge together into platelets resulting in fairly compact films (Fig. 5.3B). For these low current densities, a longer deposition time results in the formation of nanosized needle-like features parallel with the substrate (Fig. 5.3C). The formation of these features apparently requires a certain minimum film thickness. Similar nanosized features are observed for an electrode prepared for a shorter time at an intermediate current density of 2 mA/cm<sup>2</sup> (Fig. 5.3D). At the highest current density of 3 mA/cm<sup>2</sup>, no nanosized needle-like features are observed. Instead, a highly porous film composed of 100-200 nm particles stacked in a columnar fashion is formed, as shown in Fig. 5.3E.

The presence of Si in the form of tetraethyl-orthosilicate (TEOS), dissolved in the DMSO precursor solution, changes the morphology of the deposited iron films, see Fig. 5.3F. The electrodes are more compact and consist of regular spherical particles with a diameter between 100 and 150 nm. This change in morphology is not unexpected, since it has been shown previously that organic additives present in the electrolyte solution can have a strong effect on the grain size and the surface morphology of electrodeposited oxides [18,19].

The thickness for all Fe<sub>2</sub>O<sub>3</sub> samples shown in Fig. 5.3 have been determined using DekTak measurements. Figure 5.4 shows the correlation between the thickness and the total amount of charge consumed during the electrodeposition of Fe. The theoretical thickness-charge relationship, assuming 100% deposition efficiency of a fully dense film, is also shown. Although the data show some scatter, two trends can be observed. The first observation is that higher deposition rates result in seemingly thicker films. This is due to the increase in porosity at higher current densities, consistent with the observations from Figure 5.3. Secondly, the deposition efficiency of the Si-doped sample and the sample deposited in ethylene glycol is much smaller than that of the undoped samples. Since the thickness is less than the theoretically expected thickness for fully dense films, this is attributed to unknown side-reactions such as reduction of trace amounts of water.

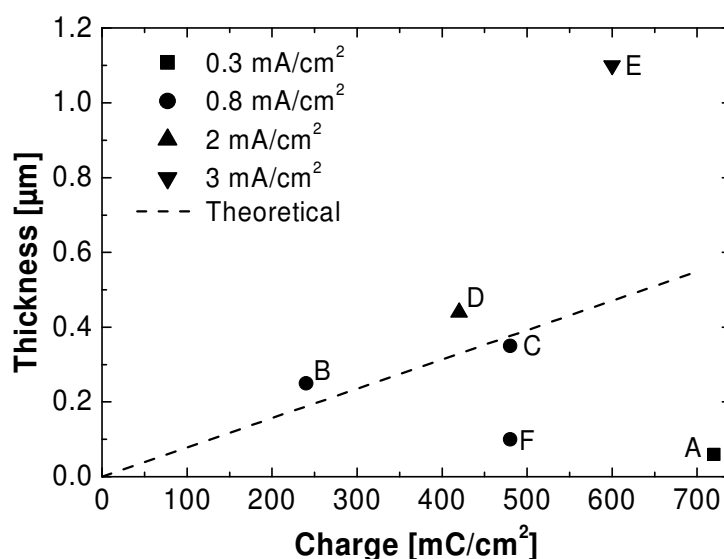


**Figure 5.4:** Relationship between the measured thickness and the amount of charge consumed during the electrodeposition of metallic Fe for various deposition current densities. The dashed line shows the expected thickness for fully dense films, assuming a deposition efficiency of 100% and 2 electrons per Fe atom. The sample labels correspond to those in Fig. 5.3.

### 5.3.3 Structural characterization

XRD measurements (Fig. 5.5) reveal that all as-deposited iron films are crystalline and have the cubic  $\alpha$ -Fe structure with its main peak (110) at  $2\theta=44.6^\circ$  (JCPDS 06-0696). The other peaks are attributed to the FTO substrate and are marked with an asterisk (\*). After the high-temperature oxidation treatment in air, the film is converted to  $\alpha$ -Fe<sub>2</sub>O<sub>3</sub> (hematite, JCPDS 33-0664) as can be seen from the XRD peaks in Figure 5.5 (bottom). The conversion to hematite is also observed for Fe films deposited in ethylene glycol (not shown). The size and the orientation of the crystallites has been determined from the width and relative areas of the (104) and (110) peaks, and are shown in Table 5.1. The crystallite size clearly decreases with increasing growth rate. Moreover, the orientation of the crystallites is not random; for low growth rates, the c-axis is perpendicular to the sample surface, while a high growth rates the relative intensity of the (110) peak increases. A (110) orientation is favorable for electron transport [5,20], which is known to be highly anisotropic in hematite [21,22]. Optimal electron transport therefore requires these Fe<sub>2</sub>O<sub>3</sub> photoanodes to be deposited at high current densities.

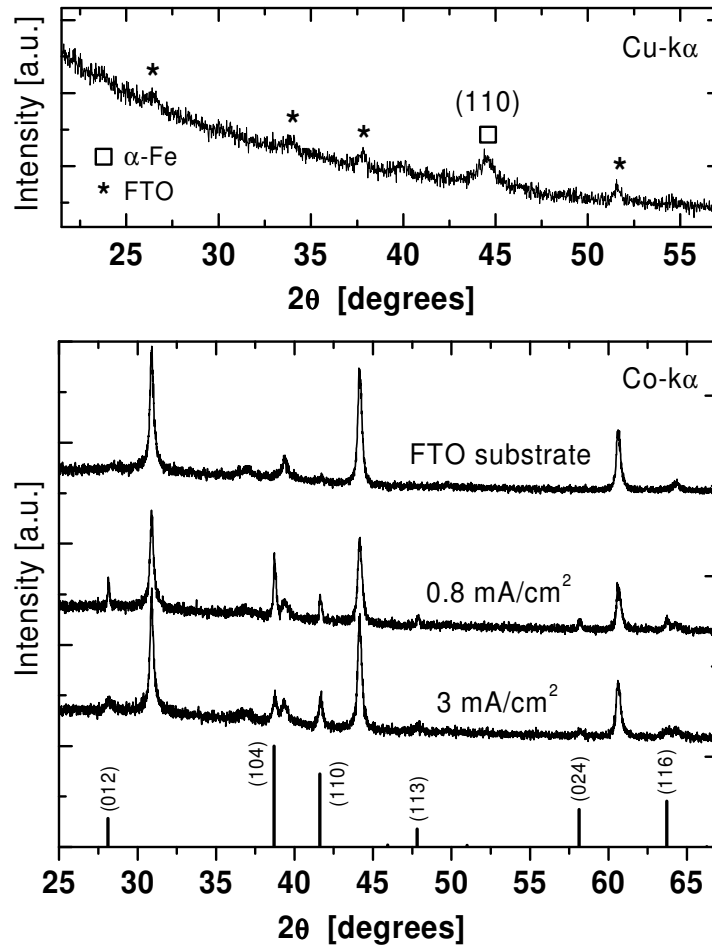


**Figure 5.5:** Top panel: Grazing incidence XRD spectra of as deposited Fe using a DMSO electrolyte solution. Bottom panel: XRD spectra of the bare FTO substrate (top curve), and of the EDOX films prepared at current densities of 0.8 mA/cm<sup>2</sup> and 3 mA/cm<sup>2</sup>. The hematite reference peaks (JCPDS 33-0664) are shown at the bottom of the graph.

**Table 5.1:** Crystallites sizes and peak area ratios for the (104) and (110) peaks of hematite films made by thermal oxidation of electrodeposited Fe films.

Deposition Conditions	XRD peak	Crystallite Size (nm)	Peak area ratio (110)/(104)
0.8 mA/cm <sup>2</sup>	(104)	53 ± 3	0.43
	(110)	52 ± 5	
3 mA/cm <sup>2</sup>	(104)	30 ± 5	1.16
	(110)	34 ± 4	
JCPDS 33-0664			0.72

The Raman spectrum for the sample prepared in DMSO (Fig. 5.6) shows peaks at 409, 500 and 612  $\text{cm}^{-1}$ , which correspond to the well known main hematite peaks at 413, 499 and 612  $\text{cm}^{-1}$  [23-25]. No other impurity phases are observed. In contrast, the samples deposited in EG show an additional peak at 655  $\text{cm}^{-1}$ , which corresponds to the main peak of magnetite,  $\text{Fe}_3\text{O}_4$  [23]. Significant amounts of magnetite are not uncommon in  $\alpha\text{-Fe}_2\text{O}_3$  films and should be avoided since they adversely affect the photoresponse [16,26,27]. No magnetite peak is observed in the XRD patterns of the EG samples, which indicates that the magnetite phase is present as either very small crystallites, amorphous grains, or as a thin surface layer that covers the hematite particles.

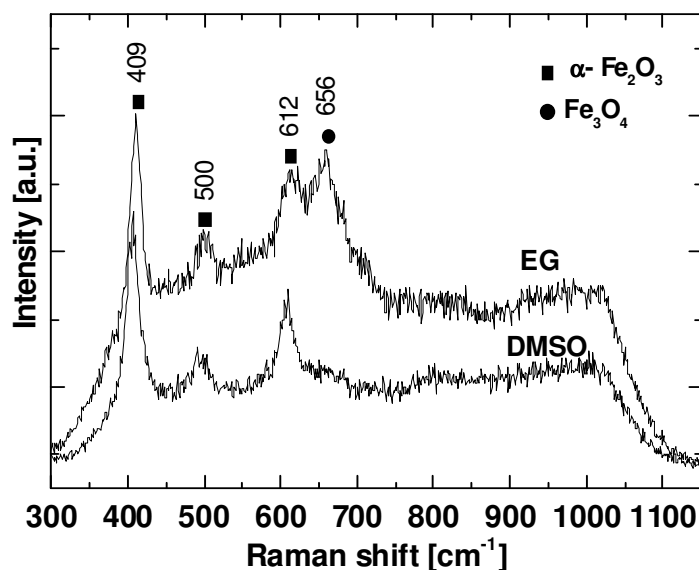


**Figure 5.6:** Raman spectra of  $\text{Fe}_2\text{O}_3$  electrodes prepared by electrodeposition in ethylene-glycol (EG) and dimethyl-sulfoxide (DMSO) solutions. The data are obtained for samples A and D of Fig. 5.3, respectively.

A typical optical absorption spectrum of a  $\text{Fe}_2\text{O}_3$  D-type electrode is presented in Figure 5.7. Apart from variations in the amount of scattering due to the different morphologies, no significant differences in the shape of the absorption spectrum are observed between the samples. The absorption starts at  $\sim 650$  nm and reaches a maximum at  $\sim 440$  nm. The inset shows  $(\alpha h\nu)^{1/2}$  as a function of  $h\nu$  from which the (indirect) bandgap of  $\text{Fe}_2\text{O}_3$  can be estimated. From the intersection of the baseline with the linear part of the absorption onset a bandgap of  $\sim 2.1$  eV is found, in good agreement with previously reported values in the literature [8,27].

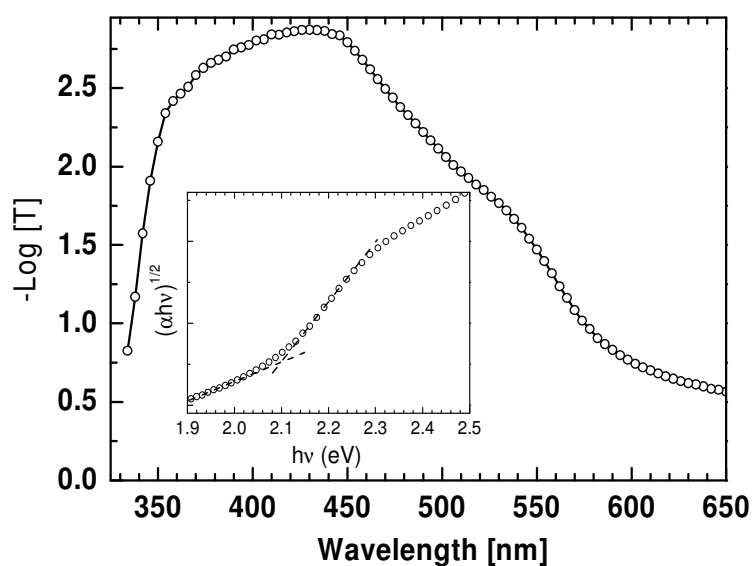


**Figure 5.7:** Absorption spectra of a hematite D-type electrode corrected for the absorption of the conducting glass substrate (but not for scattering). The inset illustrates the extrapolated (indirect) bandgap value of Fe<sub>2</sub>O<sub>3</sub>. The data are obtained for sample B of Fig. 5.3.

### 5.3.4 Photoelectrochemical characterization

Current-potential measurements have been performed in the dark and under AM1.5 simulated sunlight. As can be seen in Figure 5.8, a significant difference in the photocurrent is observed by illuminating the sample via the electrolyte-electrode (EE) interface or via the substrate-electrode interface (SE). For a film thickness of  $\sim 250$  nm the side of irradiation has no influence on the photocurrent. In contrast, for thicker electrodes ( $\sim 350$  nm, prepared under the same conditions) the SE illumination gives a three times higher photoresponse than under EE illumination. Moreover, the photoresponse of the 350 nm films is smaller than that of the 250 nm films. These observations clearly indicate that poor electron transport through the bulk of the Fe<sub>2</sub>O<sub>3</sub> is limiting the photocurrent [28]. This is consistent with undoped  $\alpha$ -Fe<sub>2</sub>O<sub>3</sub> being an insulator [27] and with our previous report indicating that doping with donor-type dopants is essential to improve the conductivity [29]. Interestingly, a small shift of the onset potential towards more negative potentials is observed for the thickest sample under SE illumination. An explanation for this cathodic shift will be given below.

From these results shown in Figure 5.9A, B similarly prepared electrodes exhibit approximately the same photoresponse, indicating good reproducibility of the *EDOX* process. Closer inspection reveals a small but systematic decrease of the photocurrent with increasing thickness under EE illumination. This is consistent with the electron-transport limitations mentioned above. However, when illuminating the sample via the substrate-electrode interface (SE, Figure 5.9B) the photoresponse shows a slight increase with increasing film thickness up to a current density of 1.3 mA/cm<sup>2</sup>. This opposite trend indicates that the holes can travel more efficiently towards the electrolyte/semiconductor interface with increasing

deposition current. This is indeed consistent with the enhanced porosity observed at higher electrodeposition currents (Fig. 5.3).

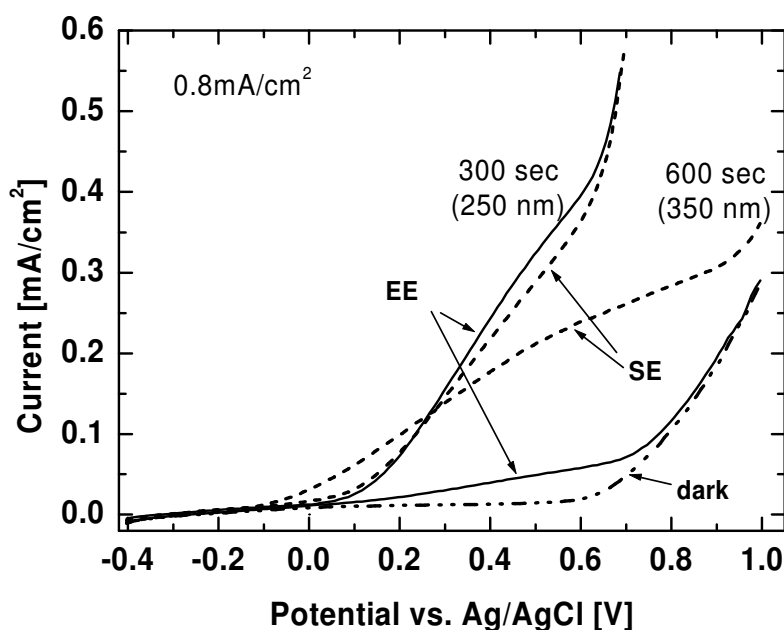


**Figure 5.8:** Voltammograms of D-type  $\text{Fe}_2\text{O}_3$  electrodes grown with  $0.8 \text{ mA/cm}^2$  and different deposition times. Measurements are performed using both electrolyte-electrode (EE) and substrate-electrode (SE) illumination (AM1.5,  $100 \text{ mW/cm}^2$ ). The dark voltammogram corresponds to the 350 nm thick sample.

The I-V curves in Figures 5.8 (SE) and 5.9B reveal that longer deposition times (Fig. 5.8, SE) as well as higher deposition currents (Fig. 5.9B) cause a small cathodic shift of the photocurrent onset potential. This shift is attributed to the formation of the nano-sized needle-like features observed in Figure 5.3. The strong curvature of these features can lead to an enhanced catalytic activity for oxygen evolution [30], which may explain the increased photocurrent at more cathodic potentials. The rapid increase of both the dark current and photocurrent at  $+0.6 \text{ V vs. Ag/AgCl}$  is caused by the direct electrochemical oxidation of water. This effect is delayed to a potential of  $+0.9 \text{ V vs. Ag/AgCl}$  for thicker samples. This indicates a certain potential drop across the  $\text{Fe}_2\text{O}_3$  film, which is consistent with the fact that these films are undoped and not very conducting.

It should be noted that the stability of the *EDOX* photoanodes is quite good. The photocurrent-voltage measurements performed under the solar simulator show no significant changes after storing the samples in air for 2 months.

Kay et al. [5] have seen beneficial effects of  $\text{SiO}_2$  underlayers in the form of a cathodic shift of the flatband potential. We have found a similar effect for a thin  $\text{SnO}_2$  underlayer [29]. Here, we investigate if dense, slowly grown underlayers of Fe (which are later oxidized to  $\text{Fe}_2\text{O}_3$ ) can have similar beneficial effects. For electrodes deposited at higher current densities ( $2 \text{ mA/cm}^2$ ), the presence of a thin underlayer of  $\text{Fe}_2\text{O}_3$  deposited at lower current densities ( $0.5 \text{ mA/cm}^2$ ) indeed results in a  $\sim 30\%$  increase in photocurrent (see Figure 5.10, curves A and B). This marked improvement is believed to be caused by a lower concentration of

(micro)structural defects when growing the structured Fe films on a dense Fe underlayer instead of growing them directly on FTO. This is supported by the observation that the underlayer was found to improve the adhesion between the Fe<sub>2</sub>O<sub>3</sub> and the FTO, as evidenced by the absence of delamination ('peeling-off') that was sometimes observed for the thickest films (>1 $\mu$ m).

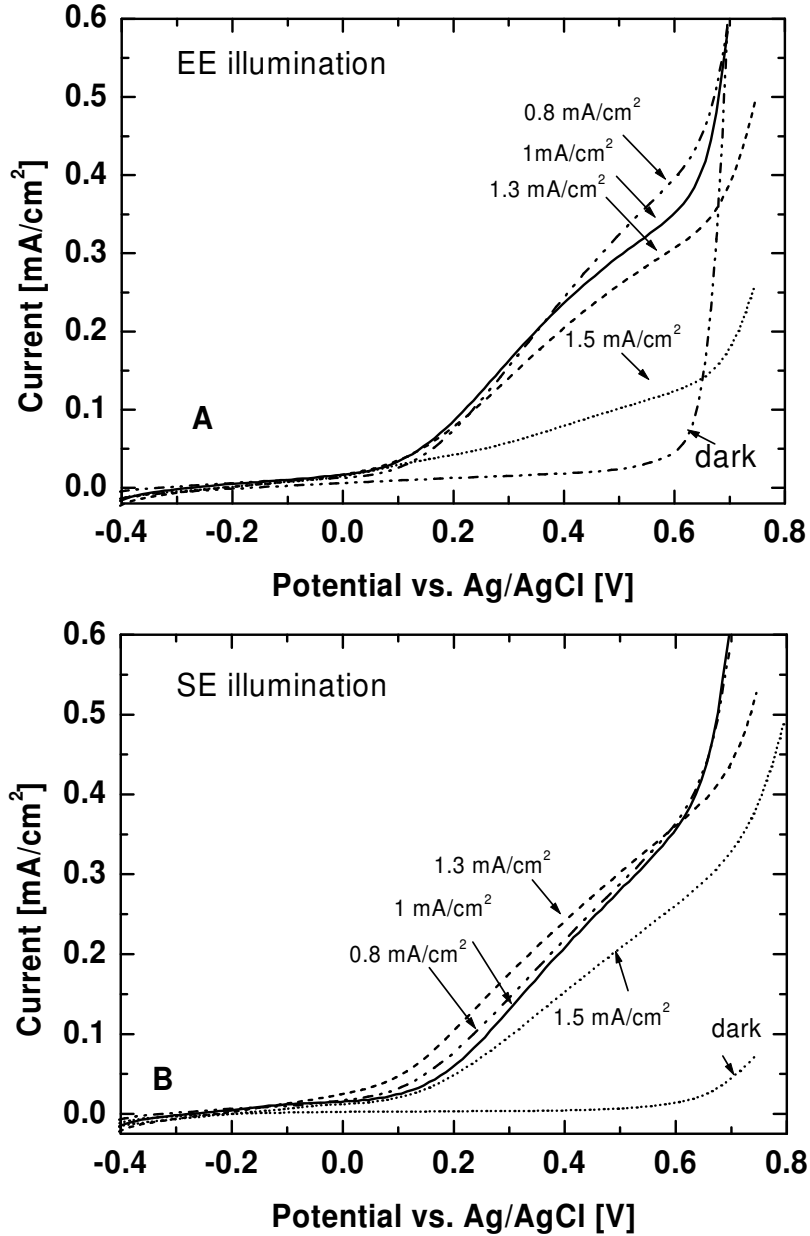


**Figure 5.9:** AM1.5 and dark voltammograms of D-type Fe<sub>2</sub>O<sub>3</sub> electrodes electrodeposited at different current densities (i.e., growth rates) for 300 s. For illumination via the electrolyte, the current decreases with increasing growth rate, whereas the opposite is observed for illumination via the substrate. The dark voltammograms corresponds to the 0.8 mA/cm<sup>2</sup> (graph A) and 1.5 mA/cm<sup>2</sup> (graph B).

Figure 5.10 indicates that the photocurrent onset potential depends on the growth rate of the films. The sample of curve D is grown at  $0.8 \text{ mA/cm}^2$  and has a  $\sim 0.13 \text{ V}$  more anodic onset potential, i.e.,  $+0.07 \text{ V vs. Ag/AgCl}$ . The samples of curves A, B, and C are all grown at  $2 \text{ mA/cm}^2$  (with or without a slowly grown Fe underlayer) and all have an identical onset potential of  $-0.06 \text{ V vs. Ag/AgCl}$ . The more cathodic onset potential for samples deposited at high growth rates can be explained by the formation of catalytically active needle-like features, as discussed above. For deposition current densities  $\geq 3 \text{ mA/cm}^2$  vertical columns of nano-particles are formed (see also Fig. 5.3E). While such a morphology is expected to be beneficial in view of the small hole diffusion length, the photocurrent for these samples was found to be less than  $0.09 \text{ mA/cm}^2$  at  $0.4 \text{ V vs. Ag/AgCl}$  (not shown). In this case the presence of an underlayer does not improve the photocurrent. Presumably, the photo-generated charges are not efficiently collected due to either poor intrinsic electron transport, or to recombination at the grain boundaries that are present between the particles. A similar effect has been reported previously for nanoporous  $\text{Fe}_2\text{O}_3$  electrodes based on spherical particles, where the large amount of grain boundaries between the nanosized particles also caused extensive recombination [9].

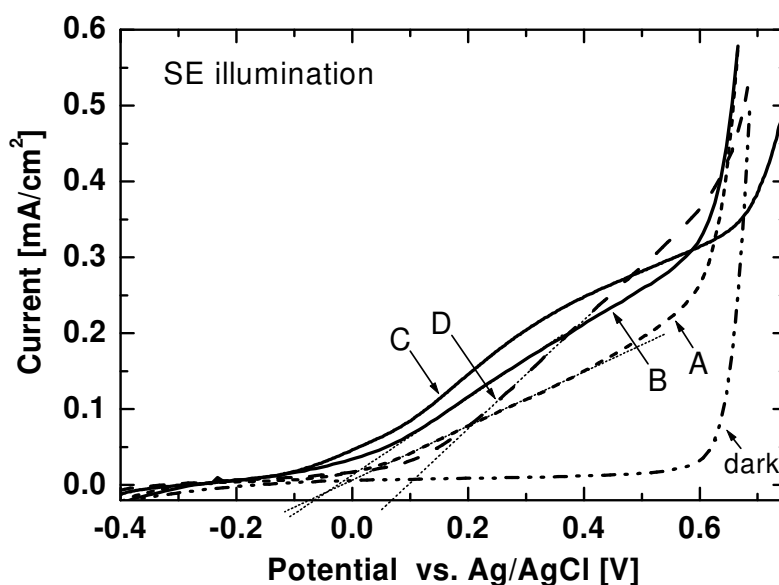


**Figure 5.10:** AM1.5 and dark voltammograms of D-type  $\text{Fe}_2\text{O}_3$  electrodes deposited at various current densities, both with (solid) and without (dashed) a slowly grown  $\text{Fe}_2\text{O}_3$  underlayer: A)  $2 \text{ mA/cm}^2$  for 90 s; B)  $0.5 \text{ mA/cm}^2$  for 60 s (underlayer) +  $2 \text{ mA/cm}^2$  for 90 s; C)  $0.5 \text{ mA/cm}^2$  for 120 s (underlayer) +  $2 \text{ mA/cm}^2$  for 180 s; D)  $0.8 \text{ mA/cm}^2$  for 300 s. The dark IV curve corresponds to sample B.

While the presence of a silicon precursor in the solution has a significant effect on the morphology (Fig. 5.3), it does not improve the photocurrent. This appears to contradict our previous work on spray-deposited  $\text{Fe}_2\text{O}_3$  where silicon was found to act as a donor-type dopant, resulting in significantly improved photocurrents [29]. However, it is known that electrodeposited silicon has a strong tendency to oxidize when trace amounts of oxygen are

present in the solution [31]. Hence, the silicon in the *EDOX* films is presumably present as electrically inactive silicon oxide clusters, and not as a substitutional dopant.

Figure 5.11 illustrates an IPCE spectrum for an *EDOX* Fe<sub>2</sub>O<sub>3</sub> photoanode deposited at 0.8 mA/cm<sup>2</sup> in DMSO, measured at 0.4 V vs. Ag/AgCl. The IPCE starts to increase below ~600 nm, which is in agreement with the optical absorption spectrum (Figure 5.7) and the 2.1 eV indirect bandgap reported for Fe<sub>2</sub>O<sub>3</sub> [8,27]. Multiplying the IPCE with the AM1.5 spectrum [2] and integrating over the absorption range of Fe<sub>2</sub>O<sub>3</sub> [5] gives a predicted AM1.5 photocurrent of ~0.1 mA/cm<sup>2</sup> (not shown). Surprisingly, this is much lower than one would expect based on the 0.2 mA/cm<sup>2</sup> photocurrent that this film shows under AM1.5 illumination (Fig. 5.9). This is caused by extensive recombination, as evidenced by the pronounced transient decay of the photocurrent as shown in the inset of Figure 5.11. When illuminating the sample with the much higher (white) light intensities (100 mW/cm<sup>2</sup>) of a solar simulator, the decay of the photocurrent can be suppressed almost completely, as shown in Figure 5.12. Such behaviour has also been observed for nanoporous TiO<sub>2</sub> and is usually explained in terms of interfacial electron traps at the semiconductor/electrolyte interface [32]. At low light intensities, trapping and de-trapping of electrons generate a transient photocurrent response, the time constant of which is determined by the trapping kinetics. At high light intensities all trap sites remain filled, yielding a faster response and a higher quantum yield [32].

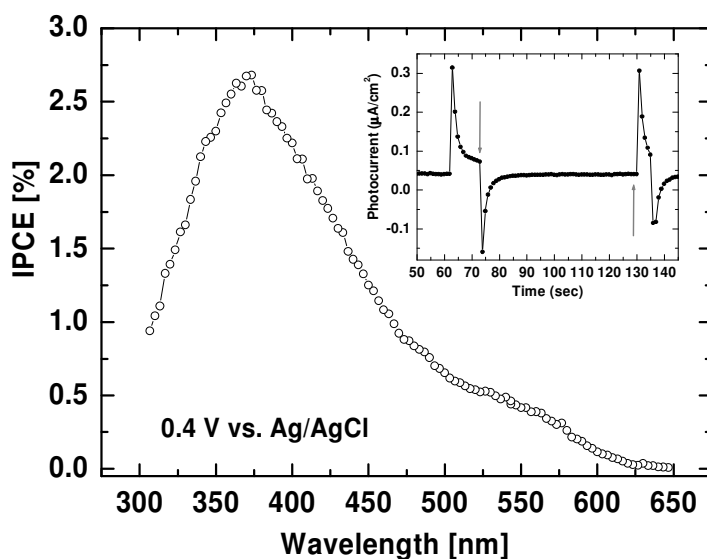


**Figure 5.11:** Incident Photon-to-current Conversion Efficiency (IPCE) of a 250 nm Fe<sub>2</sub>O<sub>3</sub> *EDOX* electrode deposited at 0.8 mA/cm<sup>2</sup> in DMSO for 300 s and measured at 0.4 V vs. Ag/AgCl (the same electrode is also presented in Figure 5.8). The sample is illuminated from the electrolyte-electrode interface side. The inset shows the transient response of the electrode at 500 nm, and the arrows indicate from which photocurrent values the IPCE is calculated.

It should be noted that our films show much less porosity and much lower specific surface area than the nanoporous TiO<sub>2</sub> electrodes in the studies mentioned above. Trapping at

$\text{Fe}_2\text{O}_3$  grain boundaries may play a role, but the crystalline size for these films is  $\sim 52$  nm (cf. Table 5.1) resulting in a  $\sim 3$  times smaller grain boundary area than for the 30 nm  $\text{TiO}_2$  particles in ref. [32]. While we cannot entirely rule out the possibility of interfacial electron trapping, we feel that a more appropriate explanation may be given in terms of photodoping. As discussed here, electron transport is the rate-limiting factor in these undoped  $\text{Fe}_2\text{O}_3$  photoanodes. At low light intensities, the photo-generated electrons accumulate and recombine with the holes before reaching the back contact. At high light intensities, however, the electronic conductivity is strongly enhanced by photodoping. This results in a faster photocurrent response, less recombination, and higher quantum yields (Figure 5.12). This explanation is consistent with the absence of photocurrent transients in more highly conducting Si-doped  $\text{Fe}_2\text{O}_3$  films made by spray pyrolysis [29].

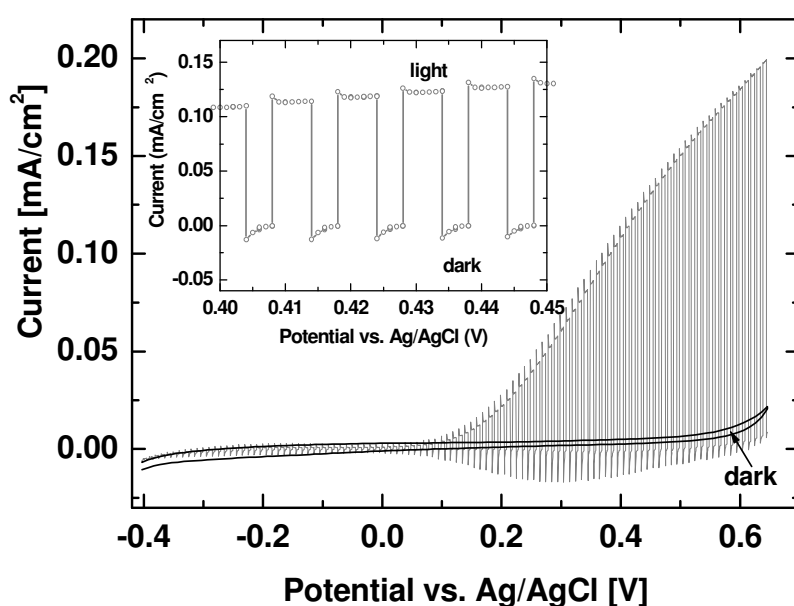


**Figure 5.12:** Chopped-light voltammograms of the same  $\text{Fe}_2\text{O}_3$  electrode as shown in Figures 5.8 and 5.10, measured under simulated AM1.5 sunlight ( $100 \text{ mW}/\text{cm}^2$ ) with a scan rate of  $1 \text{ mV}/\text{s}$  and using a shutter (6s on, 4s off). The sample is illuminated from the electrolyte side (EE). The inset shows the shape of the transients in some more detail.

## 5.4 Summary and conclusions

Electrodeposition followed by thermal oxidation (*EDOX*) is demonstrated to be a simple and effective technique to make hematite photoanodes with varying morphologies. After reaching a certain thickness, or at sufficiently high deposition currents ( $2 \text{ mA}/\text{cm}^2$ ), nano-sized needle-like features start to protrude from the oxidized films. These features may represent the onset of nanowire growth, although fully developed nanowires have not been observed in this study. A further increase of the deposition current to  $3 \text{ mA}/\text{cm}^2$  results in columns consisting of small irregular iron crystallites stacked on top of each other. In contrast, a compact dense film of spherical particles is formed after oxidation when a Si precursor is present in the electrolyte solution during the electrodeposition.

XRD analysis and Raman spectroscopy have shown that the prepared Fe<sub>2</sub>O<sub>3</sub> electrodes comprise mainly the  $\alpha$ -Fe<sub>2</sub>O<sub>3</sub> phase. The films grown at higher current densities have smaller crystallites and a preferred (110) orientation. Although the electron mobility is highest along this orientation, electron transport was found to limit the performance for all undoped films in this study.

Despite this limitation, it was possible to improve the performance by shifting the photocurrent onset potential towards more cathodic (negative) values. The origin of this shift is attributed to the high catalytic activity of the needle-like crystallites that form under the right growth conditions. In addition, a 30% improvement in photocurrent could be obtained by first growing a dense underlayer at lower current densities. This marked improvement suggests that the nature of the substrate has an important influence on the density of (micro)structural defects in the photoactive film. Finally, we found indications of photodoping in undoped Fe<sub>2</sub>O<sub>3</sub> films. This effect resulted in much higher photocurrents under AM1.5 illumination than would be expected based on IPCE data measured at low light intensities and should be taken into account when investigating undoped Fe<sub>2</sub>O<sub>3</sub> photoanodes.

## **5.5 Recommendations**

To further improve the photoresponse of the Fe<sub>2</sub>O<sub>3</sub> electrodes made by *EDOX*, it would be beneficial to have a morphology that more closely resembles a true nanowire array. Two possible strategies are proposed in order to reach this goal:

- ❖ Modifying the precursor electrolyte solution,

Additional additives can be added to the non-aqueous precursor solution in order to influence and control the growth mechanisms. For example, it has been shown that for ZnO films prepared by electrodeposition the presence of a polyvinylpyrrolidone (PVP) surfactant or tributyl-phosphine (TBP) has a strong effect on the grain size and surface morphology [33,34].

- ❖ Controlling the annealing parameters of the electrodeposited iron,

By annealing in air under a well-defined gas flow instead of under open air it may be possible to directly transform the deposited iron into Fe<sub>2</sub>O<sub>3</sub> nanorods. Chueh et al. [11] have shown that the gas flow around the substrate in an elongated tube furnace has a great influence on the type of morphology obtained. Specifically, they found that a dense network of nanowires perpendicular to the substrate is formed at relatively low gas flow, whereas poor nanowire surfaces are achieved at low gas flows or thinner iron layer.

The electrodeposition method has advantages over other processes because of its simplicity, low cost of the equipment, easy control over the deposition parameters, relative simplicity to scale up to larger areas, and the possibility to coat substrates with more complex shapes.

## References

- [1]. R. van de Krol, Y. Q. Liang, and J. Schoonman, *J. Mater. Chem.*, **18**, 2311 (2008).
- [2]. Solar irradiance data, ASTM-G173-03 (AM1.5, global tilt). (<http://rredc.nrel.gov/solar/spectra/am1.5/>). Last checked: 11 August 2010.
- [3]. J. H. Kennedy and J. Frese, *J. Electrochem. Soc.*, **125**, 709 (1978).
- [4]. T. Lindgren, H.L. Wang, N. Beermann, L. Vayssieres, A. Hagfeldt, and S. E. Lindquist, *Solar Energy Mater. Solar Cells*, **71**, 231 (2002).
- [5]. A. Kay, I. Cesar, and M. Grätzel, *J. Am. Chem. Soc.*, **128**, 15714 (2006).
- [6]. I. Cesar, K. Sivula, A. Kay, R. Zboril, and M. Grätzel, *J. Phys. Chem. C*, **113**, 772 (2008).
- [7]. F. Le Formal, M. Grätzel, and K. Sivula, *Adv. Funct. Mater.*, **20**, 1099 (2010).
- [8]. N. Beermann, L. Vayssieres, S. E. Lindquist, and A. Hagfeldt, *J. Electrochem. Soc.*, **147**, 2456 (2000).
- [9]. U. Björkstén, J. Moser, and M. Grätzel, *Chem. Mater.*, **6**, 858 (1994).
- [10]. L. Vayssieres, C. Sathe, S. M. Butorin, D. K. Shuh, J. Nordgren, and J. Guo, *Adv. Mater.*, **17**, 2320 (2005).
- [11]. Y. Chueh, M.-W. Lai, J.-Q. Liang, L.-J. Chou, and Z. L. Wang, *Adv. Funct. Mater.*, **16**, 2243 (2006).
- [12]. T. Yu, Y. Zhu, X. Xu, K.-S. Yeong, Z. Shen, P. Chen, C. T. L. Lim, J. T.-L. Thong, and C.-H. Sow, *Small*, **2**, 80 (2006).
- [13]. Olthof, T. J. "Iron oxide nanostructures for hydrogen production", B.Sc thesis, 2007, Delft University of Technology.
- [14]. W. B. Ingler, Jr. and S. U. M. Khan, *Int. J. Hydrogen Energy*, **30**, 821 (2005).
- [15]. Y.-T. Qian, C.-M. Niu, C. Hannigan, S. Yang, K. Dwight, and A. Wold, *J. Solid State Chem.*, **92**, 208 (1991).
- [16]. C. Jorand Sartorette, M. Ulmann, B. D. Alexander, J. Augustynski, and A. Weidenkaff, *Chem. Phys. Lett.*, **376**, 194 (2003).
- [17]. S. Yoshimura, S. Yoshihara, T. Shirakashi, and E. Sato, *Electrochim. Acta*, **39**, 589 (1994).
- [18]. L. Xu, Y. Guo, Q. Liao, J. Zhang, and D. Xu, *J. Phys. Chem. B*, **109**, 13519 (2005).
- [19]. E. Michaelis, D. Wöhrle, J. Rathousky, and M. Wark, *Thin Solid Films*, **497**, 163 (2006).
- [20]. I. Cesar, A. Kay, J. A. Gonzalez Martinez, and M. Grätzel, *J. Am. Chem. Soc.*, **128**, 4582 (2006).
- [21]. K. M. Rosso, D. M. A. Smith, and M. Dupuis, *J. Chem. Phys.*, **118**, 6455 (2003).
- [22]. T. Nakau, *J. Phys. Soc. Jpn.*, **15**, 727 (1960).
- [23]. D. Bersani, P. P. Lottici, and A. Montenero, *J. Raman Spectrosc.*, **30**, 355 (1999).
- [24]. L. J. Oblonsky, S. Virtanen, V. Schroeder, and T. M. Devine, *J. Electrochem. Soc.*, **144**, 1604 (1997).
- [25]. D. L. A. de Faria, S. V. Silva, and M. T. de Oliveira, *J. Raman Spectrosc.*, **28**, 873 (1997).
- [26]. N. Uekawa and K. Kaneko, *J. Phys. Chem. B*, **102**, 8719 (1998).
- [27]. A. Duret and M. Grätzel, *J. Phys. Chem. B*, **109**, 17184 (2005).
- [28]. S.E. Lindquist, B. Finnstrom, and L. Tegner, *J. Electrochem. Soc.*, **130**, 351 (1983).
- [29]. Y. Q. Liang, C. S. Enache, and R. van de Krol, *Int. J. of Photoenergy*, **2008**, 1 (2008).
- [30]. H. Kato, K. Asakura, and A. Kudo, *J. Am. Chem. Soc.*, **125**, 3082 (2003).
- [31]. J. P. Nicholson, *J. Electrochem. Soc.*, **152**, C795 (2005).
- [32]. P. E. de Jongh and D. Vanmaekelbergh, *J. of Phys. Chem. B*, **101**, 2716 (1997).
- [33]. Z. Chen, Y. Tang, L. Zhang, and L. Luo, *Electrochim. Acta*, **51**, 5870 (2006).
- [34]. R. Jayakrishnan and G. Hodes, *Thin Solid Films*, **440**, 19 (2003).

# *Summary*

For centuries, mankind has mostly used fossil fuels, i.e., natural gas, coal, and oil for its energy needs. With the fast rise of the world population and the rising standards of living in the developing countries, the amount of energy the world is going to need in the coming decades will grow enormously. Due to environmental concerns and the need to secure the energy supply, more actions have to be taken in the development and implementation of cleaner technologies, based on solar, wind, geothermal power, and biomass, combined with storage technologies such as batteries and hydrogen. Moreover, to fulfill the future global energy demand, all of the available energy sources will be needed.

Despite the fact that solar energy is abundant, clean, and widely available, only a small percentage of this energy is utilized through conversion to electricity by photovoltaic systems. This is partly due to the need for smart technological inventions to make the alternative energy cost-effective and competitive with the conventional energy production. The Netherlands intends to increase the percentage of energy produced by sustainable sources from 4% nowadays to 20% in 2020.

When considering sustainable energy production, also energy storage has to be investigated, since especially solar and wind energy are not continuous. In the chain of solar energy production and the need for energy storage, hydrogen is a promising storage candidate due to its high gravimetric energy density and its nonpollutive combustion product, water. Nowadays, hydrogen can be produced by a number of processes, such as electrolysis of water, steam reforming of natural gas, and biomass conversion, which directly or indirectly release large amounts of carbon dioxide into the atmosphere. An elegant alternative will be the use of solar energy for the electrolysis of water in a photoelectrochemical cell. Direct photoelectrolysis has the potential to be economically more attractive than coupled systems of photovoltaic cells and electrolyzers. Additional information regarding this subject can be found in Chapter 1, as well as the necessary requirements for the photoelectrodes.

In this thesis three different metal oxides,  $\text{TiO}_2$ ,  $\text{InVO}_4$ , and  $\text{Fe}_2\text{O}_3$  are investigated as photoanodes for water splitting applications. The aim of the research presented in this thesis is two-fold. First, the use of low-cost deposition techniques for the preparation of efficient thin-film photoanodes is explored. Special attention is given to the possibility to introduce dopants in a controlled manner. Second, the influence of the presence of ionic point defects on the photoelectrochemical performance of the materials is investigated.

Titanium dioxide has long been considered as one of the most promising semiconductors for photoelectrolysis applications due to its low cost, non-toxicity, and excellent stability against corrosion. However, because of its wide bandgap (3.2 eV for anatase) the utilization of  $\text{TiO}_2$  typically remains confined to the UV light region, which constitutes only a small fraction (2-3%) of the solar radiation reaching the earth surface. Therefore, shifting its photoresponse into the visible range of the solar spectrum would enhance its potential for chemical solar energy conversion. Attempts to achieve this performance are typically focused on adding dopants.

In Chapter 2 Fe- and C-doped  $\text{TiO}_2$  thin films have been investigated. Pulsed spray pyrolysis is employed to deposit high quality dense films. The prepared films are crystalline with an anatase structure and a post-deposition anneal does not change the morphology. For the Fe-doped  $\text{TiO}_2$  a small sub-bandgap photoresponse is observed, which is attributed to the presence of additional states located just above the valence band. Little or no visible-light photoresponse is observed for the C-doped anatase  $\text{TiO}_2$ , which is attributed to a (too) low carbon content. However, the photocurrent at  $h\nu > E_g$  is significantly larger for C-doped  $\text{TiO}_2$  than for undoped  $\text{TiO}_2$ . The strong enhancement of UV photoresponse is most likely caused by a change in the electronic structure of the material due to the presence of carbon and/or related defects. Photoluminescence measurements suggest that the defects present in oxidized carbon-doped anatase resemble those present in undoped, partially reduced  $\text{TiO}_2$ . Although the exact nature of these defects is unknown, impedance measurements reveal a donor density of  $10^{19}$ - $10^{20}$   $\text{cm}^{-3}$  in C-doped  $\text{TiO}_2$ . The high UV photoresponse is rather surprising for such a high donor density, and illustrates the intriguing, but still poorly understood properties of anion dopants.

From the synthesis point of view, the preparation of carbon-doped  $\text{TiO}_2$  photoanodes was found to be challenging. A more simple approach is to prepare C-doped powders by solid-state reactions at high temperatures. Such a system can serve as a convenient screening method for selecting suitable anion dopants by analyzing the evolved gases, even if the efficiencies are very low.

In Chapter 3 the focus is on the addition of carbon as dopant to anatase  $\text{TiO}_2$  by a post-deposition thermal treatment in a hexane-rich environment. Both thin films prepared by spray pyrolysis and mesoporous  $\text{TiO}_2$  photoelectrodes prepared by doctor-blading a paste of  $\text{TiO}_2$  nanoparticles are investigated. It is found that the carbon is mainly located at the surface of the  $\text{TiO}_2$ . While it causes a black coloring of the mesoporous  $\text{TiO}_2$  film, it does not enhance the photocatalytic activity in the visible part of the spectrum. Only a small amount of carbon (<0.1 at%) diffuses into the bulk of the material where it causes a small shift (0.05-0.1 eV) of the absorption edge towards higher wavelengths.

An intriguing observation is that the presence of carbon in anatase  $\text{TiO}_2$  increases the anatase-to-rutile transformation temperature from 600 °C to beyond 800 °C. Based on the

temperature at which this transformation occurs, it has been concluded that films sprayed under a CO<sub>2</sub> atmosphere contain significantly more carbon compared to the TiO<sub>2</sub> samples subjected to the post anneal hexane treatment, although in both cases the amount of carbon incorporated into the TiO<sub>2</sub> films is not sufficient to generate a visible light response. To increase the concentration of C in TiO<sub>2</sub> the oxidation of TiC films may be a more promising route.

Although the amount of C as dopant present in TiO<sub>2</sub> is not sufficient to generate a significant visible light response, the rather large increase in the anatase-to-rutile phase transformation temperature enables one to retain the anatase structure during high-temperature heat treatments. Such treatments are sometimes employed to improve the contact between small particles, and this can now be achieved while avoiding the transformation of anatase to the less photo-active rutile phase.

In Chapter 4 the ternary oxide InVO<sub>4</sub> is investigated as photoelectrode, since InVO<sub>4</sub> is one of the few ternary oxides that shows hydrogen evolution from pure water under visible light illumination. Spray pyrolysis is explored as a novel method to produce thin films of nearly phase-pure orthorhombic InVO<sub>4</sub> at low temperatures. In contrast, most of the complex oxide photocatalyst powders described in the literature are prepared using high-temperature solid state reactions.

Optical absorption analysis shows that InVO<sub>4</sub> has an indirect bandgap of ~3.2 eV with a sub-bandgap absorption at 2.5 eV, which is attributed to the presence of deep donors in the space charge region of the material. The InVO<sub>4</sub> photoresponse is mainly in the UV region of the solar spectrum and the photon-to-current conversion efficiency (IPCE) is less than 1%. The amount of visible light absorption scales with the total surface area, which explains why InVO<sub>4</sub> powders absorb much more light than compact films. Detailed electrochemical impedance analysis of InVO<sub>4</sub> thin-film photoelectrodes shows that the high concentration of deep donors causes a very narrow space charge region (few nm) in which the photo-generated electron and holes are separated. Ni and Cu dopants added to the InVO<sub>4</sub> films do not improve the response and seem rather to act as recombination centers than as acceptor-type dopants. A dielectric constant of 50 was calculated for the first time and a flatband potential of -0.04 eV vs. RHE was determined, which confirms that the InVO<sub>4</sub> is able to evolve H<sub>2</sub>.

The main bottleneck of the thin film InVO<sub>4</sub> compared to powders appears to be the high concentration of (deep) donors and a concomitant small depletion layer width. Moreover, accurate control over the stoichiometry of the metal ions for InVO<sub>4</sub> remains challenging compared to simple binary oxides. This is an important and general aspect that needs to be considered when designing photoelectrodes based on ternary and more complex metal oxides.

Iron oxide (Fe<sub>2</sub>O<sub>3</sub>) electrodes are the subject of Chapter 5. Hematite Fe<sub>2</sub>O<sub>3</sub> has potential as a photoanode for water photoelectrolysis. It is stable in aqueous solutions with pH >3 and it has a near-optimal bandgap of 2.1 eV that enables up to 32% sunlight absorption. It is also an abundant and inexpensive semiconductor. However, certain intrinsic properties of Fe<sub>2</sub>O<sub>3</sub> limit its performance as a photoelectrode. It shows a poor conductivity, which often leads to a high recombination rate, the energy level of the conduction band is too low for hydrogen evolution, it has slow kinetics for water oxidation, and a modest optical absorption coefficient.

The main goal of the research in this chapter is on the preparation of Fe<sub>2</sub>O<sub>3</sub> nanorods perpendicular to the substrate. Such a morphology could improve the efficiency of Fe<sub>2</sub>O<sub>3</sub>

photoanodes by decreasing the diffusion path length of the photo-generated holes. To achieve this, electrodeposition of Fe followed by thermal oxidation (EDOX) is explored as a new method to obtain these photoelectrodes efficiently in a short time and with the possibility to control the morphology. It is observed that after reaching a certain thickness or at a sufficiently high deposition current ( $2 \text{ mA/cm}^2$ ) nano-sized needle-like features start to form. A further increase of the deposition current to  $3 \text{ mA/cm}^2$  results in a columnar growth consisting of small irregular crystallites stacked on top of each other. In contrast, it has been observed that when a Si precursor is present in the electrolyte solution during the electrodeposition, compact dense  $\text{Fe}_2\text{O}_3$  films consisting of spherical particles are formed after the post-deposition oxidation. XRD analysis and Raman spectroscopy show that the  $\text{Fe}_2\text{O}_3$  films mainly consist of the  $\alpha$ - $\text{Fe}_2\text{O}_3$  hematite phase.

An important advantage of the EDOX method is that low-cost equipment can be used. Moreover, the direct thermal oxidation of electrodeposited Fe avoids the formation of undesired intermediate phases, such as  $\text{FeOOH}$ . Finally, the electrodeposition process takes place in a non-aqueous solvent, which allows the use of certain dopant precursors (e.g.  $\text{TiCl}_4$ ) that cannot be used in aqueous systems. This is an important advantage of this approach compared to other efforts in the literature.

Although the EDOX method has been successfully demonstrated, an important remaining challenge is to improve control over the morphology and the doping density. Further improvements of the morphology may be possible by adding additives to the electrolyte solution, or by controlling the process parameters during oxidation of the electrodeposited iron.

In conclusion, it has been demonstrated in this thesis that high-quality metal oxides can be prepared by low-cost techniques. Concomitantly, the impact of the ionic point defects on the performance of those photoanode materials is addressed and important material properties are determined. The attempts to enhance the visible-light response does not always result in higher efficiencies, due to low dopant concentrations in  $\text{TiO}_2$  films, poor electronic properties of  $\text{InVO}_4$  thin films, and morphology challenges for  $\text{Fe}_2\text{O}_3$  to overcome its limitation as photoanode material. Nevertheless, important properties of the thin film photoanodes have been investigated and determined.

No binary oxide solely can split water with a reasonable efficiency unless a tandem cell approach with suitable oxides is used. In principle, a lot can be gained by directing future research efforts towards ternary and even more complex metal oxides. In this case, however, the control over the stoichiometry of the metal ions remains challenging compared to simple binary oxides as has been demonstrated by the results on  $\text{InVO}_4$ .

While for some of the alternative energy sources technological breakthroughs have been achieved and new technologies are developed, for the hydrogen economy and in particular for the photoelectrochemical water splitting with metal oxides, more research is needed in developing low-cost techniques to make highly structured electrodes with large aspect ratios, to develop synthesis and/or doping strategies to suppress undesired defects present in the ternary oxides with non-stoichiometric metal:metal ratios, and not the least, in finding new and improving existing materials. When these challenges are met, photoelectrochemical water splitting may emerge as an economically viable and truly renewable pathway towards clean hydrogen.

# *Samenvatting*

Eeuwenlang is de mensheid voor de energievoorziening afhankelijk geweest van fossiele brandstoffen, vooral olie, gas, en kolen. Door de snelle groei van de wereldbevolking en de stijgende levensstandaard in de zich ontwikkelende landen stijgt de energiebehoefte van de wereld nog steeds enorm. Vanwege zorgen om het milieu en de noodzaak om de energievoorziening zeker te stellen, is het noodzakelijk om een grotere inspanning te doen met betrekking tot het ontwikkelen en toepassen van schone energievoorzieningen gebaseerd op zon, wind, geothermale energie, en biomassa. Deze technologieën zullen gecombineerd moeten worden met opslagmethoden, zoals batterijen en waterstof. Om de wereldenergievoorziening in de toekomst zeker te stellen, zullen alle beschikbare energiebronnen benut moeten worden.

Hoewel zonne-energie schoon en in overvloed beschikbaar is, wordt toch slechts een klein gedeelte van deze energie benut door middel van omzetting in elektriciteit met behulp van fotonvoltaïsche systemen. Dit is deels vanwege de noodzaak om deze alternatieve energietechnologie kosten-efficiënt en concurrerend te maken met conventionele energiebronnen. In Nederland is de doelstelling om het aandeel van duurzame energie in de totale energiemix te laten stijgen van de huidige 4% naar 20% in 2020.

Wanneer de duurzame productie van energie wordt overwogen, is het belangrijk dat ook de energieopslag wordt bekeken, vooral voor wind en zonne-energie, aangezien deze bronnen niet continu zijn. In de keten van zonne-energie productie en de opslag hiervan, is waterstof een veelbelovende optie door de hoge gravimetrische energiedichtheid en het niet-vervuilende verbrandingsproduct water. Tegenwoordig kan waterstof op verschillende manieren geproduceerd worden, onder meer door elektrolyse van water, steam reforming van aardgas, en biomassa conversie. Deze laatste twee processen produceren echter grote hoeveelheden kooldioxide welke vervolgens in de atmosfeer terecht komen. Een elegant alternatief is het gebruik van zonne energie voor de elektrolyse van water in een fotoelektrochemische cel. Directe fotoelektrolyse heeft het potentieel economisch meer aantrekkelijk te zijn dan

gekoppelde systemen van fotovoltaïsche cellen en elektrolyse cellen. Aanvullende informatie over dit onderwerp kan gevonden worden in Hoofdstuk 1, waar ook de vereisten voor praktische fotoelektrodes beschreven staan.

In dit proefschrift worden drie verschillende metaaloxides,  $\text{TiO}_2$ ,  $\text{InVO}_4$  en  $\text{Fe}_2\text{O}_3$ , onderzocht als fotoanodes voor het splitsen van water. Het doel van het onderzoek in dit proefschrift is tweeledig. Ten eerste wordt de toepassing van goedkope depositiemethoden voor de bereiding van efficiënte dunne-laag fotoanodes onderzocht. Speciale aandacht wordt hierbij gegeven aan de mogelijkheid om doteringen (toevoegingen) op een gecontroleerde manier toe te voegen. Ten tweede is het effect van de aanwezigheid van ionogene defecten (roosterfouten) op het elektrochemische gedrag van de materialen onderzocht.

Titaniumdioxide wordt al lange tijd gezien als één van de meest veelbelovende halfgeleiders voor de fotoelektrolyse toepassing vanwege de lage kosten, verwaarloosbare toxiciteit en de uitstekende bestendigheid tegen corrosie. Echter, vanwege de grote bandgap (3.2 eV voor anatasa) kan  $\text{TiO}_2$  uitsluitend het licht in het UV gebied benutten, wat maar een klein gedeelte (2-3 %) omvat van alle zonnestraling, die het aardoppervlak bereikt. Vanwege deze reden zou het zeer aantrekkelijk zijn om de fotorespons te verschuiven naar het zichtbare licht deel van het zonnespectrum. Hierdoor zou het potentieel van  $\text{TiO}_2$  voor de chemische omzetting van zonlicht enorm vergroot worden. Onderzoekspogingen om dit doel te bereiken richtten zich meestal op het toepassen van doteringen als fotoactieve centra, die gevoelig zijn voor zichtbaar licht.

In hoofdstukken 2 en 3 worden koolstof- en ijzer- gedoteerde  $\text{TiO}_2$  dunne lagen onderzocht. Gepulseerde spray pyrolyse is gebruikt om hoge kwaliteit dichte lagen te deponeren. De gemaakte lagen zijn kristallijn met een anatasa structuur en een hitte behandeling (annealing) na de bereiding verandert de morfologie niet. Voor het Fe-gedoteerde  $\text{TiO}_2$  is een kleinere sub-bandgap fotorespons waargenomen, welke toegeschreven kan worden aan de aanwezigheid van additionele energietoestanden net boven de valentieband. Geen of bijna geen zichtbaar-licht fotorespons is waargenomen voor de C-gedoteerde anatasa  $\text{TiO}_2$  lagen, hetgeen toegeschreven kan worden aan een (te) laag koolstof gehalte. Echter, de fotostroom bij  $h\nu > E_g$  is significant groter voor C-gedoteerd  $\text{TiO}_2$  dan voor ongedoteerd  $\text{TiO}_2$ . De sterk toegenomen UV fotorespons wordt vrijwel zeker veroorzaakt door een verandering in de elektronische structuur van het materiaal door de aanwezigheid van koolstof en/of gerelateerde defecten. Fotoluminescentie metingen suggereren dat defecten aanwezig in geoxideerd koolstof-gedoteerd anatasa lijken op die welke aanwezig zijn in niet-gedoteerd partieel gereduceerd  $\text{TiO}_2$ . Hoewel de precieze toestand van deze defecten nog onbekend is, laten impedantie metingen een donor dichtheid zien van  $10^{19}$ - $10^{20}$   $\text{cm}^{-3}$  in C-gedoteerd  $\text{TiO}_2$ . De hogere UV fotorespons is verrassend voor een dergelijke hoge donor dichtheid en dit geeft de intrigerende, maar nog steeds slecht begrepen eigenschappen van anion doteringen aan.

De bereiding van koolstof-gedoteerde  $\text{TiO}_2$  fotoanodes bleek zeer uitdagend te zijn qua synthese. Een eenvoudiger benadering is om koolstof-gedoteerde poeders te bereiden door middel van vaste-stof reacties bij hoge temperatuur. Een dergelijk systeem kan dienen als een eenvoudige screening methode om geschikte anion doteringen te selecteren door de vrijkomende gassen te analyseren, ondanks het feit dat de efficiënties laag zijn.

In Hoofdstuk 3 ligt de nadruk op het toevoegen van koolstof als doteringselement aan anataas  $\text{TiO}_2$  met behulp van een post-depositie thermische behandeling in een hexaan-rijke omgeving. Dit is onderzocht voor zowel dunne films gedeponeerd met behulp van spray-pyrolyse als voor mesoporeuze  $\text{TiO}_2$  fotoanodes bereid door middel van ‘doctor-blading’ van een suspensie van  $\text{TiO}_2$  nanodeeltjes. Gevonden is dat de koolstof zich vooral aan het oppervlak van de  $\text{TiO}_2$  deeltjes bevindt. Hoewel het een zwarte verkleuring van de mesoporeuze  $\text{TiO}_2$  film veroorzaakt, geeft het geen verbetering in de fotokatalytische activiteit in het zichtbare gebied van het spectrum. Slechts een klein gedeelte van de koolstof (<0.1 at%) diffundeert in de bulk van het materiaal, waar het een kleine verschuiving (0.05-0.1 eV) veroorzaakt van de absorptie edge in de richting van langere golflengtes.

Een intrigerende waarneming is dat de aanwezigheid van koolstof in anataas  $\text{TiO}_2$  de temperatuur waarbij de anataas naar rutiel overgang plaats vindt verhoogt van 600 °C tot boven de 800 °C. Gebaseerd op de temperatuur, waarbij deze overgang plaatsvindt, kan geconcludeerd worden dat films gesprayd onder een  $\text{CO}_2$  atmosfeer significant meer koolstof bevatten, dan  $\text{TiO}_2$  monsters welke een post-annealing hexaan behandeling hebben ondergaan. In beide gevallen is de aanwezige hoeveelheid koolstof echter niet genoeg om een zichtbaar-licht fotorespons te geven. Om de hoeveelheid koolstof in  $\text{TiO}_2$  te verhogen is mogelijkwijs de oxidatie van TiC films een veelbelovende route.

Hoewel de hoeveelheid koolstof dotering aanwezig in  $\text{TiO}_2$  onvoldoende is om een noemenswaardige zichtbaar-licht respons te geven, maakt de grote toename in de temperatuur van de anataas naar rutiel overgang het wel mogelijk om de anataas structuur te behouden tijdens hoge-temperatuur behandelingen. Zulke behandelingen worden gebruikt om het contact tussen kleine deeltjes te verbeteren en dit kan nu bereikt worden zonder dat de ongewenste overgang van anataas naar de minder foto-actieve rutiel fase plaatsvindt.

In Hoofdstuk 4 is het ternaire oxide  $\text{InVO}_4$  onderzocht als fotoelektrode.  $\text{InVO}_4$  is een interessant materiaal omdat het een van de weinige ternaire oxides is, die waterstof vrij laten komen vanuit zuiver water tijdens belichting met zichtbaar licht. Spray pyrolyse is onderzocht als een nieuwe methode om dunne lagen  $\text{InVO}_4$  met een orthorhombische kristalstructuur te deponeren bij lage temperatuur. Dit is in tegenstelling tot de in de literatuur aangegeven hoge temperaturen, die nodig zijn voor het bereiden van complexe metaaloxide fotokatalysatoren. Optische absorptie analyse laat zien dat  $\text{InVO}_4$  een indirecte bandgap heeft van ~3.2 eV met een sub-bandgap absorptie bij 2.5 eV, welke wordt toegeschreven aan de aanwezigheid van diepe donoren in de ruimteladingslaag van het materiaal. De fotorespons van  $\text{InVO}_4$  ligt vooral in het UV gebied van het zonnenspectrum en de foton-naar-stroom conversie efficiëntie (IPCE) is minder dan 1%. De hoeveelheid zichtbaar-licht absorptie schaalt met het totale oppervlak, hetgeen verklaart waarom  $\text{InVO}_4$  poeders veel meer licht absorberen dan compacte dunne lagen. Een uitgebreide elektrochemische impedantie analyse van dunnelaag  $\text{InVO}_4$  fotoelektrodes laat zien dat de hoge concentratie aan diepe donoren een zeer smal ruimteladingsgebied (enkele nm) veroorzaakt waarin de foto-gegenereerde elektronen en gaten van elkaar gescheiden kunnen worden. Ni en Cu doteringen toegevoegd aan de  $\text{InVO}_4$  films verbeteren de respons niet en schijnen eerder te werken als recombinatiecentra in plaats van als acceptor-type doteringen. In dit hoofdstuk zijn voor de eerste keer in de literatuur de dielectrische constante en vlakkebandpotentialiaal van  $\text{InVO}_4$  bepaald, waarvoor waarden van

resp. 50 en  $-0.04$  V vs. RHE zijn gevonden. De negatieve waarde van de vlakkebandpotentialiaal bevestigt dat  $\text{InVO}_4$  waterstof kan produceren.

De grootste beperking van dunne-laag  $\text{InVO}_4$  films, vergeleken met poeders, lijkt de hoge concentratie van (diepe) donoren te zijn en een daarmee verband houdende smalle depletie laagbreedte. Daarnaast blijft een nauwkeurige beheersing van de stoichiometrie van de metaalionen in  $\text{InVO}_4$  uitdagend vergeleken met eenvoudige binaire oxides. Dit is een belangrijk en fundamenteel aspect, wanneer fotoelektrodes worden ontwikkeld op basis van ternaire of meer complexe oxiden.

Hoofdstuk 5 bespreekt ijzeroxide ( $\text{Fe}_2\text{O}_3$ ) elektrodes. Hematiet ( $\alpha\text{-Fe}_2\text{O}_3$ ) is een veelbelovend materiaal als fotoanode voor de fotoelectrolyse van water. Het is stabiel in waterig milieu met een  $\text{pH} > 3$  en heeft een vrijwel optimale bandgap van 2.1 eV, hetgeen absorptie van 32% van het invallende zonlicht mogelijk maakt. Het is een ruim beschikbaar materiaal en een goedkope halfgeleider. Het heeft echter wel enige intrinsieke eigenschappen, die de toepassing als fotoanode beperken. De elektronische geleiding is slecht, wat vaak leidt tot een hoge recombinatie snelheid, het energieniveau van de geleidingsband is te laag om waterstof te kunnen produceren, de katalytische activiteit voor water oxidatie is laag, en de optische absorptiecoëfficiënt is niet hoog.

Het hoofddoel van het onderzoek in dit hoofdstuk is de bereiding van  $\text{Fe}_2\text{O}_3$  nano-staafjes loodrecht op het onderliggende dragermateriaal (substraat). Een dergelijke morfologie kan de efficiëntie van  $\text{Fe}_2\text{O}_3$  fotoanodes verbeteren door de diffusie weglengte van de door de fotonen gegenereerde gaten te verkleinen. Om dit te bereiken is ijzeroxide gemaakt door middel van elektrodepositie van metallisch ijzer, gevolgd door thermische oxidatie – de zgn. ‘EDOX’ methode. Dit is een nieuwe methode om deze fotoelektrodes efficiënt en snel te verkrijgen en daarbij de morfologie te beheersen. Waargenomen is dat nano-naaldvormige structuren gevormd worden na het bereiken van een bepaalde laagdikte, of bij een voldoende hoge stroomdichtheid tijdens de elektrodepositie van Fe ( $2 \text{ mA/cm}^2$ ). Een verdere toename in de depositiestroom tot  $3 \text{ mA/cm}^2$  resulteert in een kolomvormige groei van kleine op elkaar gestapelde onregelmatige kristallen. Echter, wanneer een Si precursor aanwezig is in de elektrolyt oplossing tijdens de elektrodepositie, dan worden compacte dichte  $\text{Fe}_2\text{O}_3$  laagjes gevormd, die resulteren in bolvormige deeltjes na de post-depositie oxidatie. XRD analyse en Raman spectroscopie bevestigen dat de  $\text{Fe}_2\text{O}_3$  laagjes vooral bestaan uit de gewenste  $\alpha\text{-Fe}_2\text{O}_3$  hematiet fase.

Een belangrijk voordeel van de EDOX methode is dat goedkope apparatuur gebruikt kan worden. Daarnaast voorkomt de thermische oxidatie van het door elektrodepositie afgezette Fe dat er ongewenste tussenfasen worden gevormd zoals  $\text{FeOOH}$ . Ook vindt de elektrodepositie plaats in een niet-waterig oplosmiddel, wat het mogelijk maakt bepaalde dotingselementen (zoals  $\text{TiCl}_4$ ) toe te voegen, die niet in waterige systemen toegepast kunnen worden. Dit is een belangrijk voordeel van deze benadering ten opzichte van andere in de literatuur beschreven methoden.

Hoewel het gebruik van de EDOX methode succesvol is aangetoond, is het nog steeds een belangrijke uitdaging om de morfologie en de donordichtheid te beheersen. Verdere verbeteringen van de morfologie kunnen mogelijk zijn door de toevoeging van additieven aan de elektrolytoplossing, of door de procesparameters beter te beheersen tijdens de oxidatie van het door elektrodepositie afgezette ijzer.

Samenvattend, in dit proefschrift wordt aangetoond dat het mogelijk is om hoge-kwaliteit metaaloxides te bereiden met goedkope technieken. Het effect van ionogene puntfouten op de fotoelektrochemische eigenschappen van fotoanode materialen is onderzocht en belangrijke materiaaleigenschappen zijn bepaald. De pogingen om de zichtbaar-licht respons te verbeteren resulteren niet altijd in hogere efficiënties. Dit wordt veroorzaakt door een te lage doperingsconcentratie in  $\text{TiO}_2$  lagen, slechte elektrische eigenschappen van  $\text{InVO}_4$  films en door morfologie uitdagingen voor  $\text{Fe}_2\text{O}_3$ , welke overwonnen zullen moeten worden om deze materialen geschikt te maken als fotoanode. Desalniettemin zijn er belangrijke nieuwe inzichten verkregen in de eigenschappen van dunne laag metaaloxide fotoanodes.

Geen enkel binair oxide is zelfstandig in staat water te splitsen met een redelijke efficiëntie, tenzij een tandem cel benadering met geschikte oxides wordt toegepast. In principe is er veel winst te behalen door toekomstige onderzoeksinspanningen te richten op ternaire of complexere metaaloxides. Hiervoor is echter wel de beheersing van de stoichiometrie van de metaaloxides zeer uitdagend, vergeleken met binaire oxides, zoals in dit proefschrift is aangetoond voor  $\text{InVO}_4$ .

Hoewel voor sommige alternatieve energiebronnen technologische doorbraken behaald zijn en nieuwe technologieën zijn ontwikkeld, is dit nog niet het geval voor de waterstofeconomie en in het bijzonder voor de fotoelektrochemische watersplitsing met metaaloxides. Meer onderzoek is nodig om goedkope methoden te ontwikkelen om hoog-structureerde elektrodes te maken met een grote aspect-ratio en om synthese en/of doperingsstrategieën te ontwikkelen. Hierbij moet de vorming van ongewenste defecten worden voorkomen, die vaak aanwezig zijn in ternaire oxides met niet stoichiometrische metaal-metaal verhoudingen. Bovenal is het noodzakelijk dat nieuwe materialen ontwikkeld worden en de bestaande materialen verbeterd worden. Zodra deze uitdagingen zijn bereikt, kan fotoelektrochemisch water splitsen zich ontwikkelen tot een economisch aantrekkelijke methode en als een daadwerkelijk duurzame route om schoon waterstof te produceren.



# Acknowledgments

There are many people who, in one way or another, have contributed to the completion of this thesis. I am indebted to many of you whom I met during the years and it is impossible to name all of you. I would like to express my gratitude to all of you who have touched my life!

First, I want to thank my promotor Prof. Dr. Joop Schoonman and my supervisor Dr. ir. Roel van de Krol for giving me the opportunity to work on this challenging subject. Thank you for your confidence in my abilities. I appreciate our interesting discussions, which helped me to see the things from a different perspective and from a more global point of view. Roel, thank you for your guidance, support, availability, and optimism that you have shown during the years. My knowledge and expertise benefited greatly from our discussions. This thesis would not have been in the present form without your contribution. I also appreciated the inspiring and stimulating scientific discussions and suggestions of Dr. Albert Goossens. Your input is gratefully appreciated.

Many thanks to Dr. H. Donker for the valuable discussions and assistance with the photoluminescence experiments, and Dr. Kay Cesar (EPFL, Lausanne, Switzerland) for the interesting scientific discussions and the SEM images. Special thanks to Dr. Tom Savenije and Dr. Annemarie Huijser for their guidance with and facilitating the use of the UV-VIS spectrophotometer. My appreciation also goes to M. Bus for help with the AFM analysis. I thank Ton van de Plas and Ben Meester for their suggestions and help with fixing the technical problems in the lab.

Not the least, many thanks for the financial support that was provided by the Delft Institute for Sustainable Energy under the Sustainable Hydrogen program, which made these investigations possible.

I am very much indebted to Dr. Carolien Huisman who was a great supervisor during my final M.Sc. project at Delft University and who encouraged me to pursue a doctorate in the Netherlands. Thank you for your friendship and the trust that you have always shown. Sunt bucuroasă că ne-am cunoscut și împrietenit.

I would like to show my gratitude towards the professors I had during my study at the “Transilvania University” in Romania for their commitment and teaching enthusiasm, for their availability as well as the nice trips and time in the Netherlands.

I am thankful to Astrid Barrow and Marian de Bruijn, and later Els and Elly for their help and support in administrative and other more personal issues. Special thanks to Heleen and Caroline for the great support with the final administrative issues of the thesis.

My appreciations go to the great roommates I had over the years: Barbara, Marius and Kay (my two energetic colleagues) and later Ruben, Hans, Yongqi, and Yen for their availability to discuss unexpected results, their support on a personal level, and nice working environment. You have been more than colleagues to me!

My gratitude extends to all the other colleagues: PhD, post doc, master students, and students I met during the years for providing a friendly and “open discussion” working environment. Dan, Frederique, Nitte, Frans, Liesbeth, Eduard not only for the interesting XRD discussions, batteries, and CVD related issues. Alexandru thank you for the nice collaboration during your time in Delft. David, Martijn, Joep, Wouter, Isabelle, .... thanks for your enthusiasm, even with the unexpected challenges in the laboratory, and cooperation.

Furthermore, I want to thank all my friends (Romanian or other nationalities) from Delft and all over the world for the nice time we had together. I cannot mention everyone here but I thank you all, and I hope we will remain friends despite the geographical distance that separate us. Special thanks to Florence, Andrei, Gabi, Diana, Marius, Oana, Elena, Viorel, Emilia, Christian, Lin, Delia, Camelia, Annemarie, Bogdan,....I always enjoy/ed the great time spent in your company. I am lucky to have met you!

Special acknowledgments I address to Ankelien Kadijk, Tommy Jessurun, and Elisabeth van der Poel for their help, patience and very useful tips. I really learn a lot from you and I am grateful for all you have done for me!

Mulțumiri speciale sunt adresate familiei mele: părinților Ionica și Mircea care mi-au oferit libertatea sa aleg studiile dorite și au încurajat educația, deasemenea unchiului și mătușei Viorel și Maricica Turcu care m-au sprijinit la momentele potrivite. Tatiana și ție îți multumesc pentru toate momentele de bucurie oferite de-a lungul anilor, pentru discuțiile colorate și pentru vacanțele frumoase in Spania! Mult success în anii studenției! Ionuț, I am very happy and proud you finally found your “vocation”! I wish you a lot of fun in the medical university!

In het bijzonder wil ik Alice en Tjeerd Nijhuis bedanken voor hun onvoorwaardelijke steun en liefde, jullie zijn voor mij meer dan alleen mijn schoonouders. Eric, Lydia en Lucas jullie ook bedankt voor de gezelligheid en jullie liefde.

Last but not least, I want to thank Alex, the dearest person in my life. Your love, encouragement, optimism, patience and understanding make me pass easier through the difficult times.

Thank you!  
Cristina

# Curriculum vitae

Cristina Simona Enache was born on 30<sup>th</sup> of October 1978 in Brasov, Romania. She attended primary and secondary school in Romania. From 1993-1997 she followed the high-school education section “Chemistry –Biology” at ‘Grupul Industrial Tractorul’, from Brasov and received her diploma in June 1997. In the same year Cristina was admitted at the University of ‘Transilvania’, Brasov, Romania, Faculty of Science, Department of Physics and Chemistry. In 2001 she was awarded a Erasmus-Socrates scholarship and came to Delft University of Technology in The Netherlands and studied ‘*Spray Pyrolysis Deposition of oxides for Organic Solar Cells*’ under the supervision of dr. C. Huisman, dr. A. Goossens, and, Prof. dr. Joop Schoonman. In February 2002 Cristina graduated in physics and chemistry at “Transilvania” University.

From July 2002 to July 2007 she was a Ph.D. student in the Inorganic Chemistry section, Faculty of Applied Science, Delft University of Technology. In this group Cristina performed research to improve and characterize various semiconductor materials as photo-electrodes for hydrogen production from water and solar energy, under the supervision of dr. Roel van de Krol and Prof. dr. Joop Schoonman. The results of her work are presented in this Ph.D. thesis. Parts of this work were presented at several national and international meetings, among this IPS-15 and IPS-16 held in Paris and respectively in Uppsala-Sweden, and Materials Research Society Fall Meeting held in Boston, Massachusetts.



# List of publications

Gh. Roman, C. Enache, I. Manciulea, and, L. Stezar '*Synthesis and reactivity of Mannich Bases XIII. Mannich reaction of 5,6 Dimetil-benzimidazole with (Hetero) aromatic Amines*', Bulletin of the Transilvania University of Brasov, Series B: Mathematics, Physics, Chemistry, Medicine, Philology (2001), 8 75-78.

Carazeanu, E. Chirila, A. Badanoiu, and, C. Enache '*Hydratation process of  $Ca_{12}Al_{14}O_{33}$  synthesized by unconventionally methods*' Proceedings International Conference of Materials Science and Engineering (Bramat), vol. IV, 2003.

Cristina S. Enache, J. Schoonman, and, R. van de Krol '*The photoresponse of Iron- and Carbon-doped  $TiO_2$  (Anatase) Photoelectrodes*', Journal of Electroceramics 13, 177-182, 2004.

C. S. Enache, J. Schoonman, and, R. van de Krol, '*Addition of Carbon to Anatase  $TiO_2$  by n-Hexane Treatment-Surface or Bulk Doping?*' Proceedings 17<sup>th</sup> Workshop on Quantum Solar Energy Conversion (Quantsol), 2005.

Cristina S. Enache, J. Schoonman, and, R. van de Krol '*Properties of Carbon-doped  $TiO_2$  (Anatase) Photo-Electrodes*' Materials Research Society Symposium Proceedings Vol. 885E, Number 0885-A10-11.1, 2006.

Cristina S. Enache, J. Schoonman, and, R. van de Krol '*Addition of Carbon to Anatase  $TiO_2$  by n-Hexane Treatment-Surface or Bulk Doping?*' Applied Surface Science 252, 6342-6347, 2006.

Alexandru Enesca, Anca Duta, Marius Nanu, Roel van de Krol, Joop Schoonman, Cristina Enache '*Photoelectrode materials of tungsten oxide ( $WO_3$ ) for water splitting*', Proceedings of the International Semiconductor Conference, CAS 2, article nr. 1558782, 293-296, 2005.

Alexandru Enesca, Cristina Enache, Anca Duta, and, Joop. Schoonman ‘*High crystalline tungsten trioxide thin layer obtained by SPD technique*’, Journal of the European Ceramic Society 26, 571-576, 2006.

Yongqi Liang, Cristina S. Enache, and, R. van de Krol ‘*Photoelectrochemical Characterization of Sprayed  $\alpha$ -Fe<sub>2</sub>O<sub>3</sub> Thin Films: Influence of Si Doping and SnO<sub>2</sub> Interfacial Layer*’, International Journal of Photoenergy 739864, 2008.

Cristina S. Enache, David Lloyd, M. R. Damen, J. Schoonman, and, R. van de Krol ‘*Photo-electrochemical Properties of Thin-Film InVO<sub>4</sub> Photoanodes: the Role of Deep Donor States*’, Journal of Physical Chemistry C 113, 19351-19360, 2009.

Roel van de Krol, Julie Ségalini, Cristina S. Enache ‘*Influence of Point Defects on the Performance of InVO<sub>4</sub> Photoanodes*’, Journal of Photonics for Energy 1, 016001, 2011.

Cristina S. Enache, J. Schoonman, and, R. van de Krol ‘*Characterization of structured  $\alpha$ -Fe<sub>2</sub>O<sub>3</sub> Photoanodes via Electrodeposition and thermal oxidation of iron*’, Thin Solid Films 520, 1034-1040, 2011.

#### **Conference presentations (orals):**

Cristina S. Enache, J. Schoonman, and, R. van de Krol ‘*The Photoresponse of Iron- and Carbon- Modified TiO<sub>2</sub> (Anatase) Photoelectrodes*’ Lunteren, CW-dagen, 19-20 January 2004.

Cristina S. Enache, J. Schoonman, and, R. van de Krol ‘*Defect characterization of Carbon-doped Titanium Dioxide thin films made by Spray Pyrolysis*’, Paris, International Conference on Photochemical Conversion and Storage of Solar Energy (IPS-15), 5-9 July 2004.

Cristina S. Enache, J. Schoonman, and, R. van de Krol ‘*Properties of Carbon-doped Anatase TiO<sub>2</sub> Photo-Electrodes*’, Boston MA, USA, Materials Research Society – Fall Meeting (MRS), November 28- December 2, 2005.